



Università  
Ca' Foscari  
Venezia

Corso di Laurea Magistrale in

## **Scienze Chimiche per la Conservazione e il Restauro**

Tesi di Laurea

### **Scanning macro-XRF: Calculation of Sensitivity and Limits of Detection for common pigments in historical paintings and the investigation of Rembrandt's 'Saul and David'”**

**Relatore**

Prof. Carlo Barbante

**Laureanda**

Longhini Elisa

Matricola 816338

**Anno Accademico**

2013 / 2014

Master thesis realized with



**Universiteit Antwerpen**

Faculteit Wetenschappen

Departement Chemie

Antwerp X-Ray Instrumentation and Imaging  
Laboratory

**Promotor:**

Prof. Dr. Koen Janssens

**Master Student:**

Longhini Elisa

**Erasmus Project**

2012/2013



## TABLE OF CONTENTS

<b>ABSTRACT</b> .....	<b>3</b>
<b>CHAPTER 1: INTRODUCTION</b> .....	<b>4</b>
1.1 Purpose of the study and motivation .....	4
1.2 Scanner MACRO-XRF: advantages and disadvantages.....	5
1.3 The beginning of the scanner MACRO-XRF success .....	6
1.3.1 Example of XRF application in art: Vincent van Gogh “ Patch of Grass” .....	6
<b>CHAPTER 2: EXPERIMENTAL PROJECT</b> .....	<b>8</b>
2.1 Preparation of the samples .....	8
2.1.1 Pre-characteristics of the samples .....	10
2.1.2 Pigments .....	11
2.2. X-Ray fluorescence analysis.....	15
2.2.1 X-Ray wavelength and energy scales.....	15
2.2.2 Interaction of X-Rays with matter .....	15
2.2.3 Scattering interactions .....	16
2.2.4 The photo electric effect .....	16
2.2.5 The XRF Spectrometer.....	18
<b>CHAPTER 3: INSTRUMENT AND METHOD: QUALITATIVE ANALYSIS</b> .....	<b>19</b>
3.1 Bruker M6 Jetstream .....	19
3.1.1 Purpose: time per pixel .....	20
3.1.2 Results .....	20
3.1.3 Purpose: step size .....	23
3.1.4 Results .....	24
3.2 AXIL scanner .....	27
3.2.1 Purpose: Geometry.....	28
3.2.2 Results .....	29
3.3. M6 and AXIL scanner .....	34
3.3.1. Purpose: comparing M6 and AXIL scanner.....	34
3.3.2. Results .....	34
Table 3.7 Operating details of the scans. ....	34
3.4 Discussion .....	38
<b>CHAPTER 4: INSTRUMENT AND METHOD: QUANTITATIVE ANALYSIS</b> .....	<b>39</b>
4.1. Purpose: sensitivity and limit of detection.....	39
4.1.1 Sensitivity.....	39

4.1.2. Limit of detection .....	40
4.2 Methodology.....	40
4.2.1 Calculation .....	41
4.2.2 Results .....	44
4.2.3 Discussion.....	86
<b>CHAPTER 5: CONCLUSIONS AND OUTLOOK .....</b>	<b>88</b>
<b>CHAPTER 6: REMBRANDT: “SAUL AND DAVID”, STUDY OF COBALT.....</b>	<b>90</b>
6.1. Technique and pigments used by Rembrandt.....	91
6.2 History of the painting: “Saul and David” .....	94
6.3 Purpose.....	95
6.3.1 Results and discussion .....	97
6.4. Conclusion .....	100
<b>7. BIBLIOGRAPHY .....</b>	<b>101</b>
<b>8. ACKNOWLEDGMENTS.....</b>	<b>104</b>

## ABSTRACT

The aim of this research was to study and compare the potential of two mobile MACRO-XRF scanners, through the analysis of multilayered paint samples. Wood and plexiglass mockups were painted with some of the most common oil colours in art, using a paint film applicator. Only the paint mockup samples on a wood support were analyzed when covered by different thicknesses of lead white, in order to reproduce realistic sequence of paint layers frequently encountered in historical painting.

The two scanners MA-XRF were the M6 Jetstream, that is the first model of the production run by Bruker and AXIL scanner, an in-house built scanner of the University of Antwerp. The potential of these two instruments was observed and studied through the change of some basic operating parameters of the MA-XRF method: step size, dwell time and detector geometry. Qualitative considerations were based on elemental maps obtained by means of the *Datamuncher* package.

Furthermore, for quantitative analysis, the best instrument AXIL scanner set-up was used. In order to calculate meaningful data of sensitivity and limits of detection for specific marker elements, the dwell time was increased up to 2,5 second per pixel.

The second part of this study shows an application of AXIL MA-XRF scanner involving the imaging of Rembrandt's painting "Saul and David"; here the attention was focused on the different use of cobalt containing compounds/materials in the painting: as a pigment (smalt) or as a drier.

Lo scopo di questa tesi di ricerca è di studiare e confrontare le potenzialità di due scanner portatili MACRO-XRF, attraverso l'analisi di campioni pittorici multistrato. Campioni di legno e plexiglass sono stati dipinti con alcuni tra i più comuni colori ad olio utilizzati nel campo dell'arte, la stesura del colore è stata effettuata con un applicatore per film. Solo i campioni di legno sono stati analizzati e ricoperti da diversi spessori di bianco di piombo, in modo da ricreare la sequenza di strati pittorici riscontrabili in un quadro.

I due scanner MA-XRF utilizzati sono: *M6 Jetstream*, primo modello di scanner macro-XRF prodotto dalla Bruker; e *AXIL scanner*, un macro-XRF portatile, progettato e costruito dall'interno dell'Università di Anversa. Le potenzialità di questi due strumenti sono state osservate e studiate cambiando alcuni parametri fondamentali: step size, tempo per pixel e geometria dei detector. Le considerazioni qualitative si sono basate sull'osservazione delle mappe degli elementi ottenute dal pacchetto software *Datamuncher*.

Una volta individuato il migliore set-up per lo scanner AXIL, questo è stato utilizzato per l'analisi quantitativa. Lo strumento è stato utilizzato con un tempo per pixel fino a 2,5 secondi, in modo da ottenere dei dati significativi per il calcolo della sensibilità e del limit of detection per ogni elemento marker individuato nei pigmenti analizzati.

La seconda parte della tesi mostra un'applicazione pratica del macro-XRF. Il quadro di Rembrandt "Saul and David" è stato scannerizzato con AXIL, focalizzando l'attenzione sul diverso utilizzo del cobalto nel quadro: utilizzato come pigmento (smalto) o come essicante.

# CHAPTER 1

## INTRODUCTION

### 1.1 Purpose of the study and motivation

During the last decade, numerous analytical techniques have been successfully applied in the conservation of art, but there still was not method available that allows the acquisition of distribution images of elements present in surface and sub-surface layers of large painted artefacts. In the last years, mobile macro-XRF (MA-XRF) scanners were developed and they filled this gap. This technique uses a focused or collimated X-ray beam of typically a few hundred micrometers diameter to scan the surface of the artefact. The elements in the material emit X-ray fluorescence radiation that is recorded by one or more detectors and that is characteristic for each element.

In this study, two mobile scanning MA-XRF were studied and compared in the field of scientific art studies: the AXIL scanner and the M6 Jetstream. While AXIL scanner is an in-house scanner developed by the AXIL group (Department of Chemistry, University of Antwerp), the M6 instrument is based on the technical knowledge of Bruker Nano GmbH in the design of XRF scanners and the experience obtained with the in-house built scanners of the University of Antwerp (Alfeld, 2013).

In this research, the two instruments were set to scan multilayered wood samples painted by seven common oil pigments and covered by different thicknesses of lead white. Lead white is a common pigment in art and it was used in the ground layer or to cover paint layers. Furthermore lead has a high atomic number and thus can screen and absorb much of the X-ray fluorescence signals coming from pigments of hidden representations. Elemental distribution maps of the samples were carried out with the *Datamuncher* package, setting each pixel to a grey scale value corresponding to the intensity of the recorded fluorescence radiation. Elemental distribution maps of element present in the sub-surface were observed because of the great interest in the study of historical paintings. Hidden paint layers could give more information about artists during the painting's creation, about their '*modus operandi*' and it could be helpful for conservation treatment and authenticity: this is the reason why multilayered samples were prepared. In fact it could be interesting know which pigment can be clearly detected under a certain thickness of covering layer. For this purpose a quantitative analysis shows the trend of sensibility and limit of detection for each marker elements present in the mockups.

Although macro-XRF instrument allows to record such elemental maps of a broad range of elements in a fast, non-destructive and in situ manner, it is still not commonly available (Alfeld, K. Janssens, J. Dik, W. de Nolf, & G. van der Snickt, 2011). The excellent results acquired in the last years by the AXIL group, suggest that this technique is of great interest in painting's conservation and art-historical community for the investigation of large flat objects.

The second part of this research shows a practical application of AXIL MA-XRF scanner on historical painting. Through a case of study, it was possible to illustrate the value of the instrument and the method in art-historical studies. The investigated painting was "*Saul and David*" by Rembrandt. The goal was to continue the project started in 2011 by Alfeld at al. (Noble, Loon, Alfeld, Janssens, & Dik, 2012) by focusing the attention on one element in particular: cobalt. The different use of cobalt as a pigment (smalt) or as a drier (adding Co in some pigments) was highlighted in the painting. The identification was possible with the *Datamuncher* software, which can highlight the different cobalt's percentages in the elemental distribution maps.

## 1.2 Scanner MACRO-XRF: advantages and disadvantages

Based on the interaction of X-Rays with matter and on its easily transportation, mobile scanner macro-XRF found various analytical applications in conservation science. Below, some of the most important advantages of this technique are listed:

- a) It is a non-destructive technique.
- b) The popularity of XRF in art conservation can be explained by the fact that no other analytical technique can identify so many different elements in an efficient and non-destructive way (Snickt, 2012). XRF allows to collect elemental and spatially resolved information on major and minor constituents of a variety of materials (such as pigments, glasses, ceramics, archaeological finds etc...)
- c) Samples or works of art need a minimal preparation for the scanning. For example paintings can be scanned without any preparation, the only important condition is for them to be perpendicular to the X-Ray beam.
- d) Modifications to the painting's original concept during its creation ( *pentimenti* ) can be visualized to gain insights in the artist's *modus operandi* (Botteon, 2011-2012).
- e) Non-original additions to a painting can be identified to allow for a better planning of the conservation treatments.
- f) M6 has an intuitive control software that allow the operation by a person who has been trained, but who is not specialized in XRF analysis and/or imaging (Alfeld, Pedroso, Hommes, & Snickt, 2013).
- g) Furthermore mobile MA-XRF has the important convention to be easily transported by car, built up and disassembled in situ. In order to avoid stress and any form of transportation, opera can stay in museums, deposits or galleries.

It is also important to highlight the disadvantages of mobile scanner MA-XRF, since only a whole knowledge of the scanner can help research to improve the instrument and art conservator to coupled it with other significant analysis:

- a) Non-destructive scanning XRF has a restricted elemental acquisition: it is restricted generally to a subset of mid-Z elements region. Organic pigments only composed by light atoms (C, O, H), such as organic dyes, cannot be detected.
- b) Furthermore, discrimination between different pigments with identical elemental markers is not directly possible.
- c) Due to the reflection geometry the acquired elemental distribution images are dominated by the surface layers and light elements in hidden layers might not be observable. Indeed detecting an hidden painting could be difficult because of the surface layer' thickness and composition, for example if Pb is present in a surface thick layer, it will absorb most of the emitted fluorescence radiation of hidden pigments. For this purpose, the parameters of MA-XRF can be improved to achieve better results. This is the first point, which will be studied in this research.
- d) In conclusion, museums generally require high performance analysis in a short time, but MA-XRF scans need a long time to obtain high quality images on a large object.

## 1.3 The beginning of the scanner MACRO-XRF success

The first descriptions of MA-XRF for the investigation of historical paintings appeared in the early 1990s, but the method did not find a widespread application until Dik et al. employed it to visualize the study of a peasant's head underneath a painting that the famous artist Vincent van Gogh created during his stay in Paris (J. Dik, Snickt, Loeff, Rickers, & Cotte).

This experiment was done at the Deutsches Elektronen Synchrotron (DESY) in Hamburg, Germany. The logistic and financial efforts of bringing a precious painting to a synchrotron radiation source are considerable and limit the number of paintings that can be investigated. In order to broaden the range of paintings that may be investigated, mobile MA-XRF instruments were developed for *in-situ* investigation of paintings. In these instruments, the X-ray tube and detectors are mounted on a motorized stage that



moved them before the surface of a stationary painting during a scan. Only with the development of the in-house built MA-XRF AXIL scanner, routine scans of paintings became practical to carry out. This scanner allowed the acquisition of elemental distribution images of elements present at a concentration level of several mass percent (pigments used for a painting are generally present at a concentration level of several mass percent), with dwell times from less than one second to few seconds per pixel, otherwise the scans durations could take several hours or even days for small investigation area.

### 1.3.1 Example of XRF application in art: Vincent van Gogh "Patch of Grass"

As I have already said, one of the most interesting application of macro-XRF in scientific art environment, is the potential to discover covered paint layers, which can give meaningful information for historical art or conservation treatments.

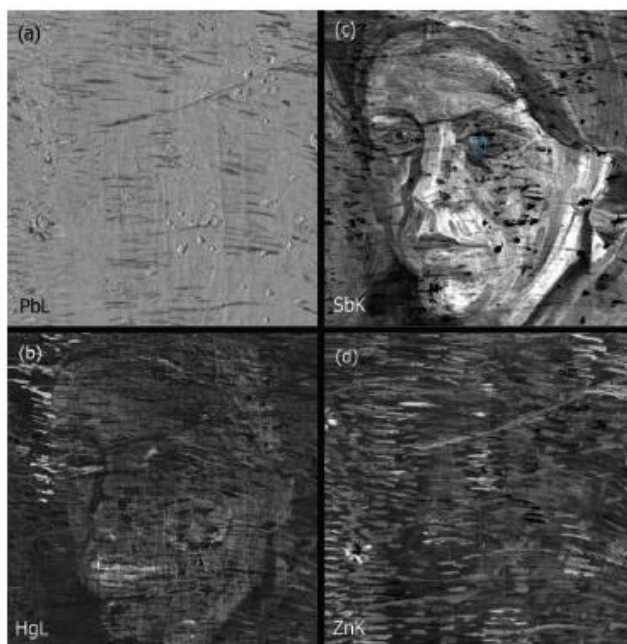
One of the most famous example of an hidden painting is "Patch of Grass" by Vincent van Gogh. This painting was studied by Dik et al. (J. Dik, Snickt, Loeff, Rickers, & Cotte) by means of synchrotron radiation based X-ray fluorescence mapping. They visualized a woman's head under the main painting with unprecedented detail. This approach opened view in the studies of nondestructive paint layers and it has been applying to many old master paintings by Van Gogh (Alfeld, Snickt, Vanmeert, & Janssens, 2013), Rembrandt van Rijn (Alfeld, et al., 2012) and Goya (Bull, Krekeler, Alfeld, Dik, & Janssens, 2011). First of all, the painting was studied with a tube-based X-ray radiation transmission radiography (XRR), focusing the attention on the hidden head. XRR and infrared reflectography (IRR) slightly revealed the hidden head, but, due to the limitations of these two techniques, the images were unsatisfying.



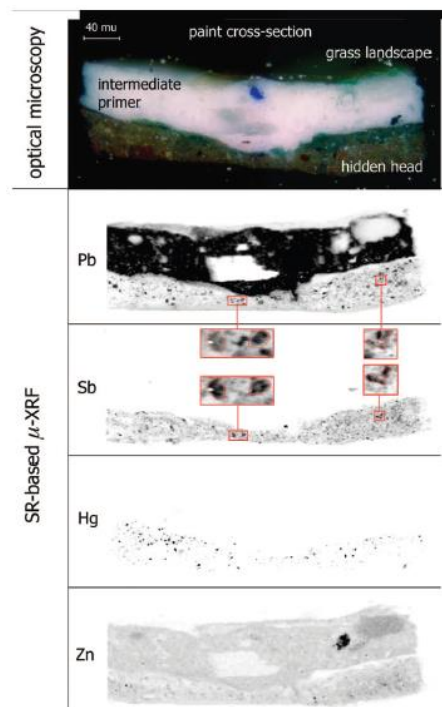
**Figure 1.1** (a) Vincent van Gogh, "Patch of Grass", Paris 1887; (b) XRR scan indicated by the red frame in (a); (c) IRR scan indicated by the red frame in (a) (J. Dik, Snickt, Loeff, Rickers, & Cotte).

Consequently, the painting was transported to undergo microfluorescence beamline L at DORIS-III, a second-generation synchrotron light source at HASYLAB (Hamburger Synchrotronstrahlungslabor at Deutsches Elektronen-Synchrotron DESY, Hamburg, Germany). A pencil beam ( $0,5 \times 0,5 \text{ mm}^2$ ) of quasimonochromatic synchrotron radiation with energy of 38,5 keV was used for primary excitation. They scanned a square of approximately  $17,5 \times 17,5 \text{ cm}^2$ , corresponding to the position of the covered head. The dwell time was 2 second per pixel, so that the total scan time was approximately two days. Fluorescence spectra were also recorded for each pixel with a high resolution energy dispersive Ge-detector.

Thanks to XRF analysis, it was possible to identify the pigments used in the hidden head. Mercury associated with vermilion (HgS) was found in the lips and cheek; zinc associated with zinc white (ZnO), predominantly corresponds to the landscape painting, but also in the light parts of the nose, ear and collar of the head; antimony was at first associated with Naples yellow ( $\text{Pb}_2\text{Sb}_2\text{O}_7$ ), but the distributions for Pb L-shell emission lines and Sb detected by K-shell emission lines did not show any correlation. For this reason a paint sample was taken from a suitable area, near an existing area of paint loss, on the white of the left eye of the hidden face. The cross section revealed the buildup of the paint layers: the surface layer is composed by a greenish glaze; underneath a lead white thick of 50  $\mu\text{m}$  was found and it was served as a secondary priming layer for the landscape painting; underneath there were two dark greenish layers correspond to the hidden head. SEM-EDS and synchrotron-based  $\mu\text{-XRF}$  confirmed the presence of Zn, Sb, Hg and significant amounts of Ca, P, Fe. Moreover, in the two lowest layers, the distribution of Pb and Sb was partially correlated to the level of individual grains. In each Sb-containing grain, Pb was also observed; lead grains were additionally present without Sb, possible as lead white. Besides, this layer is covered by 50  $\mu\text{m}$  of lead white, the secondary priming layer, that hampers any collocation of Pb and Sb.



**Figure 1.2** a) Distribution of Pb L measured with SR-based; b) Hg L-lines map shows the distribution of vermilion (HgS); c) Sb K-lines map shows the distribution of Naples yellow ( $\text{Pb}_2\text{Sb}_2\text{O}_7$ ). The blue frame indicates the paint sample location; d) Zn K-lines map shows the distribution of zinc white (ZnO) (J. Dik, Snickt, Loeff, Rickers, & Cotte).



**Figure 1.3** Cross section of paint sample measured with SR-based  $\mu\text{-XRF}$  shows elemental distributions of Pb, Sb, Hg and Zn. Insets show the correlation of Sb and Pb on the pigment grain level (J. Dik, Snickt, Loeff, Rickers, & Cotte).

For my research I reproduced and investigated a stratigraphic structure, which could be very similar to the layers sequence found in the precious painting *“Patch of Grass”*: pigment layers covered by lead white layers. Moreover I chose some common pigments in historical painting and difficult to detect, like Naples yellow. In the following chapter there is an overview of the samples preparation and pigments used.

## CHAPTER 2

### EXPERIMENTAL PROJECT

In the first part of this chapter, the preparation of the samples and their features will be described focusing on the pigments involved.

In the second part of the chapter, I will explain the history and the characteristics of X-Rays, but before going more deeply in the set-up and use of the instruments involved, I will summarize the principles of X-Ray Fluorescence Spectrometry.

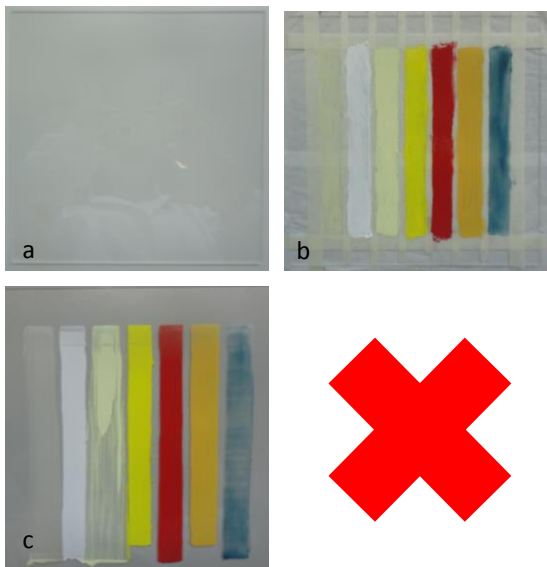
#### 2.1 Preparation of the samples

I chose to use wood and plexiglass material for the samples in order to assess the different matrix effect in X-Ray analysis. Seven common pigments in historical paintings were chosen to be applied in seven strips (1,5 cm X 15 cm) on wood and plexiglass tablets (20 cm X 20 cm): Barium sulfate ( $\text{BaSO}_4$ ), Zinc white ( $\text{ZnO}$ ), Lead tin yellow ( $\text{Pb}_2\text{SnO}_4$ ), Vermilion ( $\text{HgS}$ ), Naples yellow ( $\text{Pb}_2\text{Sb}_2\text{O}_7$ ) and Azurite ( $\text{Cu}_3(\text{CO}_3)_2(\text{OH})_2$ ). Barium sulfate, Lead tin yellow, Vermilion and Azurite were in powder, then they were ground with a glass muller and mixed with drying linseed oil as a binder. The muller was heavy to help grinding of the pigments. It is required lateral movement rather than downward pressure. The time of grinding was different as pigments have different particle size, which is an important factor to taken into account. Larger particle-sized pigments need more time to make a homogeneous agglomerate. The other pigments, Zinc white, Cadmium yellow and Naples yellow, were in tube and so applied with no added oil. For each pigment, there is a specific element (marker) commonly expected to be detected by X-ray fluorescence. A Zehnter ZUA 2000 Universal Applikator was used to level the strips thicknesses. The instrument was set to have 20  $\mu\text{m}$  paint thick, since a normal paint brushstroke measures some tens of micrometers. The instrument has been slid from the top of the sample to the bottom with the same pressure, in order to obtain seven homogeneous strips. Unfortunately, the different texture and grain of the pigment particles did not allow an optimal thickness distribution; furthermore in the plexiglass samples, the strips were completely irregular, probably due to the very smooth and non-absorbent plexiglass surface. For these reasons, only wood samples were used for the research. When the pigments appeared quite dry, they were covered by apply four different thicknesses of lead white in the same manner. The film applicator was set to have 50  $\mu\text{m}$  paint thick for the second level, 100  $\mu\text{m}$  for the third, 150  $\mu\text{m}$  for the fourth and 200  $\mu\text{m}$  for the fifth, while the first level was not covered by lead white.

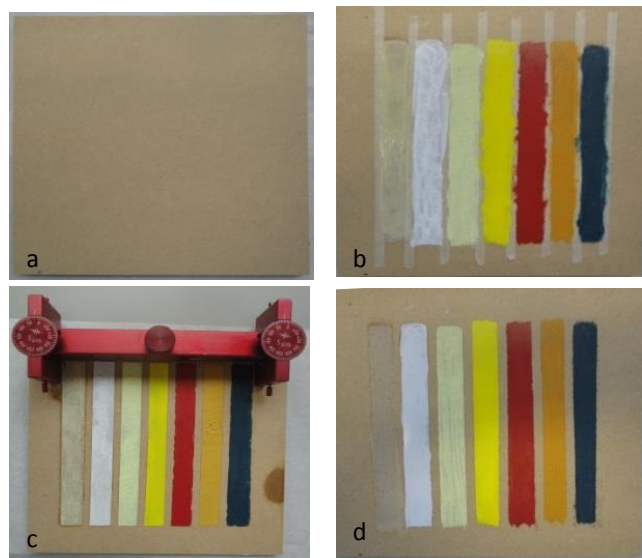
Sequence of sample's preparation:



Figure 2.1 a) preparation of the pigment powder with a pestle; b) palette with the seven pigments prepared; c) film applicator



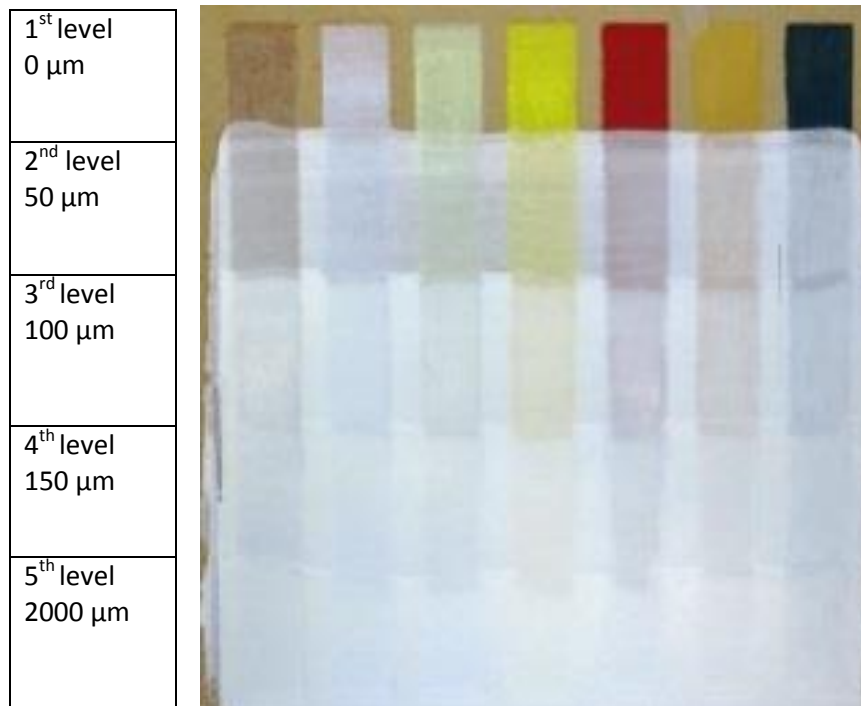
**Figure 2.2** Plexiglass sample preparation: a) plexiglass sample; b) painting pigments; c) sample after using the film applicator.



**Figure 2.3** Wood sample preparation: a) wood sample; b) painting pigments; c) use of the film applicator; d) sample after using the film applicator.

Final sample covered by lead white:






Barium Sulfate	Zinc White	Lead Tin Yellow	Cadmium Yellow	Vermilion	Naples Yellow	Azurite
BaSO <sub>4</sub>	ZnO	Pb <sub>2</sub> SnO <sub>4</sub>	CdS	HgS	Pb <sub>2</sub> Sb <sub>2</sub> O <sub>7</sub>	Cu <sub>3</sub> (CO <sub>3</sub> ) <sub>2</sub> (OH) <sub>2</sub>



**Figure 2.4** First wood sample covered by five different levels of lead white.

### 2.1.1 Pre-characteristics of the samples

I prepared three wooden samples:

	Original sample after using of film applicator	Final sample covered by lead white different layers
<p><b>1<sup>st</sup> sample:</b> The layers of seven pigments seem to be irregular. All the stripes are inhomogeneous, except for cadmium yellow and vermillion. Overall, they show some evident brushstrokes and losses of pigment. Looking at the five layers of lead white, they are inhomogeneous as well, in particular the covering lead white layer on vermillion.</p>		
<p><b>2<sup>nd</sup> sample:</b> The layers of the second sample seem to be better than the first one. Strips are more regular, although some brushstroke are still visible. On the other hand, the first layer of lead white seems to be too transparent, probably it is less than 50 µm thick.</p>		
<p><b>3<sup>rd</sup> sample:</b> The third sample is the most regular in thickness and in homogeneity of colors. Lead white layers are homogeneous too.</p>		

## 2.1.2 Pigments

Analytical chemistry for conservation of works of art had a growing interest in synthetic inorganic pigments, since they are very common in paintings and they proved to be informative during previous scans on important historical paintings. For this reason, in this study, oil paint layers contain inorganic pigments were applied on model samples. Marker elements are expected to be well visualized and in addition we suppose to detect also certain elements that are typically present as contaminants in the surface paint (e.g. Zn in azurite and cadmium yellow, Ni in lead white) or that are more difficult to detect (e.g. Cd, Sb and Sn). The table below lists pigments involved in the study, following by a brief summary of the history and origins of the pigments.

Pigment	Colour	Composition	Time period
Lead white	White	$2\text{PbCO}_3 \cdot \text{Pb}(\text{OH})_2$	15 <sup>th</sup> - 19 <sup>th</sup> century
Barium sulfate	White	$\text{BaSO}_4$	From early 19 <sup>th</sup> century
Zinc white	White	$\text{ZnO}$	From 18 <sup>th</sup> century
Lead tin yellow	Yellow	$\text{Pb}_2\text{SnO}_4$	13 <sup>th</sup> – 18 <sup>th</sup> century
Cadmium yellow	Yellow	$\text{CdS}$	Available from 1840s
Vermilion	Red	$\text{HgS}$	From 21 <sup>st</sup> B.C. century
Naples yellow	Yellow	$\text{Pb}_2\text{Sb}_2\text{O}_7$	From 17 <sup>th</sup> century
Azurite	Blue	$\text{Cu}_3(\text{CO}_3)_2(\text{OH})_2$	Middle ages - 18 <sup>th</sup> century

**Table 2.1** Pigments involved in the research.

### *Barium sulfate, BaSO<sub>4</sub>*

Synthetic barium sulfate,  $\text{BaSO}_4$ , has been used as a white extender pigment since the early nineteenth century and it also used as dye in 'lake' pigment, (Toch, 1925). The naturally mineral analogue is barite, the starting material for synthetic barium sulfate. There are three main production methodologies for barium sulfate: first barite and coal are heated, forming the sulfide and gaseous byproducts (carbon monoxide and sulfur dioxide). After dissolving the resultant barium sulfide in water and filtering it, the sulfate is precipitated by adding sodium sulfate, then it is filtered, washed and dried. A second method is to have barium chloride to react with sulfuric acid in aqueous solution. Thirdly, we can dissolve barium carbonate with hydrochloric acid so that it will react with sulfuric acid to produce the sulfate (Moser, 1973). Barium sulfate is also commonly called blanc fixe: this, term was allegedly used for the first time by Kuhlman, who began producing the pigment around 1830. Other popular early names for Barium sulfate were “*process white*” and “*permanent white*”. By the late nineteenth century “*constant*” and “*permanen*” white were probably based on zinc white (Eastaugh, Walsh, Chaplin, & Siddall, 2004).

The Colour Index for synthetic barium sulfate is CI 77120/PW 21

### *Zinc white, ZnO*

Zinc(II) oxide,  $\text{ZnO}$ , is a white pigment commonly known as zinc white or Chinese white. Zinc oxide occurs naturally as the mineral zincite (F., 1988), although it is usually red due to the presence of manganese. White zinc oxide has been known since ancient times as a by-product of brass production in which copper and zinc carbonate were smelted, but it was used largely as a pigment since the end of the eighteenth century, when it replaced the toxic lead white. Although it was not toxic, its production diminished due to financially inefficient methods of production and its poor hiding power when used in oil. At that time zinc oxide was still not popular in oil as the paints dried poorly and had poor covering power, but it was reevaluated in 1830, using zinc-oxide in watercolor under the name of *Chinese white*. In France in 1835-1844, Leclaire developed a method for the industrial production of zinc oxide: pure oxide is made from the controlled oxidation of zinc vapors derived from heating metallic zinc at 300 °C . During this time, Leclaire improved zinc white for use in oil painting by combining it with a siccative oil that was boiled with pyrolusite. After 1845, there was a rapid and widespread use of zinc oxide as a pigment. Until 1892, in USA, zinc oxide was produced by burning the zinc ores with coal, although this method produces a less pure oxide. Leaded zinc oxides can also be produced from the direct process using zinc and lead ores as starting

materials. The term “*leaded zinc oxide*” is used in Germany to refer to products containing >90 % ZnO and up to 10 % lead oxide, while in the USA, the term refers to products containing up to 70 % lead compounds, often lead sulfates.

Zinc white, along with titanium dioxide white and lead white, were the three main white pigments used commercially in the mid to late twentieth century. In these applications, zinc white was often mixed with titanium dioxide and lead white paints as a minor component because the strong ultraviolet absorbency of zinc protects the lead and the titanium pigments from photochemical changes. However, zinc oxide has been reported to affect the fading behavior of organic pigments (Eastaugh, Walsh, Chaplin, & Siddall, 2004).

The Colour Index for Zinc white is CI 77947/PW4

#### *Lead tin yellow, Pb<sub>2</sub>SnO<sub>4</sub>*

During the years, lead tin yellow was thought to be Naples yellow, lead-antimony oxide (Pb<sub>3</sub>(SbO<sub>4</sub>)<sub>2</sub>) or yellow lead oxide, partly due to the fact that its preparation is hardly mentioned in any written source. Actually, there are two lead tin yellows used as pigments: “*Type I*” Pb<sub>2</sub>SnO<sub>4</sub>, and “*Type II*” contains silicon in the crystal lattice to give a compound of approximate formula Pb(Sn<sub>1-¼</sub>Si<sub>¼</sub>)O<sub>3</sub> (Clark, 1995). European artists used lead tin yellow from the beginning of the 14<sup>th</sup> century until the early years of the 18<sup>th</sup> century, although it had largely disappeared from painting at the end of the 17<sup>th</sup> century when it was replaced by Naples yellow. Richard Jacobi of the Doerner-Institut in Munich rediscovered lead-tin yellow and made it synthetically in 1941. Jacobi focused on the high tin content in yellow paint samples. Lead-tin yellow is made by heating a mixture of lead oxide with tin dioxide at temperature of 650°-800° C (Type I, tetragonal) or, with silica, to 900°-950° C (Type II, cubic pyrochlore). The two types have different crystal structures, which can be distinguished by X-ray diffraction. Both types are lightfast and essentially stable in all paint media, although Type I, particularly, has a strong inclination to interact with oil binding media to form colourless inclusions; this is now known to be composed of lead soaps.

The earliest recipes for a yellow pigment from lead and tin was found in the Bolognese manuscript from the first half of the fifteenth century. The earliest examples of lead tin yellow ( Type II ) in paintings are from Florentine works ascribed to Giotto and the Di Cione workshop (Gordon, Bomford, Plesters, & Roy, 1985) (Bomford, Dunkerton, Gordon, & Roy, 1989). In Italy, it appears that type I replaced type II during the second quarter of the fifteenth century. On the other hand, Type I is widely found in paintings throughout Europe until the first half of the eighteenth century. Lead-tin yellow is not affected by light and is stable under normal atmosphere. On paintings, lead-tin yellow (type I) has been found mixed with lead white, vermilion, yellow lakes, ochres, verdigris, indigo and azurite; it can be found in the bright green underpaints in the foliage and landscapes of Early Netherlandish School paintings. Furthermore, there are few examples of lead-tin yellow found mainly in Florentine, Bohemian and Venetian paintings (Kuhn, 1993).

The terminology of historic names given to yellow lead-tin compounds is really vast: in old Italian manuscripts, a pale yellow pigment is called *giallolino* or *giallorino* while northern manuscripts use the term *massicot* (now designated as yellow lead oxide, PbO) to describe a pigment prepared from lead and tin ([http://www.kremer-pigmente.com/media/files\\_public/10100e.pdf](http://www.kremer-pigmente.com/media/files_public/10100e.pdf)).

The Colour Index for lead tin yellow is CI 77629/PY

#### *Cadmium yellow, CdS*

Synthetic cadmium sulfide was not commercially available until the 1840s, due to the scarcity of the metal required for its manufacture (Eastaugh, Walsh, Chaplin, & Siddall, 2004). Cadmium yellow replaced the toxic chromium yellow, which is based on lead. Cadmium yellow is an inorganic salt, CdS, and it occurs naturally as the mineral greenockite. It is usually mixed with zinc oxide, so that its chemical formula is CdS + ZnO.

Early forms of the pigment darkened on exposure to air and light: exposure to air, moisture and ultra-violet radiation has also been reported to cause bleaching due to the formation of sulfuric acid which would react with the cadmium sulfide to form colourless cadmium sulfate, although the effect may be reduced with a suitable medium. Cadmium sulfide is incompatible with copper and lead based pigments, with discoloration occurring by the formation of copper and lead sulfides (Church, 1901) (Standage, 1883).

According to Fiedler and Bayard (1986), this pigment has been generally known as cadmium yellow, but other names, dating from the nineteenth century, include *Aurora yellow*, *jaune brillian*, *mutrie yellow*, *orient yellow*, *Radiant yellow* (trade name of the British colourmen Reeves, late nineteenth century), *neutral orange* and *daffodil yellow* (Eastaugh, Walsh, Chaplin, & Siddall, 2004) .

The Color Index for cadmium yellow is CI 77199/PY37.

#### *Vermilion, HgS*

Vermilion is a mercury(II) sulfide, with chemical formula HgS. Originally, this red pigment was made of powdered mineral cinnabar and this is why sometimes HgS is called cinnabar. The word "*cinnabar*" comes from the Greek "*kinnabari*", which is itself a Hindu word meaning dragon's blood.

Cinnabar or vermilion was used from Early Chinese bone inscription (2000 B.C.) to Egyptian Fayum painting and Roman wall painting (1-3 century A.D.) to the Italian medieval and renaissance ages. Nowadays vermilion is considered unhealthy, so it is difficult to buy, but before health restrictions, the only obstacle on the purchase of vermilion was financial restrictions; in fact, only very rich people could afford to commission a painting where cinnabar was used. Cinnabar was one of the most expensive pigment with lapis lazuli, thus the presence of cinnabar in a painting can indicate the rank of the artist.

The main problem with cinnabar is that it often blackens. Blackening of cinnabar ( $\alpha$ -HgS, hexagonal structure) can be caused by exposure to sunlight and to open air (light) and it is thought to originate from its transformation into metacinnabar ( $\beta$ -HgS, black with a cubic structure) (Bearat & al.).

One of the medieval recipe of vermilion stated to take sulfur and grind it on a dry stone and add to it half part of mercury. After mixing it carefully, put it in a glass flask and cover it with clay to block the opening so that the gas does not escape, and put it near fire to dry. Then set it on live coals, and the mercury will mix with the hot sulfur. An indication of the mixing could be the noise from the bottle. When the sound stops, the colour is ready (Delamare & Guineau, 2000) .

The Colour Index for Vermilion is CI 12475, 77947, 11780/PR 170, PW 4, PO 36

#### *Naples yellow, Pb<sub>2</sub>Sb<sub>2</sub>O<sub>7</sub>*

Naples yellow is a lead antimony oxide with the chemical formula Pb<sub>2</sub>Sb<sub>2</sub>O<sub>7</sub>, which is produced in colours ranging from lemon yellow, for the very pure pigment, to darker shades. Lead antimonate yellow has been identified in objects from Egyptian, Mesopotamian, Babylonian, Greek, Roman, and Celtic cultures. In western European art, Naples yellow has been used in majolica pottery glazes since the 16<sup>th</sup> century and in paintings dating since about the 17<sup>th</sup> century. It was most frequently used during the period 1750-1850 after which it was gradually replaced by other yellow pigments.

Early theories placed the origin of Naples yellow as a natural product found around the Vesuvius, but this is probably due only the association with the other yellowish minerals that occur on Mount Vesuvius near Naples, this fact might explain the name "Naples Yellow." There is yet no documentary or analytical evidence to support this hypothesis. Watin (1785) for example, stated that Naples yellow "... is naturally formed around the sulphur mines on Mount Vesuvius", however he also added that there is a dissertation by M. Fougereux de Bondaroy in the Mémoires de L'académie 1766, where Naples Yellow was found to be composed of ceruse, alum, salts of ammonia and antimony. This dissertation marked the point at which the composition of Naples yellow was generally accepted to be lead antimonate. In consequence, through the Renaissance and later periods, many examples of yellow lead-based pigments were thought to be lead antimony oxide (Eastaugh, Walsh, Chaplin, & Siddall, 2004) . This situation was only rectified in 1941, when Richard Jacobi rediscovered lead tin yellow using X-ray diffraction analysis. Since that date, researchers recognized three different types of yellow pigments composed of lead compounds: lead antimonate yellow, lead-tin yellow Type I and lead-tin yellow Type II. Genuine Naples yellow continued to be sold during the 20th century, it is lightfast and chemically stable, but may darken with high temperatures, or exposure to iron compounds or sulfur fumes (Boston, 2013) .

The Colour Index for Naples yellow is CI 77891 / 77492/ 21108/ PW 6 / PY42 / PY83 .



*Azurite, Cu<sub>3</sub>(CO<sub>3</sub>)<sub>2</sub>(OH)<sub>2</sub>*

Azurite is a bright blue hydrated copper carbonate mineral, with the chemical formula Cu<sub>3</sub>(CO<sub>3</sub>)<sub>2</sub>(OH)<sub>2</sub>. The name “*azurite*” derived from the Persian word '*lazward*' meaning blue.

Important sources of azurite were in Germany, Hungary, France and later, in the seventeenth century, in Central America. Azurite is always found in association with malachite, cuprite, tenorite, limonite and chrysocolla.

Preparation of the mineral to use it as a pigment, typically involved crushing and washing. Sometimes it was washed with vinegar followed by extensive rinsing in water; traditionally to induce the blue pigment particles and to separate it from the dross, artists added honey, fish glue or gum was to the water (Harley & Rosamund, 1982). Examination of protein-washed azurite showed that the process effectively removed the associated cuprite. Traditionally, artists used azurite in a tempera medium because in oil it darkens and becomes muddy. Many historical names for azurite reflect the possible origin of the mineral or pigment such as *azzurro della magna*, in seventeenth century *lapis Armenius*, *Melochites*, *Spanish bise* and *blue ashes of Seville*, while Merrifield (1849) also lists *German azure*, *Lombardy a.*, *Spanish a.*, *Teutonic a.*, *Hungarian blue*. Harley indicates that the English term '*bice*' was, in the seventeenth century at least, used exclusively in connection with azurite, while in later centuries, “*bice*” was applied to other blue pigments. The synthetic analogue (copper carbonate hydroxide, azurite type,) is generally called *blue verditer* (Eastaugh, Walsh, Chaplin, & Siddall, 2004).

The Colour Index for Azurite is CI 77947 / 74160 / 77492/ PW 4 / PB 15:1 / PBr 7

## 2.2. X-Ray fluorescence analysis

In this study, only *macro-scanning X-Ray Fluorescence* spectrometry (MA-XRF) was employed as a technique. In addition micro samples were taken from each level of the three mockups. The cross sections were analyzed with the Optical Microscope to confirm the thicknesses of the layers. Therefore, a brief summary regarding the phenomenon of X-ray fluorescence could be appropriate to better understand the results in the next chapters.

In the 1895, Röntgen detected electromagnetic radiation in the wavelength of X-rays or Röntgen rays. Röntgen experimented that X-rays could penetrate deeply into materials, apparently without causing damage or changes. Now we know that X-rays are similar to radiation of longer wavelengths and that high radiation can induce discolorations and other damages on biological tissues, but they can be used on inorganic materials without changing. Thus X-rays are used to analyze the composition and the structure of cultural heritage and of many other materials. X-rays can be applied in X-ray fluorescence analysis (XRF), which consists in the ionization of the atoms of the investigated material by an energetic beam of primary X-rays. Indeed the ionized atoms emit fluorescence radiation, which identifies the nature and the concentration of the element in the sample (Janssens, 2013). Thus X-ray fluorescence is a non-destructive analysis of cultural heritage materials; in fact it is often applied to obtain qualitative and semi-quantitative information on materials.

### 2.2.1 X-Ray wavelength and energy scales

When a beam of X-rays is directed onto an object, a number of interactions can take place: transmission, polarization, reflection, refraction, diffraction, pair production, scattering and absorption. The latter, and in particular the photo-electric effect, is the base of XRF analysis (Snickt, 2012) .

The energies of X-ray photons (from 10 nm to shorter wavelengths) are of the same order of magnitude as the binding levels of inner-shell electrons (K, L, M, N, ... levels) and therefore X-rays can be used to excite the atom. This process is called photoelectric absorption. The wavelength  $\lambda$  of an X-ray photon is inversely related to its energy  $E$  according to:

$$\lambda(\text{nm}) = \frac{1.240}{E(\text{keV})} \quad (2.2.1.1)$$

X-ray analysis most commonly employ radiation in the range of 1–50 keV (10–0.2 Å ). For measuring wavelengths in X-ray region, the unit used is Angstrom ( 1Å = 0.1 nm).

### 2.2.2 Interaction of X-Rays with matter (Janssens, 2013)

When X-ray beam interacts with matter, there are three main effects: fluorescence (absorbed photons), Compton scatter and Rayleigh scatter (photons scattered back) Fig. 2.5. So that the intensity  $I_0$  of the X-Ray beam passing through a layer of thickness  $d$  and density  $\rho$  is reduced to an intensity  $I$  according to the law of Lambert–Beer:

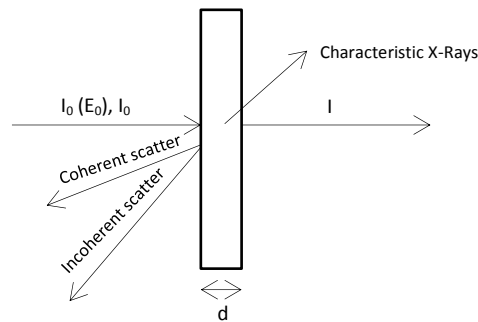


Figure 2.5 X-Ray matter interactions.

$$I = I_0 e^{-\mu \rho d} \quad (2.2.2.1)$$

$I$  = X-Ray photons  
 $I_0$  = transmitted fraction of X-Ray photons  
 $\mu$  = mass attenuation coefficient  
 $\rho$  = density of the sample  
 $d$  = thickness of the sample

While the energy is unchanged, the intensity is reduced. The term  $\mu$  [ $\text{cm}^2/\text{g}$ ] is the mass absorption coefficient and the product  $\mu_L = \mu \cdot \rho$  is the linear absorption coefficient, which is expressed in  $\text{cm}^{-1}$ . More frequently calculating the absorption factor or more in general the sensitivity, the total cross-section for X-ray absorption at energy  $E$  is used ( $\mu(E)$ ). Looking at elements in periodic table, low  $Z$ -elements attenuate or absorb X-Rays less than high  $Z$ -elements. The mass attenuation coefficient of element  $i$  can be written as:

$$\mu_i = \tau_i + \sigma_i \quad (2.2.2.2)$$

$\tau_i$  = cross-section for photo-electric ionization  
 $\sigma_i$  = cross-section for scattering interactions.

### 2.2.3 Scattering interactions

A part of the incoming radiation is reflected by the sample and this effect is called Scattering. Scatter takes place when a photon hits an electron and bounces away. Two scattering phenomena can happen: elastic Rayleigh (elastic scatter) and Compton (incoherent scatter). The first takes place when a photon hits electrons in strong bound, the electrons start oscillating and emit a radiation with the same energy of the incoming radiation. Inelastic or Compton scattering occurs when photons hit bound electrons, while Compton occurs when X-ray photons interact with electrons in the weakly bound.

So that the total cross-section for scattering  $\sigma_i$  can be written as the sum of two components:

$$\sigma_i = \sigma_{R,i} + \sigma_{C,i} \quad (2.2.4.1)$$

## 2.2.4 The photo electric effect

When primary excitation X-ray emitted from a X-ray tube hits the sample, it will be scattered by either X-ray absorbed to an atom or penetrated through the substance. Photoelectric effect refers to a process when X-ray transfers all energy to the deepest part and absorbed by the atom.

In this process, if the primary X-ray has enough energy, an electron will be ejected from the K-shell and the atom becomes ionized. Since the atom always tries to return to the stable state, an electron from the L or M shell filled the electron vacancy created in the K-shell. This transition process is accompanied by the emission of a specific X-Ray line known as  $K\alpha$  line for electron comes from L shell or  $K\beta$  line if the electron comes from the M shell. This process leaves in the L or M shell a vacancy, which can be filled by electrons falling from further orbits, so that L or M-line emission can occur (Gauglitz & Vo-Dinh).

Corresponding to the difference in energy between the atomic shells involved, the characteristic X-rays fluorescence allows the identification of the element, since the energy difference between discrete levels depends only on the atomic number  $Z$ . Thus elemental analysis, such as measurements of wavelength or energy and intensity of the characteristic X-ray photons, can be used to identified elements in the analyte and their mass or concentration. Next to this form of relaxation, Auger Effect can take place. In this case, atom uses the free energy for an auto-ionization and the atom delivers another electron (Auger electron) instead of the photon. The probability of this competitive process is higher for elements with low energetic levels (low  $Z$  elements).

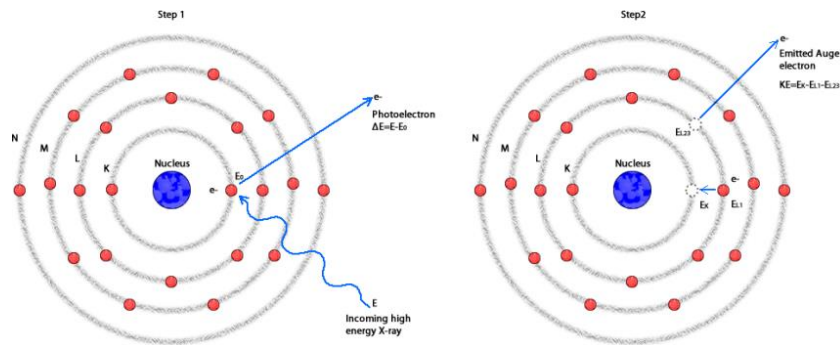


Figure 2.6 Photo electric and Auger Effect

As a consequence, the amount of radiation emitted by a certain level will depend on the efficiency of the two processes of de-excitation and it is usually called fluorescence yield ( $\omega$ ). The fluorescence yield is the ratio of the number of emitted characteristic X-rays to the total number of inner-shell vacancies in a particular atomic shell. As we have already said, for light elements ( $Z < 20$ ), Auger effect is high, so that their  $\omega_K$  is really low, while medium and heavy  $Z$  elements are preferentially relaxing in a radiative manner. This is the reason why X-ray analysis are limited for element with  $Z < 20$ . On the other hand, it is not possible to detect K-line fluoresce for high  $Z$ -element ( $Z > 50-56$ ), because they need really high energy source to be excited.

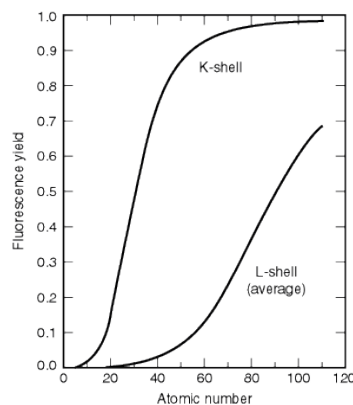
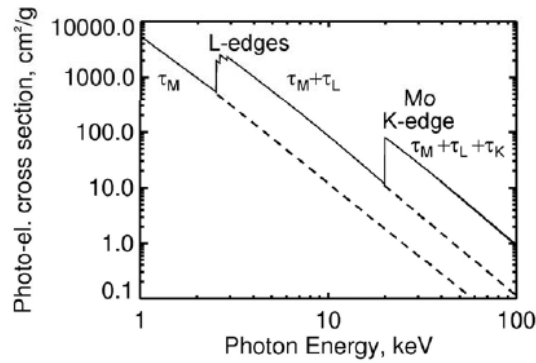


Figure 2.7. Fluorescence yields for K and L shells for  $5 < Z < 110$  (Thompson, Kirz, T.Attwood, Gullikson, Howells, & Kortright., 2009)

Photo-electric absorption happens when the energy  $E$  of the incoming radiation is equal or higher than the binding energy ( $\phi$ ) of the hit electron. Photo-electric absorption can happen in every excitable energy levels of the atom and, as a consequence, the sum of specific shells contributions give the total photo electric cross section  $\tau_i$ :

$$\tau_i = \tau_{i,K} + \tau_{i,L} + \tau_{i,M} + \dots = \tau_{i,K} + (\tau_{i,L1} + \tau_{i,L2} + \tau_{i,L3}) + (\tau_{i,M1} + \dots + \tau_{i,M5}) + \dots \quad (2.2.3.1)$$



**Figure 2.8** Cross section of Mo. Variation of  $\tau_{Mo}$  as a function of X-Ray photon energy. K, L and M edges are clearly visible (Janssens, 2013).

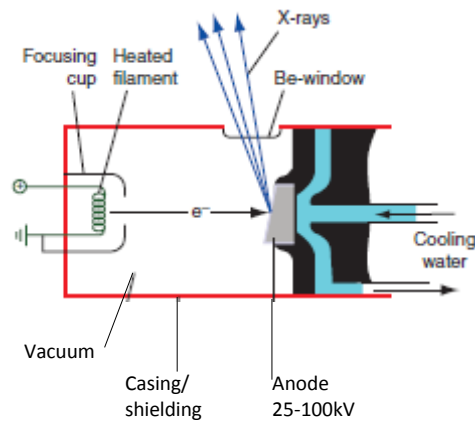
As the energy of the X-ray photon decreases, the cross section increases, i.e. more vacancies are created. The discontinuities in the photoelectric cross-section are called absorption edges (Fig. 2.8). Therefore an element can be determined with high sensitivity when the exciting radiation has its maximum intensity at an energy just above the K-edge of that element, in fact at  $\phi_K = 19,99$  keV ( that is the binding energy), there is an abrupt decrease in cross section (Fig. 2.8) (Janssens & Grieken, 2004) .

## 2.2.5 The XRF Spectrometer

The working principle of XRF analysis is the measurement of the wavelength or energy and intensity of the characteristic photons emitted from the sample when it is irradiated by a primary X-rays beam. All the information are stored in the XRF spectrum in which all characteristic emission lines and the other interaction processes are superimposed to the background.

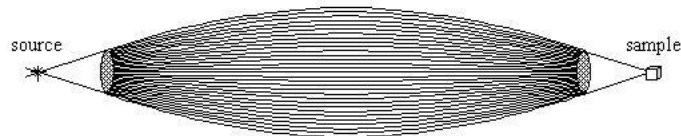
All the spectrometers are composed by a source, which irradiates a sample and a detection system, that measures the radiation emitted by the sample.

Sample can be irradiated by a primary X-rays beam comes from three different X-Ray sources. In our case, MA-XRF has a X-ray tube source, but rotating anode tubes or synchrotron radiation facilities are also employed for analytical purposes. Sealed X-ray tube (Fig. 2.8) typically employs a heated tungsten filament to induce the emission of thermionic electrons in a vacuum chamber. The electrons are accelerated through a high voltage and directed to the anode, which is composed by a high purity metal (e.g. Rh, W, Mo, Pd, . . .). The metal of the anode produces a bremsstrahlung continuum, onto which the characteristic lines of the element of the anode are superimposed ( "Brems" is German for decelerate and "strahlung" for radiation (Brouwer, 2010) ). The radiation from these high purity metals is suited for the excitation of the characteristic lines of a wide range of elements. To increase the intensity of the primary beam, high atomic number of the anode material is required (Janssens, 2013) .In our case M6 is equipped by an Rh-Anode, while the source of AXIL can be changed, I will examine both the Mo-anode and Rh-anode sources for AXIL scanner



**Figure 2.9** Cross section of a sealed X-ray tube

Both M6 and AXIL scanner are equipped by a polycapillary X-Ray optic, which consists of an assembly of monocapillaries. Monocapillary consists of a small hollow glass tube and a large amount of curved tubes form a spindle-shaped. The particular application and the energy range of the optic will be used in determine the optimal curvature and channel size. The optic collects the emerging X-Rays from the X-Ray source within a large solid angle and redirects them, by multiple external total reflections, to a focused or parallel beam. The rapid development of polycapillary optics in commercial instruments enhanced their performance and triggered the development of compact X-ray spectrometers (Tsuji, Injuk, & Grieken, 2004).



**Figure 2.10** Sketch of a focused monolithic polycapillary optic.

While the sources are generally of three type, the detection systems are divided in two main group: energy dispersive system (EDXRF) and wavelength dispersive system (WDXRF). Detector in EDXRF spectrometer measures and separates the radiation coming directly from the sample into the radiation from the elements in the sample. This process of separation is called dispersion. In the WDXRF spectrometers, the dispersion is made by a crystal, which diffracts the incoming energies in different directions. Furthermore EDXRF usually is equipped by a solid-state detectors, while WDXRF has gas-filled detectors and scintillation detectors. All these detector produce electrical pulses, which are proportional to the energy of the incoming photons. The pulse are amplified and stored in a multichannel memory. The result is a spectrum with X-ray energy versus intensity (cps) (Brouwer, 2010) . M6 and AXIL scanner are equipped by silicon-drift detector (SDD).

## CHAPTER 3

### INSTRUMENT AND METHOD: QUALITATIVE ANALYSIS

The aim of this chapter is to improve the analytical performance working on measurement conditions. The spatial resolution of a measurement by MA-XRF is influenced by different factors such as the step size, the time per pixel and the geometry of detectors and source. The influence of these factors on the spatial resolution will be examined in this chapter.

Least squares fitting of individual XRF spectra conventionally carried out the evaluation of XRF spectra but this approach became impractical as the pace at which data could be acquired became faster than that which data could be processed. To accelerate the data processing, Matthias Alfeld, member of the research group of Koen Janssens, University of Antwerp, wrote a software package, called *Datamuncher*, that allows the processing of several thousand spectra per second based on Dynamic Analysis. The files sum spectra obtained were then fitted with PyMca, a freely available software package developed at the European Synchrotron Radiation Facility (ESRF, Grenoble, France) [<http://pymca.sourceforge.net/>]. In this study, I carried out the reported elemental distribution maps with *Datamuncher*, since this has been created to obtain sharper images than those achieved by PyMCA. Each image (or map) shows how a specific element is distributed over the surface of the painting, therefore the grey-scale of the images is indicative for the local mass per unit area of the element. I will show only the K-lines elemental maps because they are more energetic than L-lines, which are easily absorbed by covering lead white layers. In particular the  $K\alpha$ -lines radiations are easier to be detected in the hidden painting than  $K\beta$ -lines, because their higher chances to occur.

#### 3.1 Bruker M6 Jetstream (Alfeld, 2013)

The Bruker M6 Jetstream was developed by Bruker Nano GmbH (Berlin, Germany) in close contact with the Universities of Antwerp and Delft. It is based on the technique of the Bruker M4 Tornado micro-XRF scanner and the experience gained with the previous in-house built instrument of the University of Antwerp. It is the first commercially available XRF scanner for large objects.



**Figure 3.1** M6 Jetstream, the Bruker first model of the production run (Alfeld, Pedroso, Hommes, & Snickt, 2013).

The M6 Jetstream consists of a measuring head that is moved over the painting's surface through a X-Y motorized stage with a Silicon-Drift detector. The motorized stage features a minimum step size of  $10\ \mu\text{m}$  and a maximum travel range of  $80\ \text{cm} \times 60\ \text{cm}$  (h x v). The distance between the measuring head and the painting is adjusted by a motorized stage of  $7\ \text{cm}$  travel range oriented along the Z axis.  $1 - 1,5\ \text{cm}$  is the right distance to be observed between the painting and the measuring head. The measurement head travels within a metal frame that can be tilted in order to adjust it to the surface of a painting and to allow the analysis of horizontally positioned samples. The frame holding the motorized stage is mounted on a box containing the detector electronics, the motor control electronics and the high voltage generator of the X-Ray tube. The measuring head consists of a  $50\ \text{W}$  Rh-target micro-focus X-Ray tube with a maximum voltage of  $50\ \text{keV}$  and a maximum current of  $0.6\ \text{mA}$ . The beam is defined through a polycapillary optic, allowing a variable beam size (with ca.  $40\ \mu\text{m}$  as the smallest beam size) as a function of the distance between the painting and the measuring head. Two

optical cameras with magnifying optics, focused on the surface of the painting are mounted on the measuring head. The focal plane of the stronger magnifying camera can be manually adjusted in five steps and is used to control the distance from the measuring head to the painting and thus the beam size. The other camera can be used to automatically acquire “mosaic images” of the whole surface of the painting that allow direct comparison of these images with the elemental distribution images. This is a very helpful feature for the operator because the “mosaic images” are used for defining the scanned area. This important feature is not present in the software of AXIL scanner. For geometrical reasons the cameras observe the surface of the painting with a slight offset from the spot excited by the X-Ray beam. This offset is automatically corrected by the control software during measurement.

### 3.1.1 Purpose: time per pixel

The purpose of these scans was to operate with the same step size, but increasing the time per pixel, in order to observe and compare the different resolutions images and the changing in operating time. The scanner operated at 50 keV voltage, 600  $\mu$ A current beam and 520  $\mu$ m beam size. The sample n. 1 was scanned first with 500  $\mu$ m step size and a dwell time of 10 ms for pixel, for a total operating time of about 20 minutes. The second scan parameters were 500  $\mu$ m step size and a dwell time of 50 ms for pixel, for a total operating time of about 2 hours and 35 minutes. The third scan parameters were 500  $\mu$ m step size and a dwell time of 500 ms for pixel, for a total operating time of about 25 hours.

### 3.1.2 Results

Original sample, sample number 1:

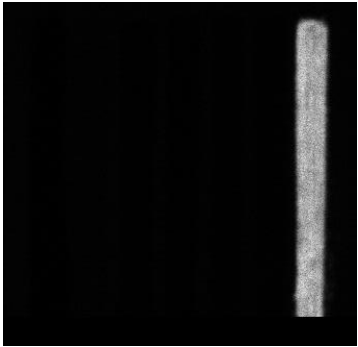
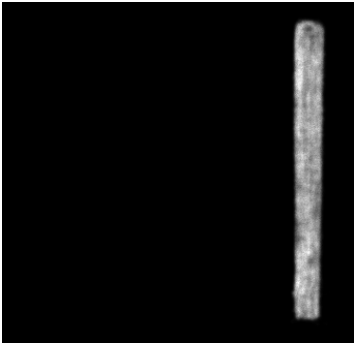
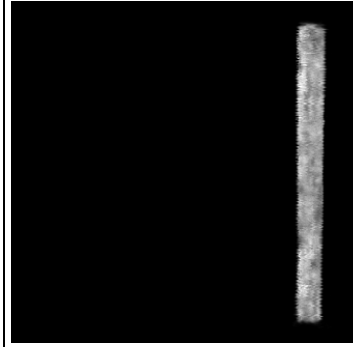
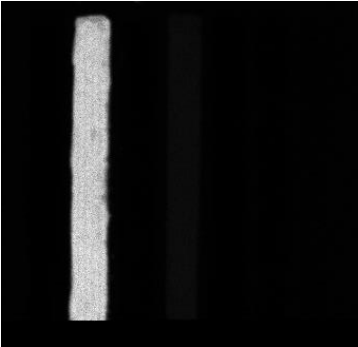
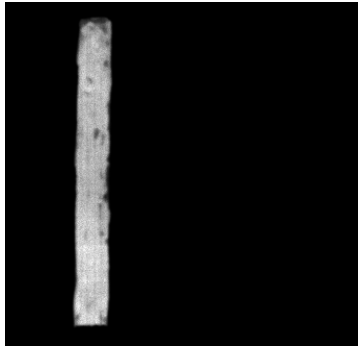
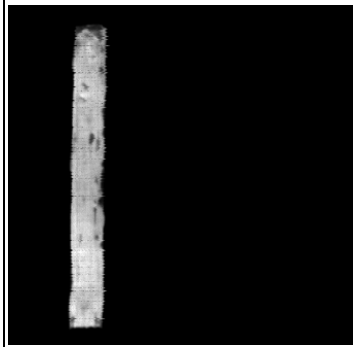
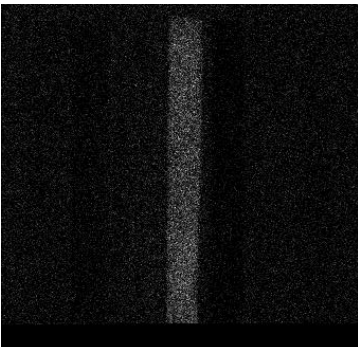
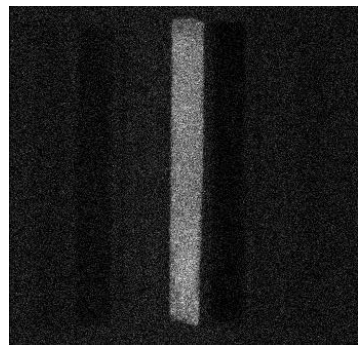
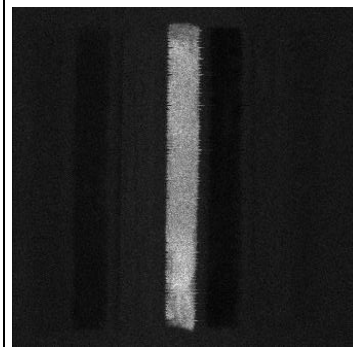


Figure 3.2 Sample number 1

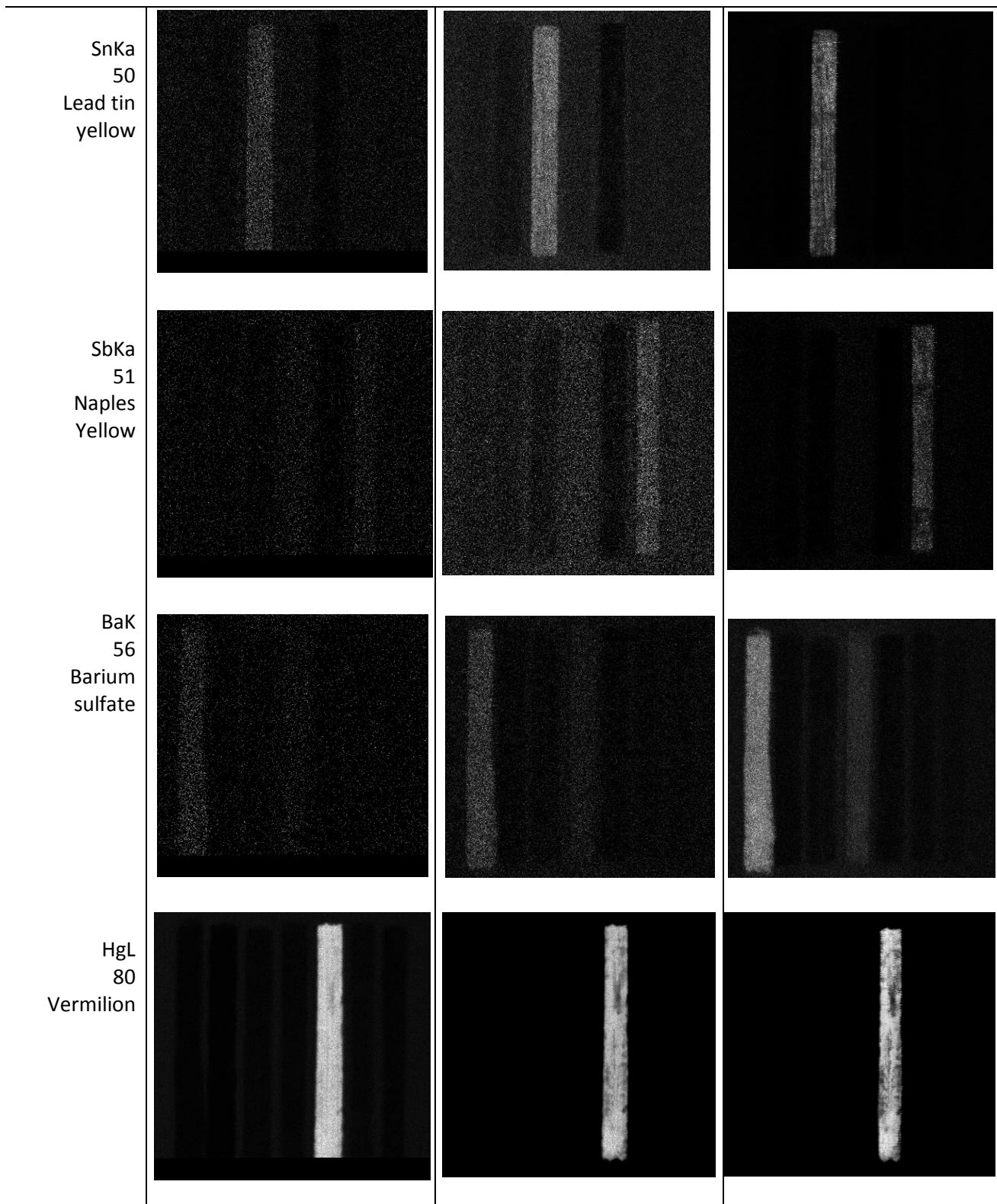
The strips in this sample are not homogeneous. In particular barium sulfate, lead tin yellow and azurite have some evident brush marks. Marks are probably visible in these pigments because they were in powder. It is difficult to obtain pigments with a homogeneous and buttery texture. Artists used to grind the powder for hours in order to obtain the correct consistency. Cadmium yellow and vermilion seem to be homogenous. Cadmium yellow was in tube and vermilion in powder. Vermilion has a very fine grain and it was easily mixable with Drying Linseed Oil to obtain the buttery texture. Although zinc white was in tube, there are some evident gaps in color.

**Table 3.1** Operating details of the scans.

Sample n. 1	Area of scan	Step size (µm)	Time per pixel (ms)	Total time (h)
1 <sup>st</sup> (Rh-anode)	21cm x 22cm	500	10	20 minutes
2 <sup>nd</sup> (Rh-anode)	21cm x 22cm	500	50	2 hours and 35minutes
3 <sup>rd</sup> (Rh-anode)	21cm x 22cm	500	500	25 hours

Element, atomic number, pigment	Instrument: M6 Step size (µm): 500 Time per pixel (ms): 10 Source: Rh	Instrument: M6 Step size (µm): 500 Time per pixel (ms): 50 Source: Rh	Instrument: M6 Step size (µm): 500 Time per pixel (ms): 500 Source: Rh
CuKa 29 Azurite			
ZnKa 30 Zinc white			
CdKa 48 Cadmium yellow			





Looking at the maps of the elements, it is obvious that the image resolution increases with the increasing of the time per pixel, but the operating time increases dramatically: 20 minutes for 10 ms time per pixel and 25 hours for 500 ms for pixel. The problem could be that museums or galleries do not always have time and money available for such long analysis. Trying to focus the attention on the grain of the pictures, a marked improvement in the resolution of the image of the second scan could be observed. Indeed the images of the second and third scans are more spotless and pixels are brighter due to the higher time per pixels.

In particular Cu, Zn and Hg are quite well detected in all scans, but in the second and third scans the resolution of the images are higher, pigments gaps and brush marks are visible. Brush marks are also visible in cadmium yellow and lead tin yellow in the third scan, moreover their element maps do not present the background noise. Background noise makes the reading of Sb and Ba maps difficult in first and second scans, while in the third elements are really well detected, without background noise. Ba and Zn are also visible on cadmium yellow, they are probably present in form of extenders: zinc oxide (ZnO) and barium sulfate (BaSO<sub>4</sub>).

In conclusion if the surface layer of a framework needs to be analyzed, M6 scanner should be set with a time per pixel between 50 ms and 500 ms with a step size of 500  $\mu\text{m}$ , otherwise the elements with high atomic weight (in particular Sb and Ba) cannot be detected by their K-lines fluorescence.

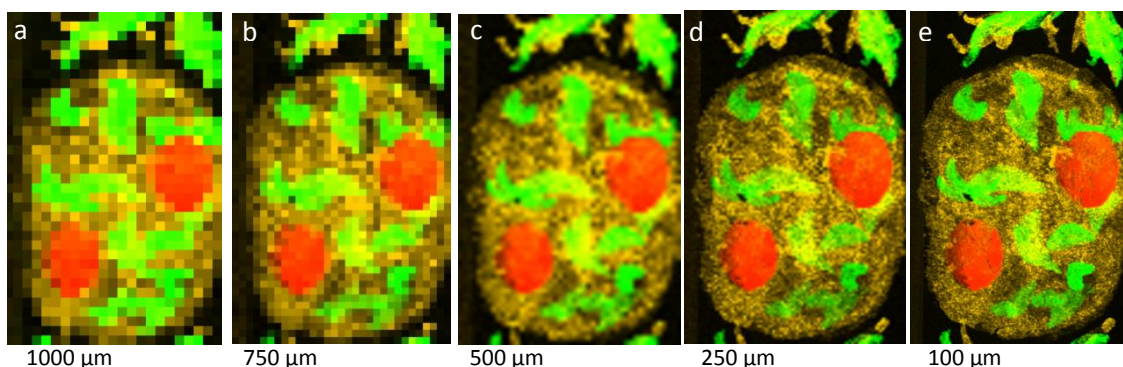
### 3.1.3 Purpose: step size

The following two scans with different step size were done in order to observe and compare the different resolutions images and the changing in the total operating time. Pixel size influences the spatial resolution of elemental distribution images, but for a good contrast between neighbouring pixels, a good contrast is required by varying the acquisition time per pixel, as we have already seen in the paragraph before.

The scanner operated at 50 keV voltage, 600  $\mu\text{A}$  current beam and 520  $\mu\text{m}$  beam size. The sample was scanned first with 1000  $\mu\text{m}$  step size and a dwell time of 17 ms for pixel, for a total operating time of about 15 minutes. The second scan parameters were 350  $\mu\text{m}$  step size and a dwell time of 200 ms for pixel, for a total operating time of about 22 hours and 20 minutes.

### 3.1.4 Results

In the following scans, lateral resolutions below 100  $\mu\text{m}$  can be achieved, but it is not recommended to use for a large area, due to the nature of MA-XRF as a scanning technique with two lateral dimensions. It is necessary six days to scan an area of 50cm x 50cm with a lateral resolution of 100  $\mu\text{m}$  and a dwell time of 20 ms per pixel. However, the same instrument and with a lateral resolution of 500  $\mu\text{m}$  can investigate the same area in just more than 5 hours (Alfeld, 2013).



**Figure 3.3** Map images of a decorated piece of paper with different step size and same time per pixel. Scans were made by G. Van der Snickt.

It is clear that with a low step size (250  $\mu\text{m}$  and 100  $\mu\text{m}$ ), we have an high resolution image. We can see define edges and all details of the drawing. On the other hand, the total operating time may become too long. Looking at the Fig. 3.3a and 3.3b, it is hard to see the scanned pictures, which appear as color spots. The drawing is not clear and the big pixels interfere with the reading of the subject.

In conclusion, It seems that the better operating parameter should be between 500  $\mu\text{m}$  and 250  $\mu\text{m}$  of step size. The same idea has been applied to the mockup n. 1.





Sample covered by lead white, sample number 1:


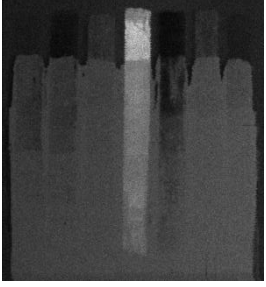
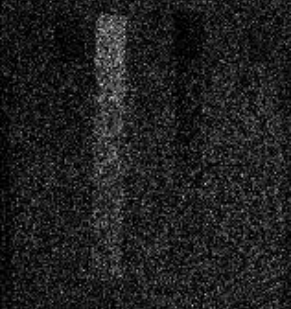
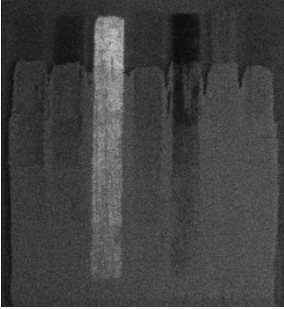
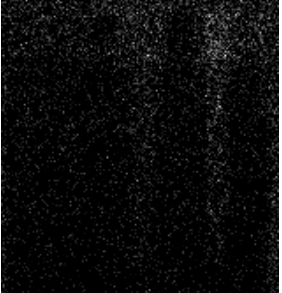
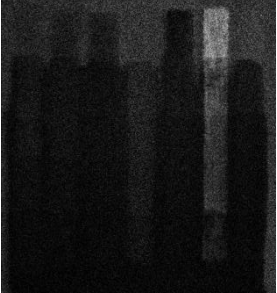
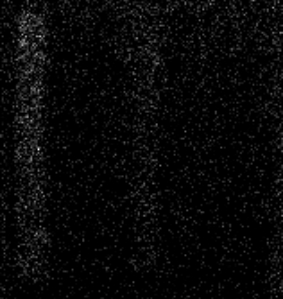
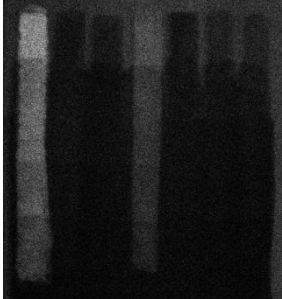




Figure 3.4 Sample number 1

Table 3.2 Operating details of the scans

Sample n. 1	Area of scan	Step size (μm)	Time per pixel (ms)	Total time (h)
1 <sup>st</sup> (Rh-anode)	21cm x 22cm	1000	17	15 minutes
2 <sup>nd</sup> (Rh-anode)	21cm x 22cm	350	200	20 hours and 30 minutes

Element, atomic number, pigment	Instrument: M6 Step size (μm): 1000 Time per pixel (ms): 17 Source: Rh	Instrument: M6 Step size (μm): 350 Time per pixel (ms): 200 Source: Rh
CuKa 29 Azurite		
ZnKa 30 Zinc white		

<p>CdKa 48 Cadmium yellow</p>		
<p>SnKa 50 Lead tin yellow</p>		
<p>SbKa 51 Naples Yellow</p>		
<p>BaK 56 Barium sulfate</p>		
<p>HgL 80 Vermilion</p>		

Focusing the attention on the grain of the pictures, a marked improvement is notable in the resolution of images of the second scan.

In the first scan azurite covered by lead white is not visible, while in the second scan it is still visible under 50  $\mu\text{m}$  of lead white. Zinc white is still visible under 50  $\mu\text{m}$  and 100  $\mu\text{m}$  in both scans. Zn seems to be also in cadmium yellow, probably as a zinc oxide. Cd and Sn are better detected in the second scan, but they can be visible in both scans up to 200  $\mu\text{m}$  of lead white, because their enough high energies (Cd-K $\alpha$ : 23,2 keV ; Sn-K $\alpha$ : 25,3 keV ). Although Cd seems to be well detected, the pile-up artefacts could improve its detection. Pile-up peaks are the effect of two photons hitting the detector in the same time, so that both photons are detected as a sum of the two energies. Pile-up peaks can interfere and lead to wrong conclusions about elements in analysis (Brouwer, 2010). In our case the cascade of photons come from Pb (Pb $_{\alpha 1}$ : 10,55 KeV ; Pb $_{\beta 1}$ = 12,61 KeV ) result as a sum peak at the energy of Cd ( Cd-K $\alpha$  : 23,17 KeV ; Cd-K $\beta$  : 26,10 KeV ).

Sb and Ba are not visible in the first scan, because they are difficult to be detected with a very low time per pixel (17 ms). In the second scan, Ba and Sb are quite well detected up to a covering of 200  $\mu\text{m}$  of lead white. Ba seems to be also in cadmium yellow, probably as an extender. Hg is well detected in both scans up to a covering of 150  $\mu\text{m}$  and 200  $\mu\text{m}$  of lead white.

In conclusion, the images of the second scan are more spotless and pixels are brighter due to the higher time per pixels. A set-up with step size between 500  $\mu\text{m}$  and 350  $\mu\text{m}$  is convenient to get more information and more homogeneous elemental maps.

**Table 3.3** Results

First scan 17ms ; 1000 $\mu\text{m}$	Cu	Zn	Cd	Sn	Sb	Ba	Hg	Second scan 200ms ; 350 $\mu\text{m}$	Cu	Zn	Cd	Sn	Sb	Ba	Hg
0 $\mu\text{m}$	xxx*	xxx	x	x	/	/	xxx	0 $\mu\text{m}$	xxx	xxx	xx	x	x	x	xxx
50 $\mu\text{m}$		x	x	x		/	xx	50 $\mu\text{m}$	xx	x	x	x	x	x	xx
100 $\mu\text{m}$		x	x	x			x	100 $\mu\text{m}$		x	x	x	x	x	x
150 $\mu\text{m}$			/	/			x	150 $\mu\text{m}$			x	x	x	x	x
200 $\mu\text{m}$			/	/			x	200 $\mu\text{m}$			x	x	x	x	x

\*( XXX = really well detected ; / = barely detected )

The parameters of the first scan are good enough to detect some low Z-elements present in the surface layer and middle high-Z elements covered by lead white (present in the hidden painting ). Therefore the parameter of the 1<sup>st</sup> scan should be used for a prescan' painting. Then, observing the obtained image from prescan, it could be possible to perform an additional scanning to obtain a better image in the small area of interest.

### 3.2 AXIL scanner

The instrument described below is AXIL instrument C while in the next paragraph I will show results obtained with instruments C and D. The latter differs from the first ( C ) in the 50 W Rh-anode X-ray tube and in a different detectors geometry. These instruments are an improved version of the "instrument B" described in: "Optimization of mobile scanning macro-XRF systems for the in situ investigation of historical paintings" (Alfeld M. K., 2011).

Matthias Alfeld et al. (AXIL group, Department of Chemistry, University of Antwerp) developed AXIL from 2008 onwards, starting from a conventional laboratory  $\mu$ -XRF setup. The instrument is equipped with four silicon drift detectors (SDDs) and 10 W Mo-anode (or 50 W Rh-anode) X-Ray tube, equipped with a polycapillary X-Ray lens and a beam size of minimum 50  $\mu\text{m}$ . AXIL scanner can reach a scanning area of maximum 60 cm x 60 cm using a voltage of 45 keV and a current of 200  $\mu\text{A}$ . According to the studies carried out by the AXIL group (University of Antwerp), high sensitivity is achieved by positioning the measuring head approximately 1 cm away from the painting in order to avoid the absorption of low energetic fluorescence lines in the air and to enlarge the solid angle from which the fluorescence radiation is recorded, as it depends on the inverse squared distance from the surface .

### 3.2.1 Purpose: Geometry

One of the merits of AXIL scanner is the easy removal and interchangeability of moving parts: interchangeable source, detectors and sample position. The geometry of detectors and source will be now explained further.

The angle of the incident primary radiation  $\alpha$  and the taken-off angle of the emitted radiation  $\beta$  are very important in order to have a better resolution image and sensitivity for covered layers as well. The parameter of geometry is than an important figure of merit for scanning painting through MA-XRF. In our case the absorption in a homogeneous pigment layer covered by a lead white layer between the spectrometer and the sample can be described as:

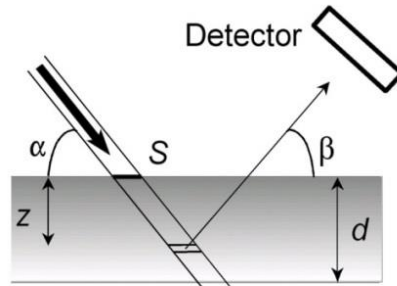


Figure 3.5 Geometry of primary incident X-Ray and taken-off X-Ray fluorescence.

$$A_{tot} = \frac{1 - e^{-X_2(E_0, E_i)\rho_2 d_2}}{X_2(E_0, E_i)\rho_2 d_2} + e^{-X_1(E_0, E_i)\rho_1 d_1} \quad (3.2.1.1)$$

With:  $X(E_0, E_i) = \mu(E_0)\csc\alpha + \mu(E_i)\csc\beta$

- $A_{tot}$  = total absorption factors
- $E_0 = E_0$  = X-Ray excitation energy of element i
- $E_i = E_i$  = X-Ray excitation energy of element i
- $\mu$  = mass attenuation coefficient
- $d$  = thickness ( $d_2$  = pigment thick ;  $d_1$  = lead white thick)
- $\rho$  = density ( $\rho_1$  = pigment density ;  $\rho_2$  = lead white density)

Observing the formula above, it is easy to understand that  $\alpha$  and  $\beta$  should be about 90 degrees to get a low absorption (a small  $A_{tot}$ ). For geometrical reasons, this is difficult to achieve, so researchers chose, for the first set-up, to make  $\alpha$  at 80 degrees and the four  $\beta$  angles at 25 degrees, 36 degrees , 45 degrees and 39 degrees and, for the second set up,  $\alpha$  at 90 degrees and  $\beta$  at 45 and 47 degrees.

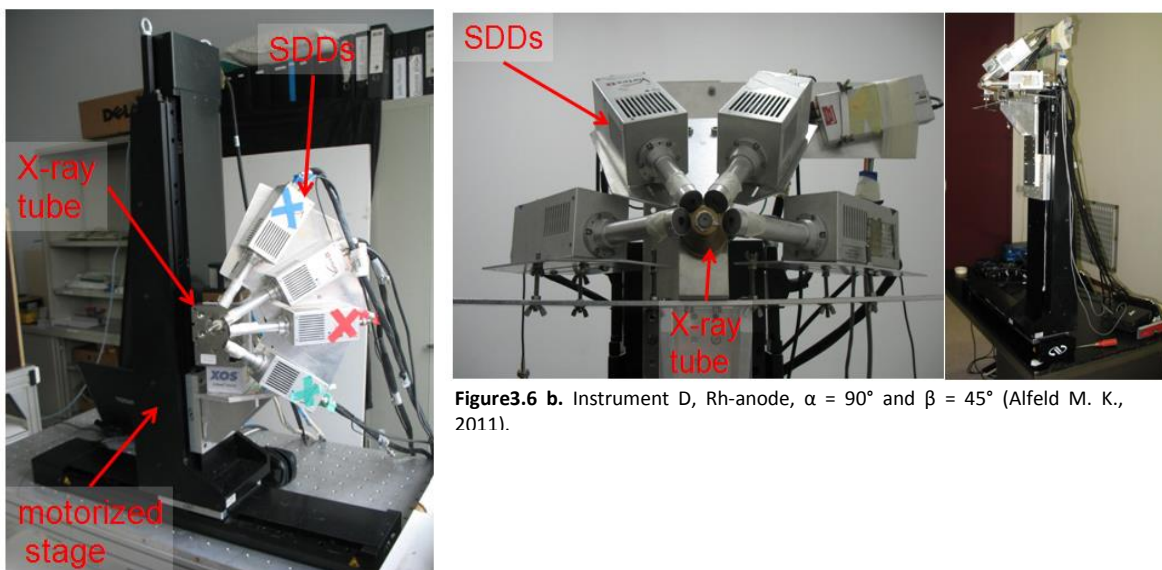


Figure 3.6 a. Instrument C, Mo-anode,  $\alpha = 80^\circ$  and  $\beta = 25^\circ; 36^\circ; 45^\circ$  and  $39^\circ$  (Alfeld M. K., 2011).

Figure 3.6 b. Instrument D, Rh-anode,  $\alpha = 90^\circ$  and  $\beta = 45^\circ$  (Alfeld M. K., 2011).

### 3.2.2 Results

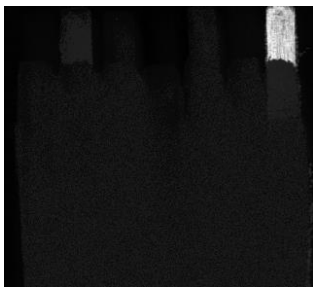
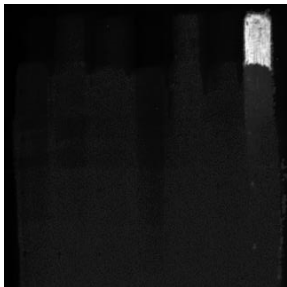
Sample covered by lead white, sample number 1:



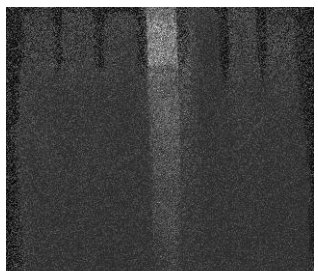
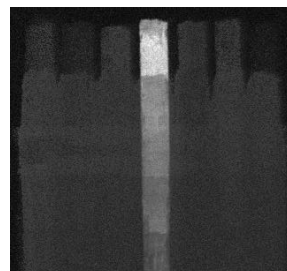
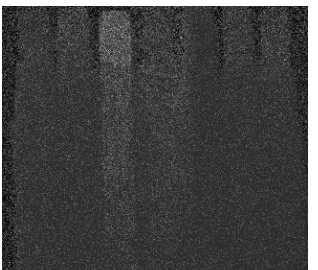
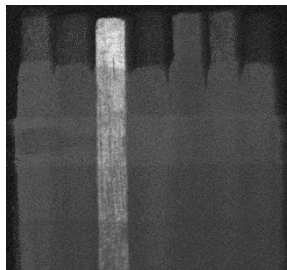
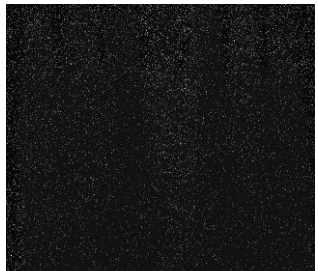
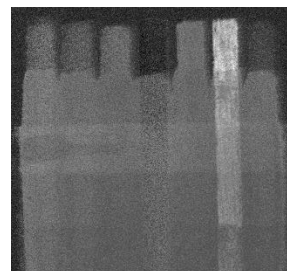
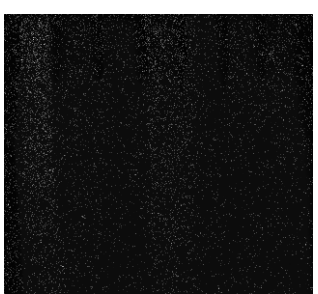
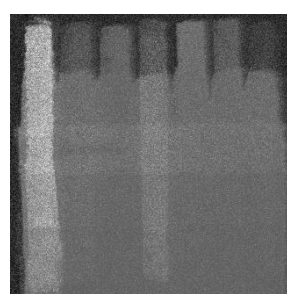


Figure 3.7 Sample number 1

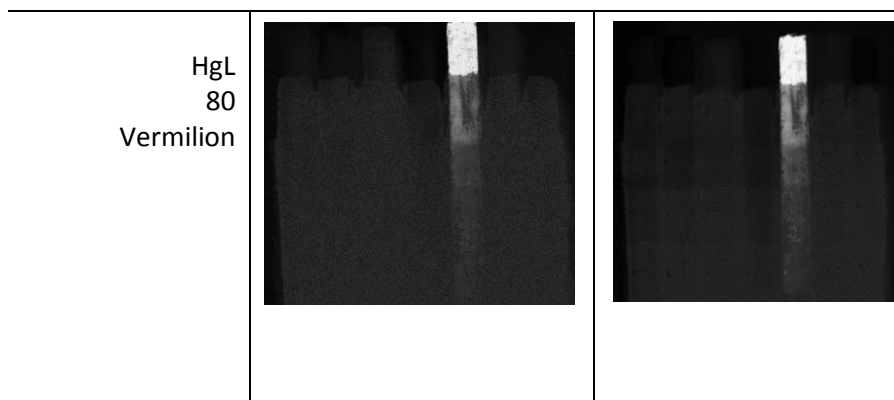
Table 3.4 Operating details of the scans.

Sample n. 1	Area of scan	Step size (μm)	Time per pixel (ms)	Total time (h)	Geometry
1 <sup>st</sup> (Mo-anode)	16,5cm x 17cm	500	850	26 hours and 30 minutes	α angle = 80° β angle = 25°; 36°; 45°; 39° detector are on the left of the source
2 <sup>nd</sup> (Rh-anode)	15,4cm x 16cm	500	850	23 hours and 16 minutes	α angle = 90° β angle = 45° and 47° detectors are closer and around the source

Element, atomic number, pigment	Instrument: AXIL C Geometry: α angle = 80° β angle = 25°; 36°; 45°; 39° Source: Mo	Instrument: AXIL D Geometry: α angle = 90° β angle = 45° and 47° Source: Rh
CuK 29 Azurite		

<p>ZnK 30 Zinc white</p>		
<p>CdK 48 Cadmium yellow</p>		
<p>SnK 50 Lead tin yellow</p>		
<p>SbK 51 Naples Yellow</p>		
<p>BaK 56 Barium sulphate</p>		





Azurite and zinc white are similarly detected in both scans. Azurite is partly visible under 50  $\mu\text{m}$  of lead white, while Zinc is visible up to 100  $\mu\text{m}$  of lead white. Cd and Sn are better detected in the second scan, but Cd can be visible also in the first scans under 50  $\mu\text{m}$ , 100  $\mu\text{m}$ , 150  $\mu\text{m}$  and 200  $\mu\text{m}$  due to their high energy (Cd-Ka: 23,2 keV). Sn is just discernible in the first scan. Sb and Ba are not visible in the first scan, they are not able to be detected with the geometry of the first scan (C geometry), where detector are too far from the sample. Furthermore the particularity of the brushstroke in the original sample of Sn and Sb is clearly visible in the elemental maps of the second scan. Ba and Sb are quite well detected only in the second scan up to a covering of 200  $\mu\text{m}$  of lead white. Hg is quite well detected in both scans up to a covering of 150  $\mu\text{m}$  and 200  $\mu\text{m}$  of lead white.

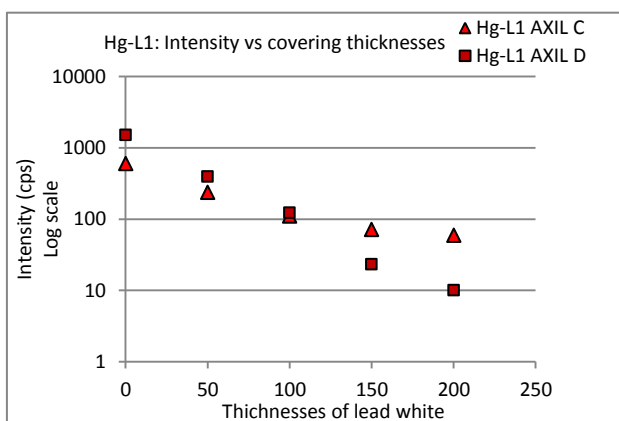
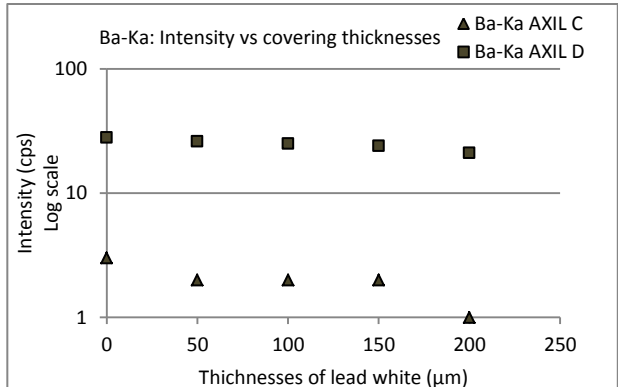
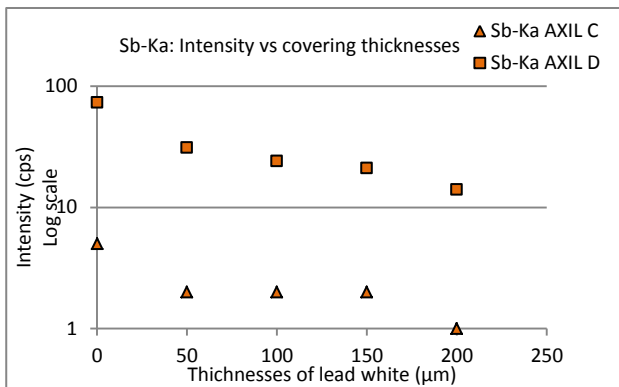
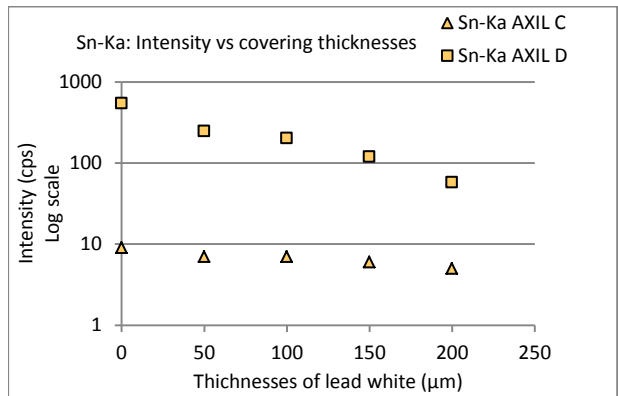
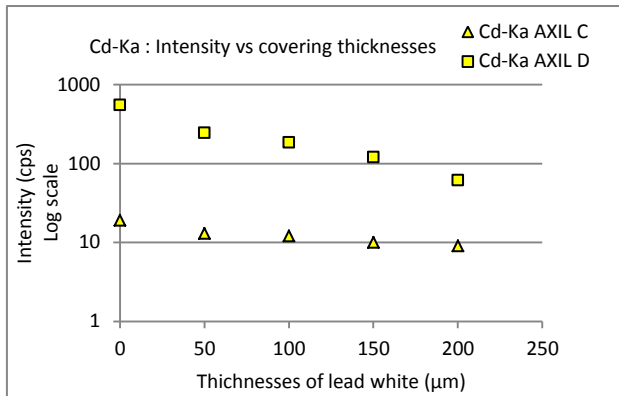
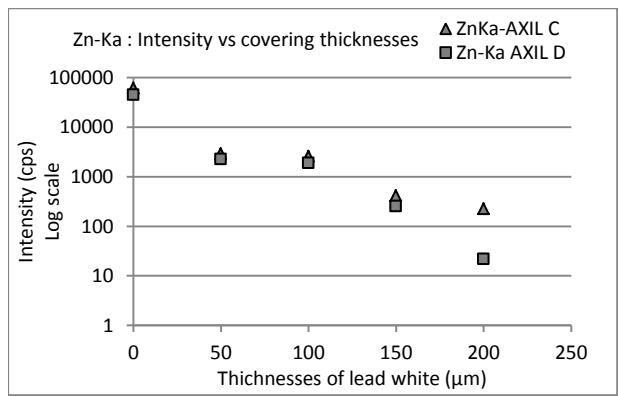
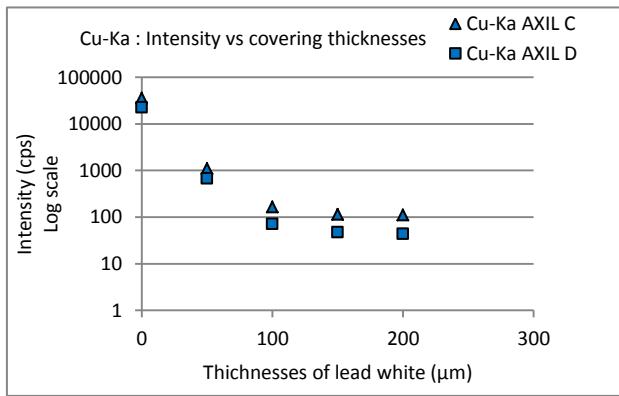
In conclusion geometry between detectors, source and sample is an important figure of merit and it becomes crucial when pigments such as yellow, which contain Cd, Sn, Sb, have to be detected. The obtained results confirm the theory: by approximating angles to 90 degrees, it is possible to minimize  $A_{\text{tot}}$  and to have better element sensitivities.

Table 3.5 Results

First scan: Source = Mo Step size = 500 $\mu\text{m}$ Time per pixel=850 $\alpha = 80^\circ$ $\beta = 25^\circ; 36^\circ; 45^\circ;$ $39^\circ$	Cu	Zn	Cd	Sn	Sb	Ba	Hg	First scan: Source = Rh Step size = 500 $\mu\text{m}$ Time per pixel=850 $\alpha = 90^\circ$ $\beta = 45^\circ$ and $47^\circ$	Cu	Zn	Cd	Sn	Sb	Ba	Hg
0 $\mu\text{m}$	xxx	xxx	x	x			xxx	0 $\mu\text{m}$	xxx	xxx	xxx	xx	xx	x	xxx
50 $\mu\text{m}$	X	X	x				xx	50 $\mu\text{m}$	x	x	xx	xx	xx	x	xx
100 $\mu\text{m}$		X	x				x	100 $\mu\text{m}$		x	xx	xx	xx	x	x
150 $\mu\text{m}$			x				x	150 $\mu\text{m}$			xx	xx	xx	x	x
200 $\mu\text{m}$								200 $\mu\text{m}$			x	x	x	x	x

Table 3.6 Intensity (cps) for each element.

1st scan Mo-anod Geometry: $\alpha = 80^\circ$ $\beta = 25^\circ; 36^\circ; 45^\circ; 39^\circ$	CuKa Average Intensity (cps)	ZnKa Average Intensity (cps)	CdKa Average Intensity (cps)	SnKa Average Intensity (cps)	SbKa Average Intensity (cps)	BaKa Average Intensity (cps)	HgL1 Average Intensity (cps)
0 $\mu\text{m}$	36180	61566	19	9	5	3	599
50 $\mu\text{m}$	1117	2945	13	7	2	2	236
100 $\mu\text{m}$	166	2609	12	7	2	2	110
150 $\mu\text{m}$	116	417	10	6	2	2	71
200 $\mu\text{m}$	112	228	9	5	1	1	59
1st scan Rh-anod Geometry: $\alpha = 90^\circ$ $\beta = 45^\circ$ and $47^\circ$	CuKa Average Intensity (cps)	ZnKa Average Intensity (cps)	CdKa Average Intensity (cps)	SnKa Average Intensity (cps)	SbKa Average Intensity (cps)	BaKa Average Intensity (cps)	HgL1 Average Intensity (cps)
0 $\mu\text{m}$	22819	45360	548	545	73	28	1510
50 $\mu\text{m}$	680	2271	243	247	31	26	393
100 $\mu\text{m}$	72	1910	183	202	24	25	122
150 $\mu\text{m}$	48	255	120	120	21	24	23
200 $\mu\text{m}$	44	22	61	58	14	21	10



**Graphics 3.1** Comparison of AXIL C scanner and AXIL D scanner by plotting K-Lines Intensity vs Thicknesses of Lead White.

Observing the Table 3.6 and the plotted Graphics 3.1, the quantitative data carried out with PyMca software reflect the results observed in the elemental dispersive maps. Counts per second decrease with the growth of lead white. In particular Cu and Zn show a strong difference in Intensity from 0 level to the others.

The K-line intensity for elements heavier than Rh (Z= 45) such as Cd, Sn, Sb and Ba are problematic. These elements are often associated with yellow pigments except for barium sulfate that is used as filler in many pigments. Their Intensities are very low, in the range of 3-19 cps for instrument C and a little bit better for instrument D in the range of 28-548 cps. The reason for this low Intensity is the choice of a polycapillary beam, which has a lower transmission for the high energy components of the primary radiation. On the other hand, observing the images from the second scan, Cd ( $K\alpha$  : 23,2 keV), Sn ( $K\alpha$  : 25,3 keV), Sb ( $K\alpha$  : 26,4 keV) and Ba( $K\alpha$  : 32,2 keV) are quite well visible under the lead white, due to their high fluorescence energies and for the geometry performing. In fact looking at Table 3.6 their XRF signals are only weakly absorbed by lead white layers.

The most heavy element Hg is detected by its L-lines ( $L_I$  : 9,98 keV ;  $L_{II}$  : 11,82 keV). Hg more or less falls in the same energy range of the K-lines of Cd, Sn, Sb and Ba. Its K-lines are not detected since it was impossible to assemble a more energetic source (Hg K-excitation energy: 83,103 keV).

A noise free visualization of hidden paint stripes may require longer dwell times than 850ms per pixel. For this reason, after analyzing the data listed above, the same sample was scanned with the instrument D (rhodium source and geometry 90°- 45°/47°) with a time per pixel greater than 850ms. This experiment will be describe in the 4<sup>th</sup> chapter. Now I will compare the two scanners M6 and AXIL to conclude the comparison of their potential.

### 3.3. M6 and AXIL scanner


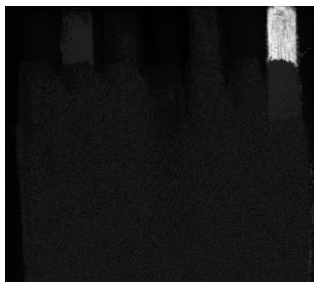
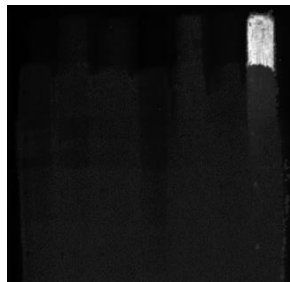
#### 3.3.1. Purpose: comparing M6 and AXIL scanner

The purpose is to compare the performance of the three instruments M6, AXIL instrument C and AXIL instrument D on the same sample (sample n. 1 covered by lead white).

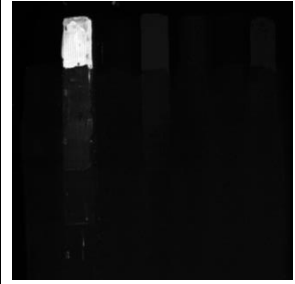
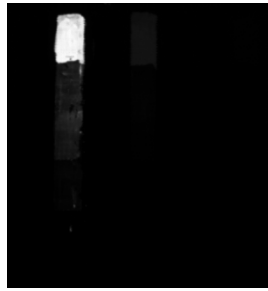
#### 3.3.2. Results

Table 3.7 Operating details of the scans.

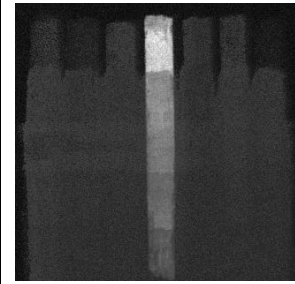
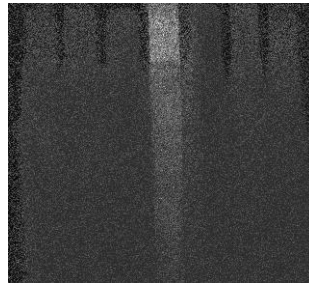
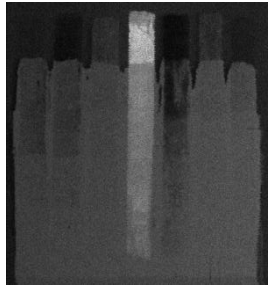
Sample n.1	Area of scan	Step size ( $\mu\text{m}$ )	Time per pixel (ms)	Total time (h)
M6 (Rh-anode)	21cm x 22cm	350	200	20 hours and 30 minutes
AXIL (C) (Mo-anode)	16,5cm x 17cm	500	850	26 hours and 30 minutes
AXIL (D) (Rh-anode)	16cm x 15,4cm	500	850	23 hours and 16 minutes

Element, atomic number, pigment	Instrument: M6 Step size ( $\mu\text{m}$ ): 350 Time per pixel (ms): 200 Source: Rh	Instrument: AXIL scanner C Step size ( $\mu\text{m}$ ):500 Time per pixel (ms):850 Geometry: $\alpha$ angle = 80° $\beta$ angles = 25°; 36°; 45°; 39° Source: Mo	Instrument: AXIL scanner D Step size ( $\mu\text{m}$ ): 500 Time per pixel (ms): 850 Geometry: $\alpha$ angle = 90° $\beta$ angle = 45° and 47° Source: Rh
Cu-K 29 Azurite			

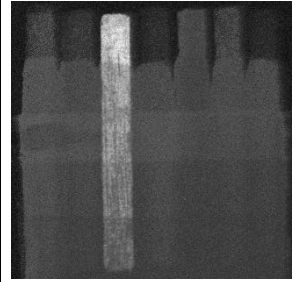
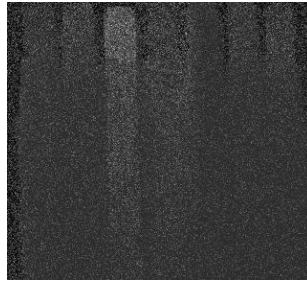
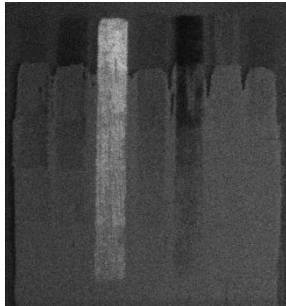
Zn-K  
30  
Zinc white



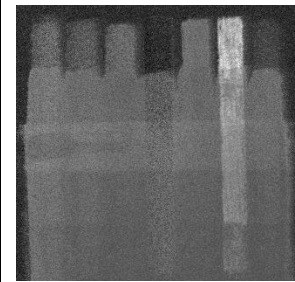
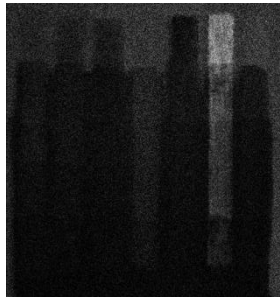
Cd-K  
48  
Cadmium yellow



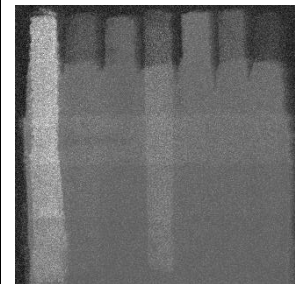
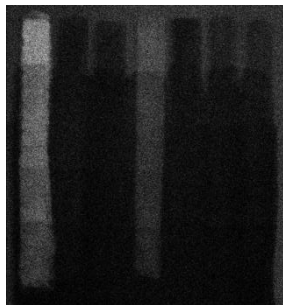
Sn-K  
50  
Lead tin yellow



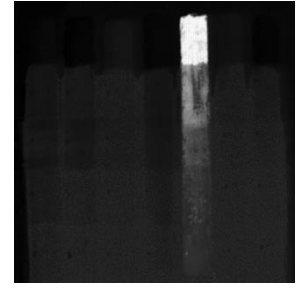
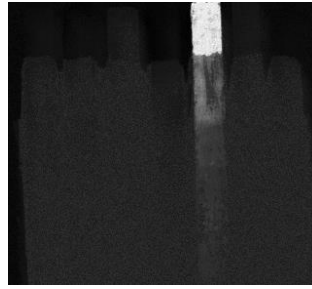
Sb-K  
51  
Naples Yellow



Ba-K  
56  
Barium sulfate



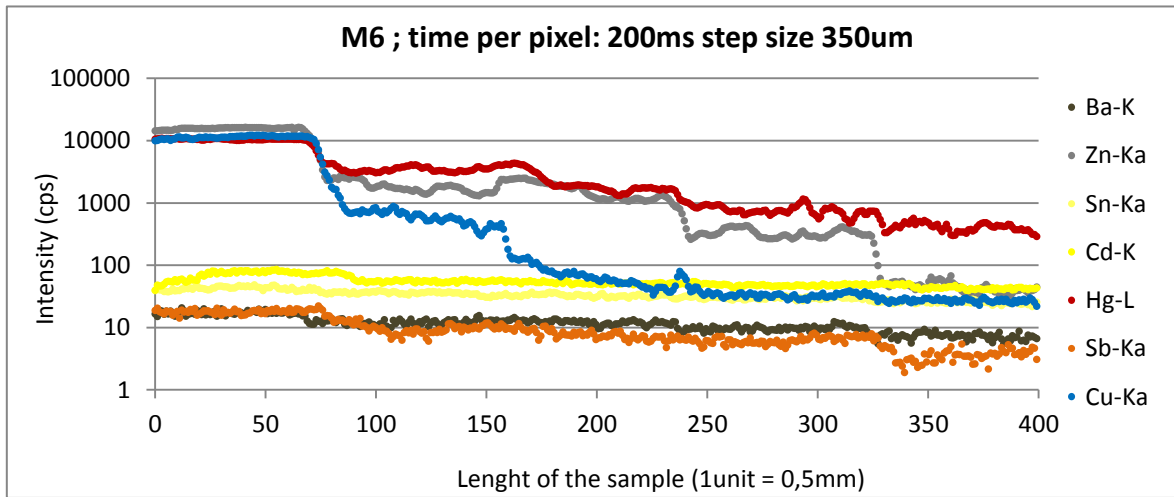
HgL  
80  
Vermilion



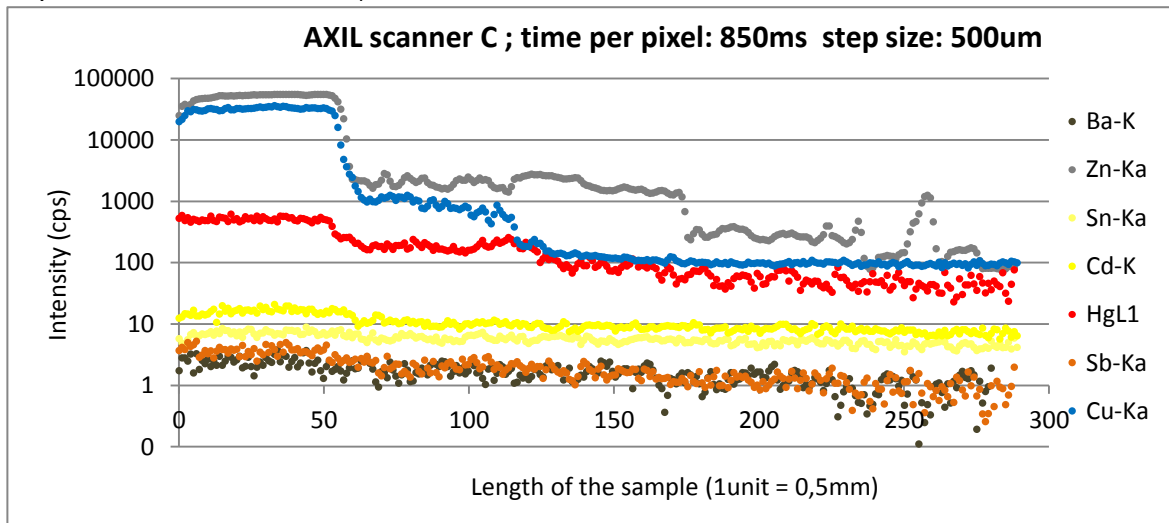
The elemental distribution images are of comparable quality with the exception of the high Z-element distribution maps such as SnK, SbK and BaK. Instrument C cannot give a clear impression of these elements distribution, while the other two instruments show quite detailed images. Looking closely at the images, it is possible to see a small resolution improvement in the images of instrument D.

The detailed maps acquired with M6 allow visualizing single characteristics of the paint strips, although its dwell time (200 ms) is much lower than the dwell time (850 ms) of AXIL scanner. Then M6 Jetsteam seems to be the best scanner because of its better resolution images, reasonable operating time and sensitivity.

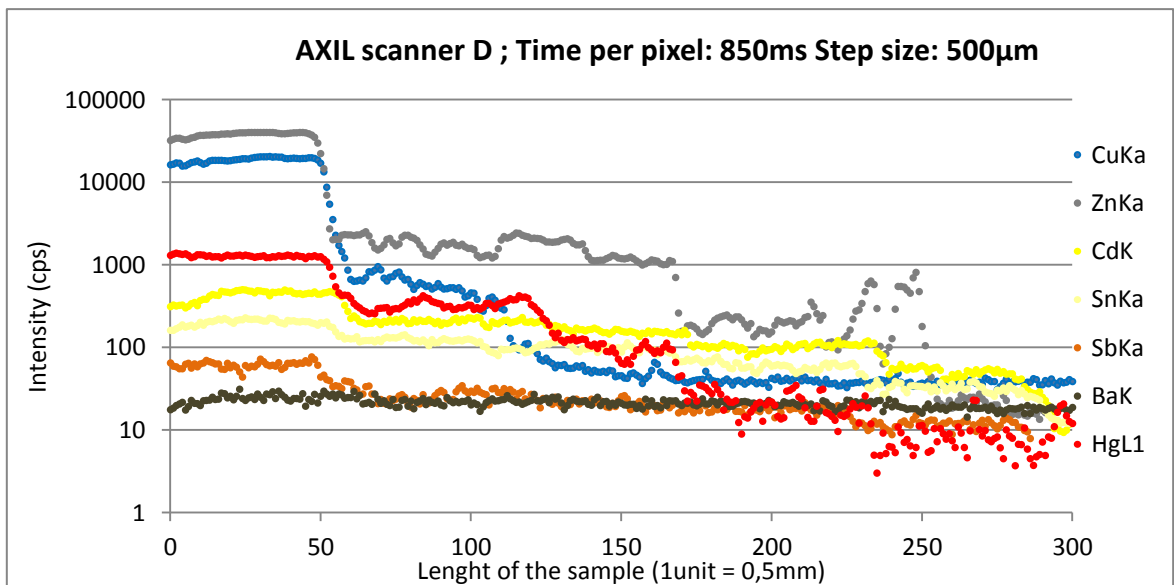
In the following graphics, line-scans for each element are plotted. On the X-axis there are the pixels distance, on the Y-axis there is the intensity for each pixel reported. The following values of intensity are the average of 30 lines of pixels taken in every strip. Data were processed with PyMca software in RGB tool.



Graphic 3.2 Line-scans of K-lines intensity carried out from M6.



Graphic 3.3 Line-scans of K-lines intensity carried out from instrument AXIL C.



Graphic 3.4 Line-scans of K-lines intensity carried out from instrument AXIL D.

The Graphics 3.2, 3.3 and 3.4 support the same results already valuated through the elemental maps, but more information can be taken. In fact, comparing the Graphic 3.2 (M6) with Graphic 3.4 (AXIL instrument D), it is clear that AXIL scanner D has a higher sensitivity for Cd, Sn, Sb and Ba. Indeed the main limitations of M6 is the lack of sensitivity for X-Ray fluorescence lines from high Z-elements.

AXIL C does not have direct advantage over the M6 Jetstream, while instrument D offers complementary data to M6, as it seems to be more sensitive for the K-level radiation of heavy elements.

The lack of sensitivity for the K-shell radiation of heavy elements is a common characteristic of all mobile instruments. The high energetic primary radiation needed is strongly scattered in the sample and difficult to shield, so that the maximum energy must be limited for radiation protection worries (Alfeld, 2013).

### 3.4 Discussion

MACRO-XRF is a powerful tool for the qualitative analysis and the determination of elemental distribution of large area. The performance depends on the measurement conditions: step size, time per pixel and geometry are crucial parameters to determine the sensitivity and the spatial resolution of the measurement. Researchers have to carefully select them according to the required analytical task. In this chapter I tested two mobile scanning MA-XRF (M6 and AXIL scanner) and I showed their potentialities and limits.

Time per pixel were tested on original sample number 1 by M6 Jetstream. Time per pixel chosen for the first scan was 50 ms, while 500 ms were chosen for the second one. Looking at the elemental maps with 500 ms per pixel, the selected elements stood out against a dark background minimizing the interference.

The only one problem was the long operating time, in fact if the instrument scans an area of 50 cm x 50 cm with a step size of 500  $\mu\text{m}$  and a dwell time of 500 ms, the analysis takes more than 2 days. Indeed for a whole painting scan, a dwell time a bit lower than 500 ms is convenient, otherwise the operating time could become too long. High time per pixel is suitable for small area of interest, for revealing small interesting details.

The pixel's dimension (step size) can affect the precision and the accuracy of the elemental maps as well. I tested 1000  $\mu\text{m}$  and 350  $\mu\text{m}$  of step size on the same sample number 1 covered by four different thicknesses of lead white. The carried out images with 1000  $\mu\text{m}$  of step size are imprecise and not sharp. In particular the high Z-element (Cd, Sn, Sb and Ba) are not recognizable, the images appear as a mosaic. On the other hand, images carried out with 350  $\mu\text{m}$  of step size are clear, the edges of the strips and details of the brush strokes are very well detected. Nevertheless, if we want to scan a painting with high resolution, it is recommended not to use a step size below 500  $\mu\text{m}$  because of the long operating time.

For the set-up of AXIL scanner, I chose a step size of 500  $\mu\text{m}$  because, as we seen above, it can give well-defined images within a reasonable time. I wanted to see if it was possible to detect other marker element in the seven pigments, so I increased the dwell time up to 850 ms per pixel. Furthermore, two set-up of geometry detector, source and sample were tested. A significant improvement in the resolution of the images was been reported using a Rh-anode instead of Mo-anode and by placing the four detectors closer to the source and sample, with an angle  $\alpha = 90$  degrees instead of 80 degrees and standardizing the angles  $\beta$  at about 45 degrees (Alfeld, 2013). Instrument D gave better results compared to instrument C, in particular for those elements difficult to be detected and for hidden paint layers. The observations on elemental distribution maps were confirmed by the fluorescence intensities carried out by PyMca software and visible on Table 3.6 and in the Graphics 3.1.

Using comparable parameters, scans of M6 and AXIL scanner were observed on the same sample. Elemental maps carried out from M6 and AXIL D seem to be quite the same, but, observing the line-scans (Graphics 3.2 - 3.3 -3.4), different capability is observed. For low Z-elements (Cu and Zn) not covered by lead white, AXIL C gives the best results, while for paint layers covered by lead white, the capability of M6 and AXIL D are the best. AXIL D rather than M6 better detected the more problematic high Z-elements. The reason for this low sensitivity is the choice of a polycapillary as beam optic. The polycapillary optic



attenuates the high energetic part of the primary radiation and the single detector in M6 covers a smaller solid angle than the four SDDs in instrument D. However the results obtained, M6 could be the most versatile scanner among those investigated and data could be better than those presented in this project, since M6 was used with 200 ms per pixel instead of 850 ms. M6 allows to acquire high resolution elemental distribution images with reasonable sensitivity and its software package is much more simple and intuitive, so even the less expert will use it. Its main limitation (as it is mentioned in (Alfeld, 2013) )is the lack of sensitivity for X-ray fluorescence lines above 20 keV, in our case above cadmium X-ray fluorescence K-line: 23,17 keV. The limitation might be overcome by installing a collimator optic in front of the X-ray tube or using AXIL instrument D, which is more sensitive to K-level radiation of heavy elements.

## CHAPTER 4

### INSTRUMENT AND METHOD: QUANTITATIVE ANALYSIS

In the specific field of non-destructive analysis of irregular and heterogeneous materials, the use of conventional XRF for quantitative analysis is limited by the usually large area of investigation, moreover the non-ideal and irregular sample surface can introduce systematic errors. In order to overcome the obstacle of large and bulky object, mobile instrumentation with a comfortable accommodation for object have been invented (Janssens. & Grieken, 2004). In this chapter AXIL scanner will be tested with the intention of collecting suitable quantitative data or at least a meaningful trend.

#### 4.1. Purpose: sensitivity and limit of detection

The fluorescence radiation emitted from a sample, that is exposed to an X-ray beam, contains qualitative and quantitative information about the elements present in the sample. Now I will see if MA-XRF allows to achieve good quantitative data through the calculation of sensitivity and limit of detection. I analyzed three samples on the model of the sample number 1, already investigated in the third chapter. The three samples were scanned by means of AXIL scanner D because its set-up gave the best results (Chapter 3).

##### 4.1.1 Sensitivity (Janssens, 2013)

To be considered a complete and competitive investigation technique, MA-XRF has to give good quantitative results, in addition to excellent qualitative data. During the last years, studies of quantitative analysis with XRF have showed a linear relation between the Net X-ray intensity ( $N_i$ ) and the irradiated mass ( $m_i$ ), which usually is also proportional to the concentration ( $c_i$ ) of that element in the sample:

$$N_i = S_i \times m_i \times t \quad (4.1.1.1)$$

$$\text{or } N_i = S_i \times c_i \times t \quad (4.1.1.2)$$

$N_i$  = Net X-ray intensity of a given characteristic line of element  $i$   
 $S_i$  = sensitivity coefficients of the element (expressed in counts  $s^{-1}/(g \text{ cm}^{-3})$ )  
 $m_i$  = irradiated mass  
 $c_i$  = concentration of the element  
 $t$  = analysis time

The equation above is true only for thin film samples. In reality a total intensity ( $T_i$ ) is measured, since it is not possible to directly obtain the  $N_i$ .  $T_i$  is the sum of  $N_i$  and the background intensity ( $B_i$ ). The latter value is the sum of different radiations contributions:  $B_i$  scatter +  $B_i$  detector +  $B_i$  overlap +  $B_i$  blank.

When the magnitude of  $B_i$  is experimentally determined and this measurement is repeated  $n$  times, the results will be distributed around a mean value  $\langle B_i \rangle$  with its standard deviation ( $st.dev._B$ ).

$$N_i = \langle B_i \rangle + Kst. dev._B \quad (4.1.1.3)$$

$N_i$  = Net X-ray intensity of a given characteristic line of element  $i$   
 $\langle B_i \rangle$  = mean value of background intensity  
 $K$  = constant  
 $st.dev._B$  = standard deviation of the background intensity

For these reasons, instead of the Net X-Ray intensity collected over a specific time  $t$ , it is often more convenient to use the Net X-Ray count rate  $R_i$ .

$$R_i = N_i/t = S_i \times C_i \quad (4.1.1.4)$$

$R_i$  = count rate

$N_i$  = Net X-ray intensity of a given characteristic line of element  $i$

$t$  = analysis time

$S_i$  = sensitivity coefficients of the element

$c_i$  = concentration of the element

The sensitivity coefficients are proportionality constants for the elements collected and are important instrument's figures of-merit. In fact by relating the sensitivity coefficients, it is possible to compare the power of different instruments and find the concentration of the element in analysis.

#### 4.1.2. Limit of detection

Another important figure of merit is the Limit of Detection. The Union of Pure and Applied Chemistry (IUPAC) defines the limit of detection as "the lowest concentration level that can be determined to be statistically significant from an analytical blank" (Gary, Long, & Winefordner., June 1983). Therefore, limit of detection is derived from the smallest measure ( $Y_L$ ) that can be detected with reasonable certainty.

$$Y_L = Y_{bl} + K \text{ st. dev.}_{bl} \quad (4.1.2.1)$$

$$\text{LOD} = \frac{K \text{ st. dev.}_{bl}}{S'} \quad (4.1.2.2)$$

$Y_L$  = smallest measure

$Y_{bl}$  = mean of the blank responses

$K$  = constant

$\text{st. dev.}_{bl}$  = standard deviation of the blank responses

$S'$  = Sensitivity (count.sec<sup>-1</sup> per concentration unit)

Thus the detection limit decreases with the growing of sensitivity and increases with the standard deviation. Detection limits are useful figures of-merit as it is important to know the lowest concentration (or mass) level at which the spectrometer can be used for qualitative or quantitative determinations. Usually the detection limit is related to three times the standard deviation ( $K=3$ ), corresponding to a statistical confidence level of 99% (Van Grieken & and Markowicz, 2002.) .

## 4.2 Methodology

For this part of research, I carried out three scans for each mockup (three wood samples). Using the instrument AXIL D, the three scans were performed with the same step size of 500 $\mu\text{m}$  and a time per pixel of 850ms for the first scan, 1000ms for the second and 2500ms for the third.

The goal is to calculate the sensitivity and the limit of detection for the main and significant element (marker element) present in each pigment.

Since the fluorescence intensity depends on the different thicknesses of the covered lead white layers, we cannot directly consider the Net X-ray count rate ( $R_i$ ) recorded by the detector. It was therefore necessary to devise a method to select the Net X-ray count rate from the five levels created on each strip of pigment: first level without lead white, second level covered by 50  $\mu\text{m}$  of lead white, third level by 100  $\mu\text{m}$  of lead white, fourth level by 150  $\mu\text{m}$  of lead white and the fifth level by 200  $\mu\text{m}$  of lead white. In order to overcome this problem, I used the "RGB correlator" option presents in the PyMca software, where it is possible to select one or more elements visible in the spectrum. Once the element is selected, the sample

image appears in black and white, the white corresponds to the element selected and the rest will be black. By using the command “line profile selection”, it is possible to track single or multiple lines on the image (each line has a width of one pixel) and a “scan window” simultaneously appears with a preview line-scan graphic: on Y-axis there are fluorescence intensities and on X-axis the distances. In my case a grid of 30 lines was suitable and the resulting file was then treated in Excel. In conclusion data were processed in Excel to calculate: average fluorescence intensity, standard deviation, sensitivity and LOD for the five levels in each of the seven markers

I will not report all results obtained from the nine scans (three scans for each of the three sample), but I will show only the best results for each element.

#### 4.2.1 Calculation

In this project, samples are composed by seven pigment strips covered by different thick layers of lead white. M6 and AXIL scanner have a polychromatic forms of excitation, so that the equation for  $R_i$  calculation is quite complicated and involves an integral over the intensity distribution of the X-ray source. In general, if a sample with thickness  $d$  and density  $\rho$  is analyzed by polychromatic excitation, the observed XRF count rate  $R_i$  (for  $K\alpha$ -line of an element  $i$ ), can be written as:

$$R_{i,K\alpha} = \int_{E=E_{i,abs}}^{E_{max}} I_0(E) \frac{G_1}{\sin\theta} \sigma_{i,K\alpha}(E) C_i H_i(E) e^{-X(E,E_{i,K\alpha})\rho z} G_2 B(E, E_{i,K\alpha}) \varepsilon(E_{i,K\alpha}) dz dE \quad (4.2.1.1)$$

After the integration over the sample depth, equation (4.2.1.1) becomes:

$$R_{i,K\alpha} = \int_{E=E_{i,abs}}^{E_{max}} I_0(E) \frac{G_1 \rho d}{\sin\theta} \sigma_{i,K\alpha}(E) C_i \times \frac{1 - e^{-X(E,E_{i,K\alpha})\rho d}}{X(E, E_{i,K\alpha})\rho d} \times G_2 B(E, E_{i,K\alpha}) \varepsilon(E_{i,K\alpha}) dE \quad (4.2.1.2)$$

$E_{i,abs}$  = absorption edge energy

$E_{i,K\alpha}$  =  $K\alpha$ -line energy

$I_0(E)dE$  = spectral distribution of the exciting radiation

$\sigma_{i,K\alpha}$  = cross-section for the production of  $K\alpha$  radiation

$G_1$  and  $G_2$  = geometry constants

$B(E, E_{i,K\alpha})$  = absorption of the radiation in the medium between tube, sample and detector

$\varepsilon(E_{i,K\alpha})$  = efficiency of the detector

A set of this equations can be written for each element present in the sample and they can be solved making the method computationally complex. Although this is the appropriate equation for our instrument set-up, data were processed with the formula for monochromatic forms of excitation, which was supposed to be enough to get a reliable trend data.

Using monochromatic forms of excitation (with energy  $E_0$ ) for a single homogeneous layer and in absence of enhancement phenomena, the observed XRF count rate  $R_i$  of an element  $i$  (with energy  $E_i$ ) is related in the following manner:

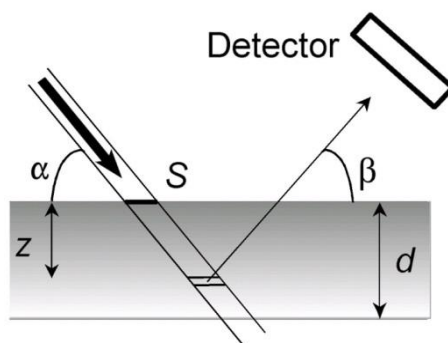


Figure 4.1 XRF irradiation geometry on single layer sample.

$$R_i = S_i m_i \frac{1 - e^{-X(E_0, E_i) \rho d}}{X(E_0, E_i) \rho d} = S_i m_i A_i \quad (4.2.1.3)$$

$$R_i = S_i S c_i \frac{1 - e^{-X(E_0, E_i) \rho d}}{X(E_0, E_i)} = S_i c_i A_i \quad (4.2.1.4)$$

$$\text{With: } X(E_0, E_i) = \mu(E_0) \text{csc}\alpha + \mu(E_i) \text{csc}\beta \quad (4.2.1.5)$$

$$m_i = \rho_i d_i S c_i \quad (4.2.1.6)$$

$\alpha$  = angle at which the X-rays arrive to the sample surface  
 $\beta$  = angle at which the X-rays leave the sample surface  
 $\rho$  = density of the pigment  
 $S'$  = sensitivity of the element  $i$   
 $A_i$  = absorption factor  
 $m_i$  = irradiated mass  
 $S$  = spot size

$A_i$  is the absorption factor, which is obtained by adding all contributions to  $R_i$  produced in a series of infinitesimal sample volumes at various depths  $z$  inside the sample and by considering the sum of two attenuation factors:  $\exp[-\mu(E_0) \text{csc}\alpha p z]$  for the primary radiation  $E_0$  and  $\exp[-\mu(E_i) \text{csc}\beta p z]$  for the fluorescent radiation  $E_i$ .

A more accurate observation at the Formula 4.2.1.3 helps us to understand that when  $d$  approaches to zero (very thin layers), the factor  $A_{i1}$  become equal to 1 so that the observed count rate becomes proportional to the irradiated mass  $m_i$  and thus proportional to both  $c_i$  and  $d$ . On the other hand, when  $d$  approaches to infinite (very thick layers), the factor  $A$  become equal to  $1/\chi$  so that the observed count rate becomes proportional to the concentration  $c_i$  and is no longer a function of  $d$ .

In our case, we can only use the Formula 4.2.1.3 for the 0 level (level not covered by lead white). In fact for the others levels, the Intensity derived from a single homogeneous layer of density  $\rho_2$  and thickness  $d_2$ , covered by a single homogeneous layer of  $\rho_1$  and thickness  $d_1$  not containing element  $i$ , is influenced by the absorption factor of the covered layer. The formula can be written as:

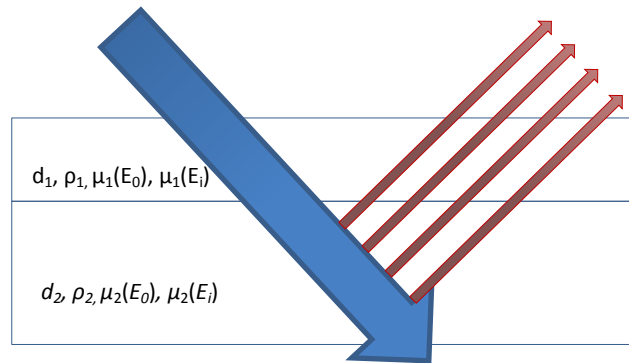


Figure 4.2. XRF irradiation geometry on multilayered sample.

$$R_{2i} = S'_i m_{2i} \frac{1 - e^{-X_2(E_0, E_i) \rho_2 d_2}}{X_2(E_0, E_i) \rho_2 d_2} e^{-X_1(E_0, E_i) \rho_1 d_1} = S'_i m_{2i} A'_{2i} a_{1i} \quad (4.2.1.7)$$

$$R_{2i} = S'_i S c_{2i} \frac{1 - e^{-X_2(E_0, E_i) \rho_2 d_2}}{X_2(E_0, E_i) \rho_2 d_2} e^{-X_1(E_0, E_i) \rho_1 d_1} = S_i c_{2i} A'_{2i} a_{1i} \quad (4.2.1.8)$$

$$\text{With: } X_2(E_0, E_i) = \mu_2(E_0)\text{csc}\alpha + \mu_2(E_i)\text{csc}\beta \quad (4.2.1.9)$$

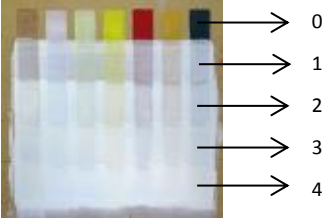





$$X_1(E_0, E_i) = \mu_1(E_0)\text{csc}\alpha + \mu_1(E_i)\text{csc}\beta \quad (4.2.1.10)$$

$e^{-X_1(E_0, E_i)\rho_1 d_1}$  = Absorption factor of lead white

$\frac{1 - e^{-X_2(E_0, E_i)\rho_2 d_2}}{X_2(E_0, E_i)\rho_2 d_2}$  = Absorption factor of the pigment

## 4.2.2 Results

### Sample 2: Azurite $\text{Cu}_3(\text{CO}_3)_2(\text{OH})_2$

Description	Samples taken from the five levels 
0 level Azurite average thickness: 24,50 $\mu\text{m}$	 4X magnification
1 level Azurite average thickness: 21,46 $\mu\text{m}$ Lead white average thickness: 58,65 $\mu\text{m}$	 4X magnification
2 level Azurite average thickness: 30,85 $\mu\text{m}$ Lead white average thickness: 76,96 $\mu\text{m}$	 4X magnification
3 level Azurite average thickness: 22,66 $\mu\text{m}$ Lead white average thickness: 91,53 $\mu\text{m}$	 4X magnification
4 level Azurite average thickness: 23,61 $\mu\text{m}$ Lead white average thickness: 126,67 $\mu\text{m}$	 4X magnification

**Table 4.1** Cross sections of five samples taken from azurite paint layer.

Azurite	0 level	1 level		2 level		3 level		4 level	
	$\mu\text{m Cu}$	$\mu\text{m Cu}$	$\mu\text{m Pb}$	$\mu\text{m Cu}$	$\mu\text{m Pb}$	$\mu\text{m Cu}$	$\mu\text{m Pb}$	$\mu\text{m Cu}$	$\mu\text{m Pb}$
Values taken on the cross sections photos by Dino Capture	23,52	21,01	65,83	28,01	84,03	18,21	92,44	21,54	120,29
	31,32	16,81	49,02	35,01	82,63	18,21	86,83	14,36	134,65
	31,32	19,81	58,82	35,01	81,23	21,06	93,84	21,62	122,08
	27,96	23,81	65,83	25,37	79,83	28,01	81,23	23,34	120,29
	24,61	30,81	56,02		64,43	28,05	84,14	41,29	116,70
	25,75	15,08	58,82		63,78	22,41	93,84	21,54	140,04
	25,73	28,01	56,02		75,68		79,94	21,54	134,65
	22,37	18,21	58,82		84,03		98,04		113,11
	16,78	19,61					113,45		138,24
15,66									
<b>Average Thicknesses:</b>	<b>24,50</b>	<b>21,46</b>	<b>58,65</b>	<b>30,85</b>	<b>76,96</b>	<b>22,66</b>	<b>91,53</b>	<b>23,61</b>	<b>126,67</b>

Table 4.2 Calculation of average thicknesses for azurite and lead white

In the tabel above there are a list of thicknesses taken from the five samples shown in the page before. The layers are more or less homogeneous, except the 2 layer of Azurite, that is 10 $\mu\text{m}$  thicker than the others. The lead white layers grow homogeneously from 58,65 $\mu\text{m}$  to 126,67 $\mu\text{m}$ .

Below an outline of the mockup in section shows the layers thicknesses:



Figure 4.3. Outline of azurite structure



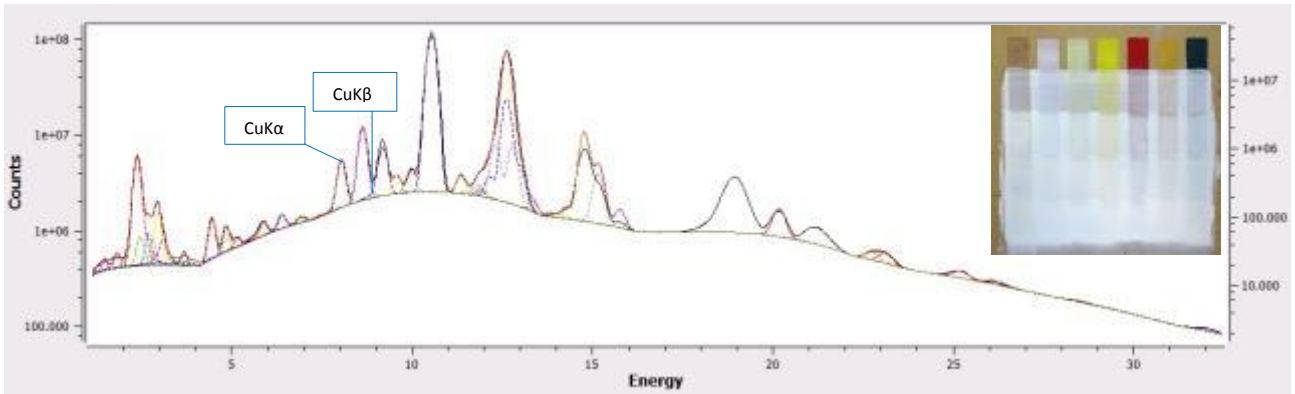


Figure 4.4. Spectra of the second sample. Below the blue lines highlight the Cu-K $\alpha$  and Cu-K $\beta$  peaks.

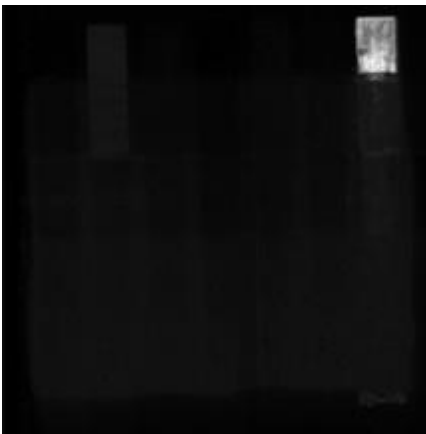


Figure 4.5 a. Cu-K map; 850ms time per pixel and 500 $\mu$ m step size

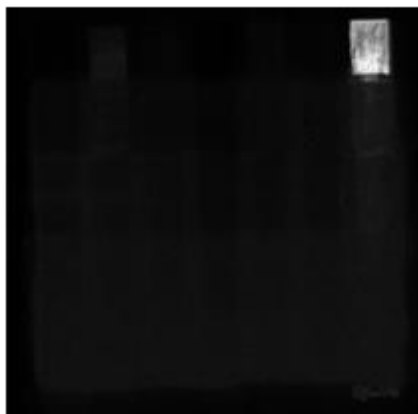
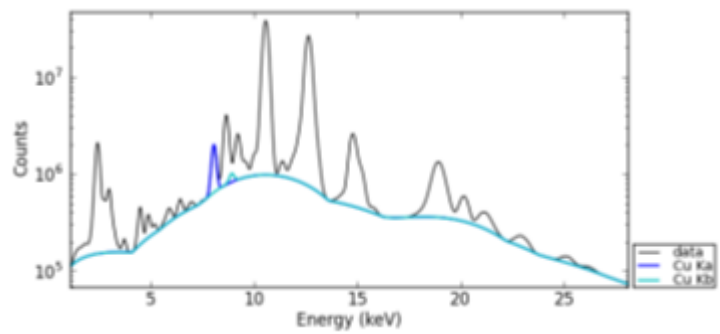


Figure 4.5 b. Cu-K map; 1000ms time per pixel and 500 $\mu$ m step size.

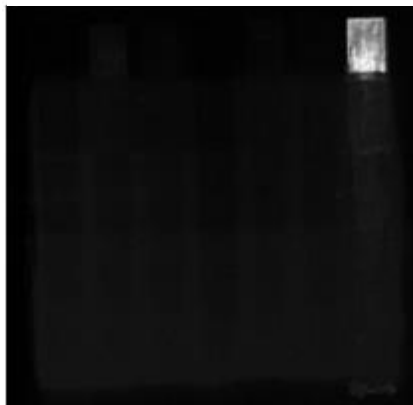
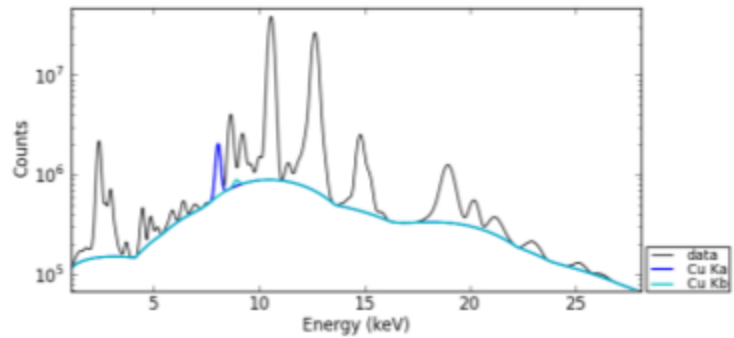
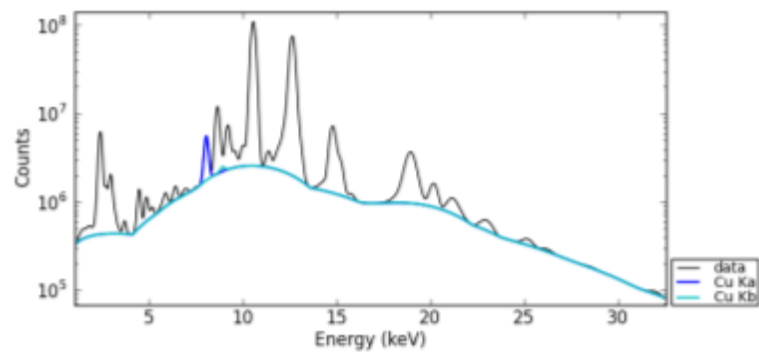


Figure 4.5 c. Cu-K map; 2500ms time per pixel and 500 $\mu$ m step size.



In the table below there are data of azurite pigment analyzed and data for the calculation of sensitivity and limit of detection.

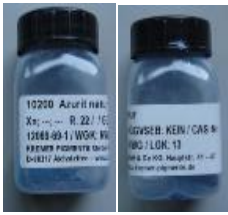


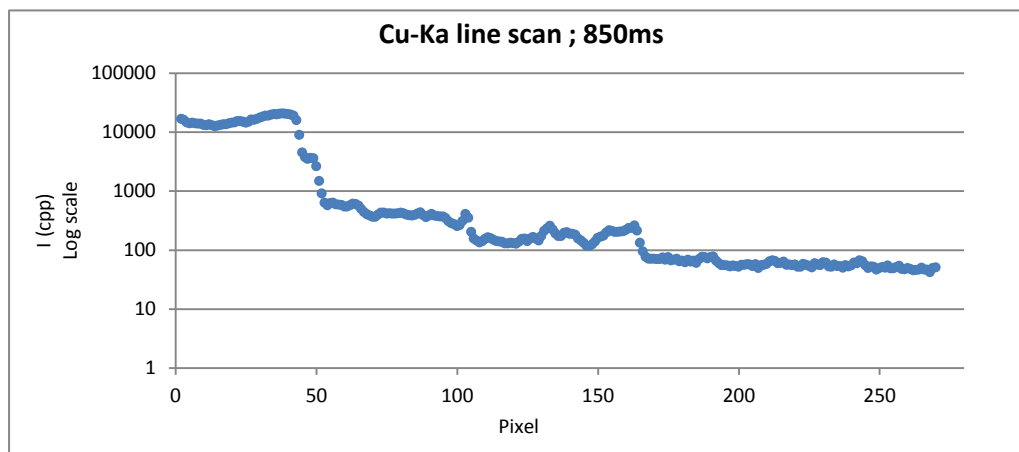
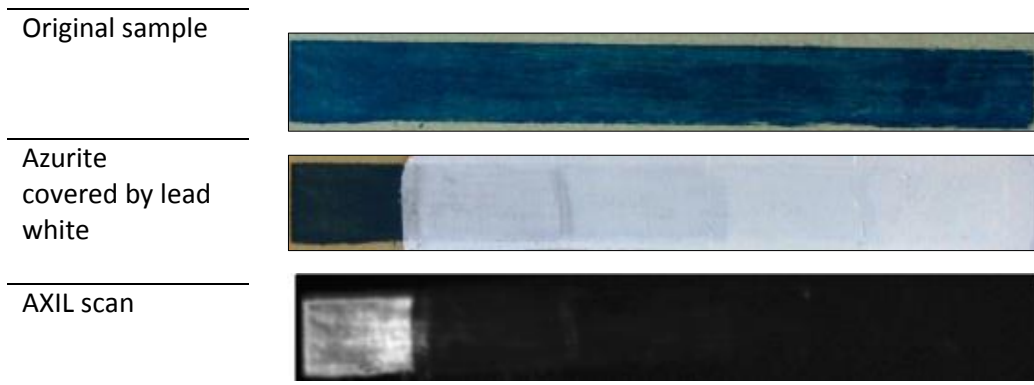
Figure 4.6. Pigment used in the study

<b>Element of interest</b>	Copper (Cu)	<b>X-Ray excitation energy for Cu-K</b>	K = 8,979 KeV
<b>Pigment provenience</b>	Kremer	<b>mass attenuation coefficient (<math>\mu_0</math>)</b>	138,5 cm <sup>2</sup> /g
<b>Atomic Number (Z)</b>	29	<b>X-Ray fluorescent energy for Cu-K<math>\alpha</math></b>	K $\alpha$ = 8,047 KeV
<b>Density of lead white (<math>\rho</math>)</b>	5,11 g/cm <sup>2</sup>	<b>mass attenuation coefficient (<math>\mu_f</math>)</b>	182,4 cm <sup>2</sup> /g
<b>Density of pigment (<math>\rho</math>)</b>	3,11 g/cm <sup>2</sup>	<b>Cos<math>\alpha</math></b>	0,000
<b>Concentration (C<sub>i</sub>)</b>	55,31	<b>Cos<math>\beta</math></b>	0,707
<b>Levels</b>		<b>Absorption factor for Pb (A<sub>1</sub>)</b>	<b>Absorption factor for Cu (A<sub>2</sub>)</b>
0 level		1,000	0,637
1 level		0,920	0,671
2 level		0,897	0,574
3 level		0,879	0,657
4 level		0,836	0,647
		<b>Irradiated mass (mg)</b>	
		4,21	
		3,69	
		5,30	
		3,89	
		4,05	

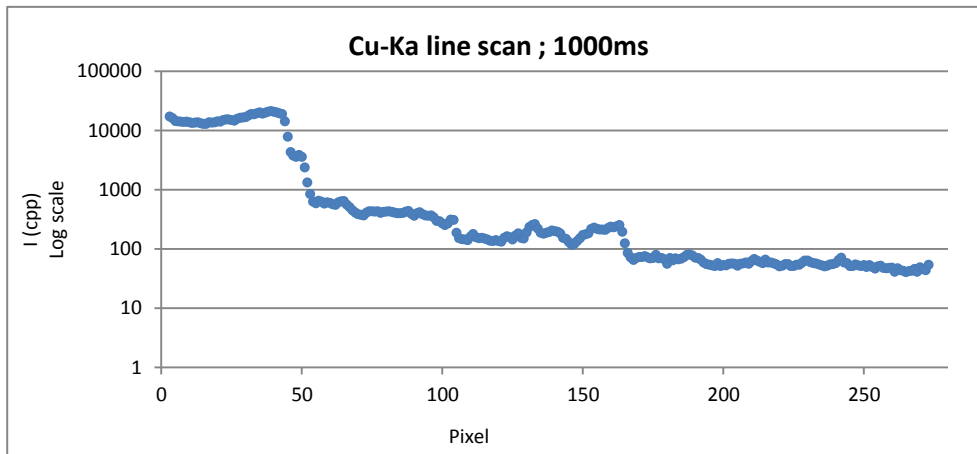
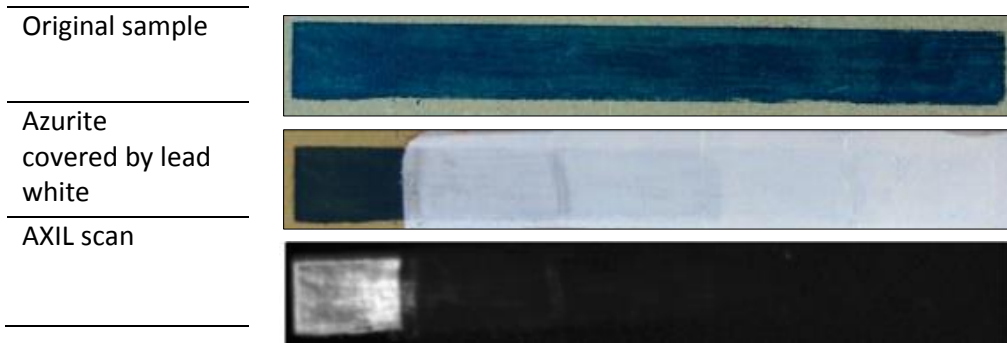
Table 4.3. Data for the quantitative analysis of Cu.

Results for:

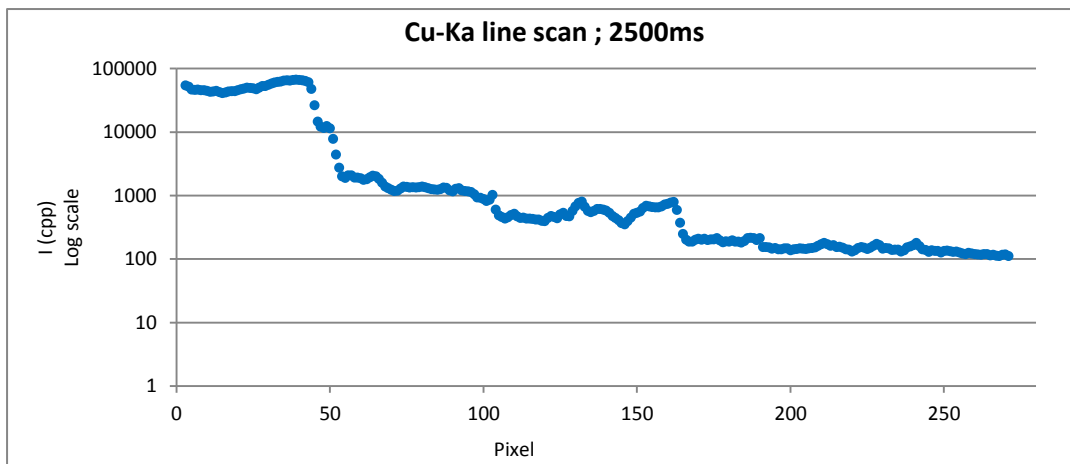
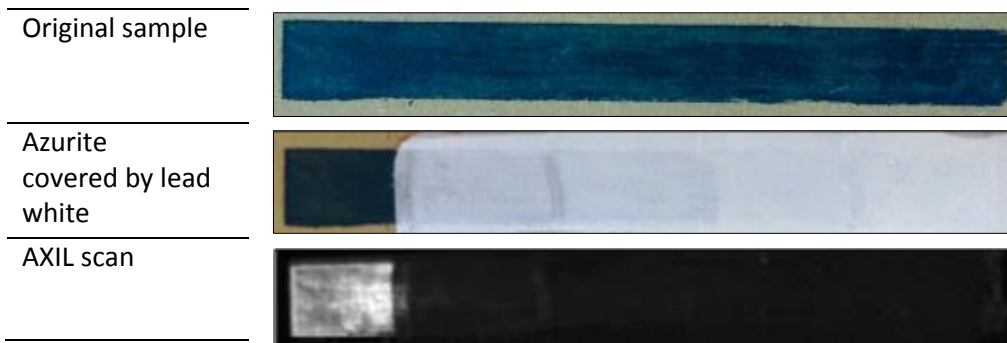
Instrument AXIL D; Time per Pixel: 850ms ; Step size: 500 $\mu$ m; Total time: 22 hours and 50minuts



Results for:  
instrument: AXIL D; Time per Pixel: 1000ms; Step size: 500µm; Total time: 26 hours and 52 minutes



Results for:  
Instrument: AXIL; Time per Pixel: 2500ms; Step size: 500µm; Total time: 67 hours and 10 minutes



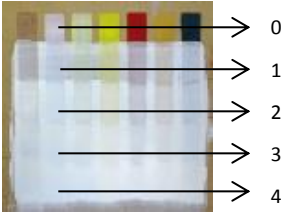





<b>SCAN: 850ms 500µm</b>	<b>Intensity average (cps)</b>	<b>St.Dev.</b>	<b>Sensitivity (cpp/mg)</b>	<b>Limit of Detection (µg)</b>
0 level	18676	3044,13	6966	1311
1 level	507	117,39	223	1581
2 level	200	43,33	73	1776
3 level	74	9,14	33	829
4 level	61	6,09	28	662
<b>SCAN: 1000ms 500µm</b>				
0 level	15819	2864,52	5901	1456
1 level	438	105,10	192	1638
2 level	176	38,61	64	1797
3 level	62	8,09	28	875
4 level	55	6,91	25	821
<b>SCAN: 2500ms 500µm</b>				
0 level	20695	3402,86	7719	1322
1 level	586	127,20	258	1482
2 level	214	47,08	78	1801
3 level	69	10,39	31	1015
4 level	52	6,15	24	776

**Table 4.4.** Results for Cu

Intensity and sensitivity decrease considerably with the growth of lead white thicknesses. The highest values of sensitivities are of course in the 0 level, between 6000cps/mg and 7700cps/mg. The sensitivity is very low for the 2, 3 and 4 levels, these values correspond perfectly to what is observed in elemental maps, where only 0 and 1 levels are visible.

Limit of detection increases with the growth of the lead white thickness up to the 2 level). Effectively it is necessary more pigment under a thick covering layer to let copper detected.

## Sample 2: Zinc White ZnO

Description	Sample taken from the five levels 
0 level Zinc white average thickness: 26,04 $\mu\text{m}$	 Magnification: 4X
1 level Zinc white average thickness: 21,36 $\mu\text{m}$ Lead white average thickness: 19,47 $\mu\text{m}$	 Magnification: 5X
2 level Zinc white average thickness: 30,24 $\mu\text{m}$ Lead white average thickness: 40,32 $\mu\text{m}$	 Magnification: 4X
3 level Zinc white average thickness: 38,57 $\mu\text{m}$ Lead white average thickness: 83,33 $\mu\text{m}$	 Magnification: 4X
4 level Zinc white average thickness: 30,82 $\mu\text{m}$ Lead white average thickness: 108,74 $\mu\text{m}$	 Magnification: 5X

**Table 4.5.** Cross sections of the five samples taken from zinc white paint layer.

Zinc White	0 level	1 level		2 level		3 level		4 level	
	µm Zn	µm Pb	µm Zn	µm Pb	µm Zn	µm Pb	µm Zn	µm Pb	µm Zn
Values taken on the cross sections photos by Dino Capture	22,40	21,01	23,81	44,79	22,40	69,00	35,91	120,29	30,52
	22,40	18,21	21,01	40,38	29,12	100,60	39,50	113,11	25,13
	42,55	14,01	19,61	42,55	40,31	57,45	32,32	89,84	28,73
	17,92	21,01	21,01	40,31	26,88	122,08	45,03	111,31	30,52
	26,88	21,42		33,59	35,83	78,99	44,88	100,54	19,75
	33,59	19,61		40,31	26,88	71,84	36,31	96,95	26,93
	17,92	21,01			33,59		36,09	107,72	39,50
	24,64				26,88			95,22	46,68
							143,67	30,52	
<b>Average Thicknesses:</b>	<b>26,04</b>	<b>19,47</b>	<b>21,36</b>	<b>40,32</b>	<b>30,24</b>	<b>83,33</b>	<b>38,57</b>	<b>108,74</b>	<b>30,92</b>

Table 4.6 Calculation of average thicknesses for zinc white and lead white

Looking at the table above, layers are more or less homogeneous, except the 1 layer (21,36 µm) and the 3 layer (38,57 10µm) of zinc white. The lead white layers grow homogeneously from 19,47µm to 108,74 µm.

Below there is an outline of the mockup in section:



Figure 4.7. Outline of Zinc white structure

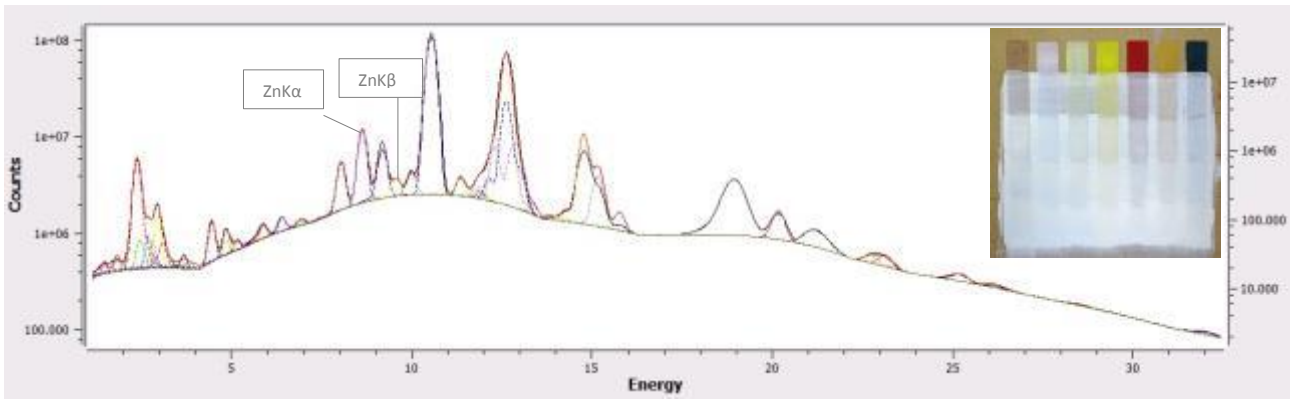


Figure 4.8 Spectra of the second sample. Below the black and gray lines highlight the ZnK $\alpha$  and ZnK $\beta$  peaks.

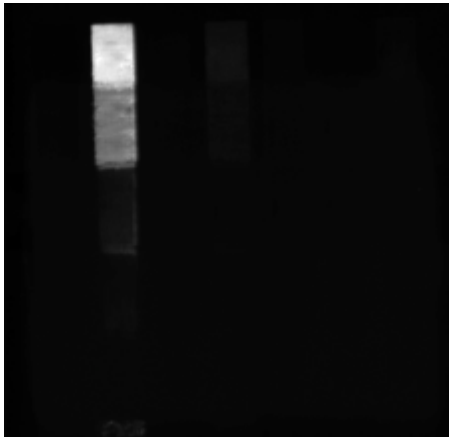


Figure 4.9 a. Zn-K map; 850ms time per pixel and 500 $\mu$ m step size.

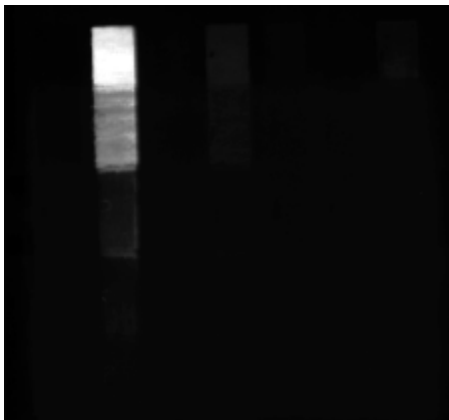
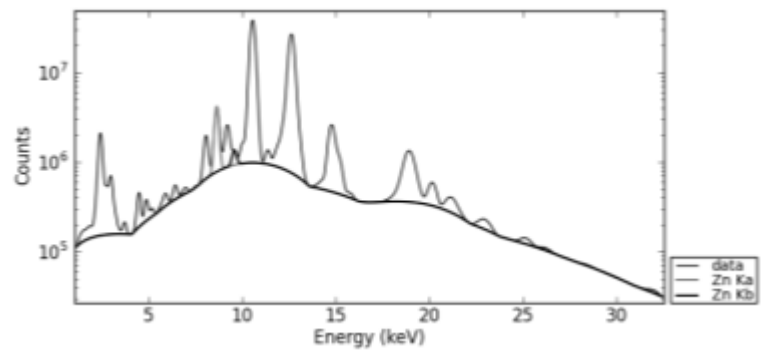


Figure 4.9 b. Zn-K map; 1000ms time per pixel and 500 $\mu$ m step size.

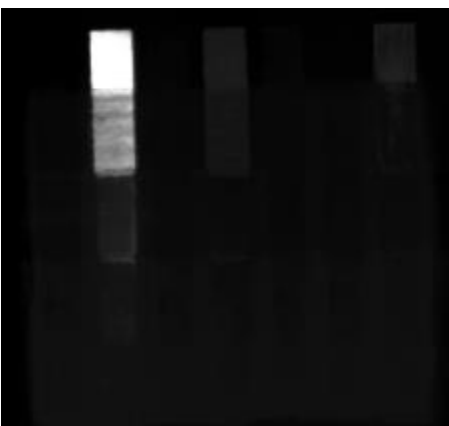
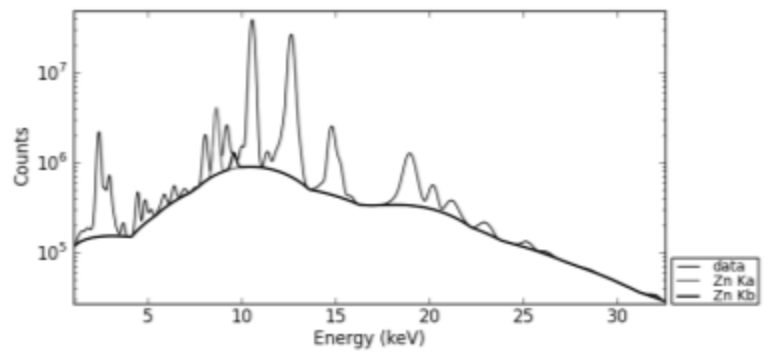
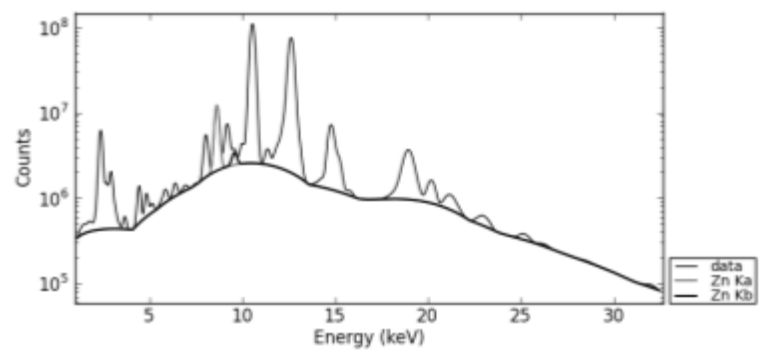


Figure 4.9 c. Zn-K map; 2500ms time per pixel and 500 $\mu$ m step size.



In the table below there are data of azurite pigment analyzed and data for the calculation of sensitivity and limit of detection.



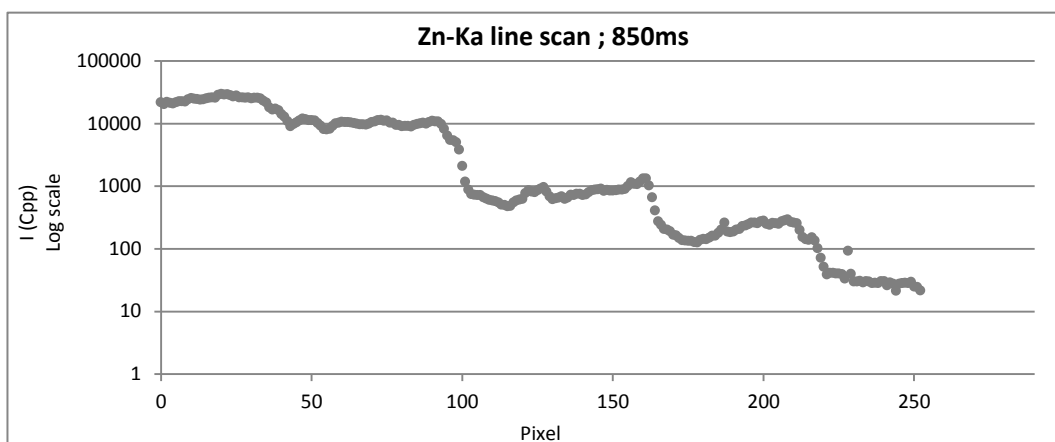
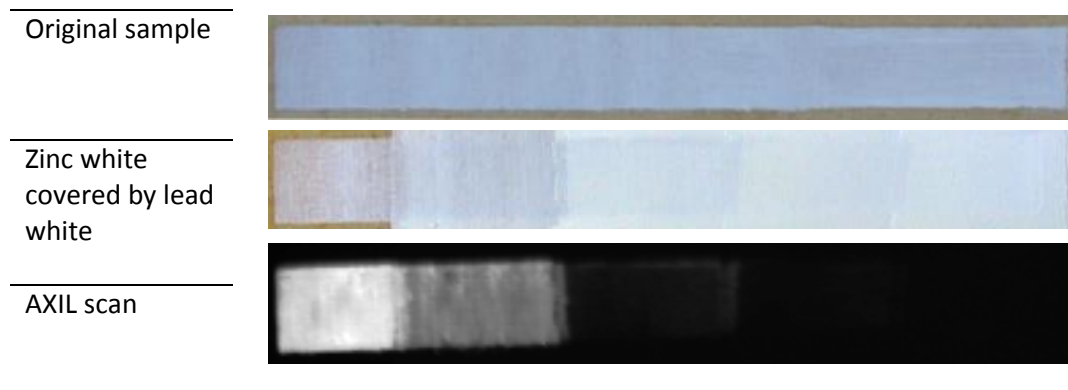
Figure 4.10 Pigment used in the study

<b>Element of interest</b>	Zinc (Zn)	<b>X-Ray excitation energy for Cu-K</b>	K = 1,196 KeV
<b>Pigment provenience</b>	Block	<b>mass attenuation coefficient (<math>\mu_0</math>)</b>	115,20 cm <sup>2</sup> /g
<b>Atomic Number (Z)</b>	30	<b>X-Ray fluorescent energy for Cu-K<math>\alpha</math></b>	K $\alpha$ = 8,638 KeV
<b>Density of lead white</b>	5,11 g/cm <sup>3</sup>	<b>mass attenuation coefficient (<math>\mu_f</math>)</b>	152,9 cm <sup>2</sup> /g
<b>Density of pigment ( <math>\rho</math> )</b>	4,44g/cm <sup>3</sup>	<b>Cos<math>\alpha</math></b>	0,000
<b>Concentration (C<sub>i</sub>)</b>	80,34	<b>Cos<math>\beta</math></b>	0,707
<b>Levels</b>			
	<b>Absorption factor for Pb ( A<sub>1</sub> )</b>	<b>Absorption factor for Cu ( A<sub>2</sub> )</b>	<b>Irradiated mass (mg)</b>
0 level	1,000	0,571	9,28
1 level	0,973	0,626	7,61
2 level	0,945	0,528	10,78
3 level	0,889	0,455	13,75
4 level	0,858	0,521	11,02

Table 4.7. Data for the quantitative analysis of Zn.

Results for:

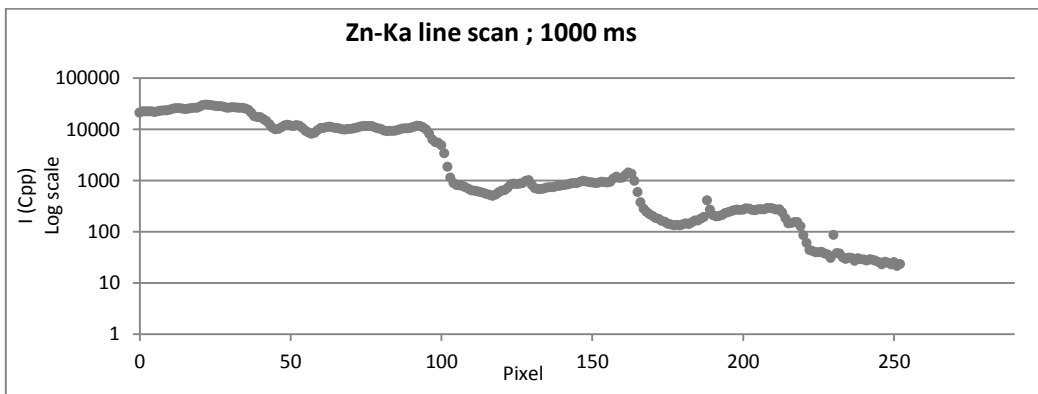
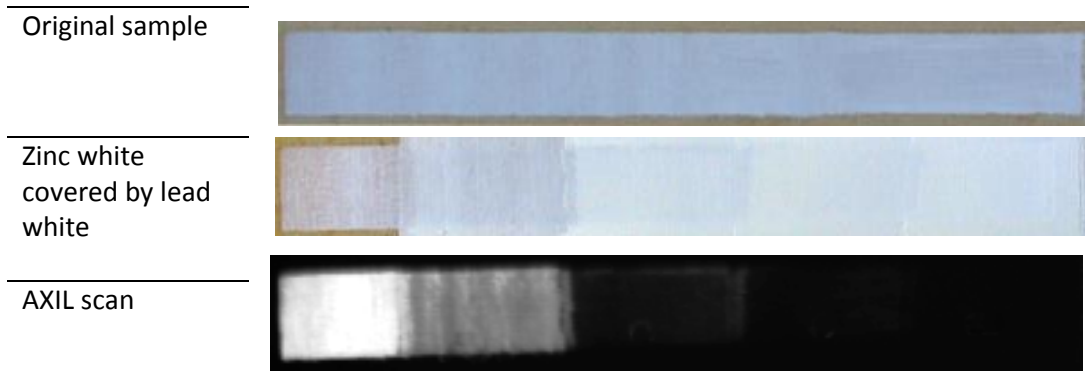
Instrument: AXIL D; Time per Pixel: 850ms ;Step size: 500 $\mu$ m ; Total time: 22 hours and 50minuts





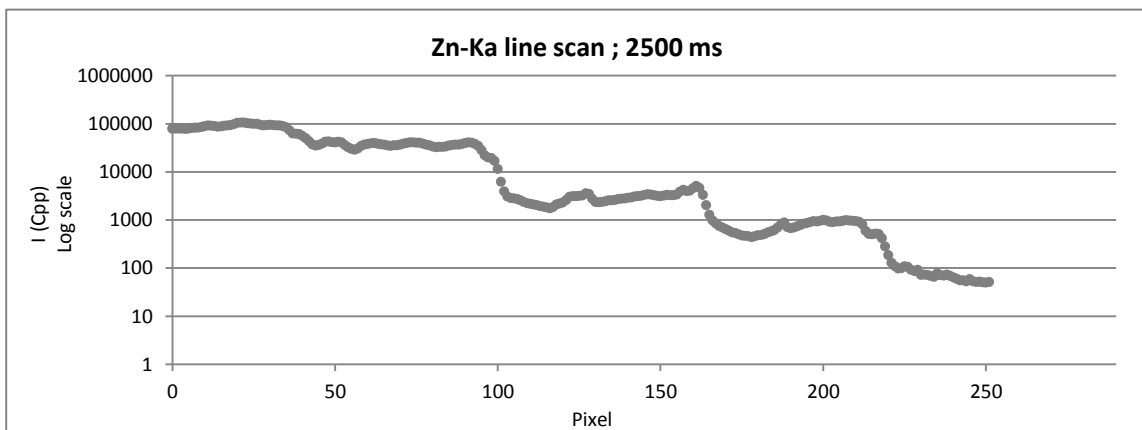
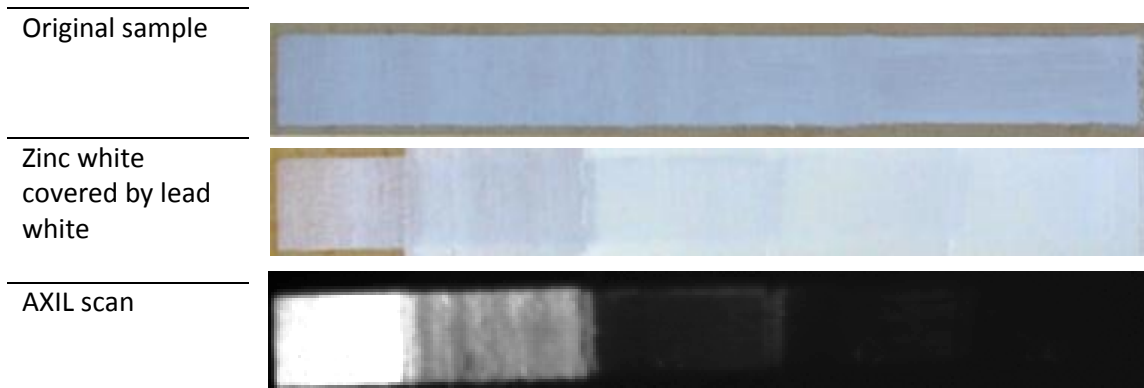
Results for:

Instrument AXIL D Time per Pixel: 1000ms ; Step size: 500 $\mu$ m ; Total time: 26 hours and 52 minutes



Results for:

Instrument AXIL D ; Time per Pixel: 2500ms ; Step size: 500 $\mu$ m ; Total time: 67 hours and 10 minutes



<b>SCAN: 850ms 500µm</b>	<b>Intensity average (cps)</b>	<b>St.Dev.</b>	<b>Sensitivity (cps/mg)</b>	<b>Limit of Detection (µg)</b>
0 level	28187	3411	5319	1924
1 level	11789	1142	2544	1347
2 level	913	232	170	4095
3 level	239	64	43	4472
4 level	36	8	7	3248
<b>SCAN: 1000ms 500µm</b>				
0 level	24974	3437	4712	1846
1 level	10489	1085	2263	1286
2 level	832	221	155	3821
3 level	216	62	39	4228
4 level	31	8	6	3064
<b>SCAN: 2500ms 500µm</b>				
0 level	34478	4315	6506	1990
1 level	14728	1361	3178	1285
2 level	1170	286	218	3941
3 level	293	74	53	4217
4 level	30	8	6	3921

**Table 4.8.** Results for Zn.

All the average intensity and sensitivity decrease with the growth of lead white thickness. For Zn the decrease of the values of sensitivity seems to be much stronger than in the other elements.

Limit of detection always increases with the growth of covering lead white, except for the 1 level, probably because of the high difference in standard deviation between 0 and 1 level, this is due to the irregularity of the layers.

## 4.2.2 Results

### Sample 2: Azurite $\text{Cu}_3(\text{CO}_3)_2(\text{OH})_2$

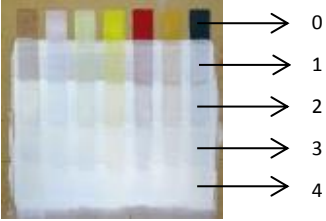





Description	Samples taken from the five levels 
0 level Azurite average thickness: 24,50 $\mu\text{m}$	 4X magnification
1 level Azurite average thickness: 21,46 $\mu\text{m}$ Lead white average thickness: 58,65 $\mu\text{m}$	 4X magnification
2 level Azurite average thickness: 30,85 $\mu\text{m}$ Lead white average thickness: 76,96 $\mu\text{m}$	 4X magnification
3 level Azurite average thickness: 22,66 $\mu\text{m}$ Lead white average thickness: 91,53 $\mu\text{m}$	 4X magnification
4 level Azurite average thickness: 23,61 $\mu\text{m}$ Lead white average thickness: 126,67 $\mu\text{m}$	 4X magnification

Table 4.1 Cross sections of five samples taken from azurite paint layer.

Azurite	0 level	1 level		2 level		3 level		4 level	
	μm Cu	μm Cu	μm Pb	μm Cu	μm Pb	μm Cu	μm Pb	μm Cu	μm Pb
Values taken on the cross sections photos by Dino Capture	23,52	21,01	65,83	28,01	84,03	18,21	92,44	21,54	120,29
	31,32	16,81	49,02	35,01	82,63	18,21	86,83	14,36	134,65
	31,32	19,81	58,82	35,01	81,23	21,06	93,84	21,62	122,08
	27,96	23,81	65,83	25,37	79,83	28,01	81,23	23,34	120,29
	24,61	30,81	56,02		64,43	28,05	84,14	41,29	116,70
	25,75	15,08	58,82		63,78	22,41	93,84	21,54	140,04
	25,73	28,01	56,02		75,68		79,94	21,54	134,65
	22,37	18,21	58,82		84,03		98,04		113,11
	16,78	19,61					113,45		138,24
15,66									
<b>Average Thicknesses:</b>	<b>24,50</b>	<b>21,46</b>	<b>58,65</b>	<b>30,85</b>	<b>76,96</b>	<b>22,66</b>	<b>91,53</b>	<b>23,61</b>	<b>126,67</b>

Table 4.2 Calculation of average thicknesses for azurite and lead white

In the tabel above there are a list of thicknesses taken from the five samples shown in the page before. The layers are more or less homogeneous, except the 2 layer of Azurite, that is 10μm thicker than the others. The lead white layers grow homogeneously from 58,65μm to 126,67μm.

Below an outline of the mockup in section shows the layers thicknesses:

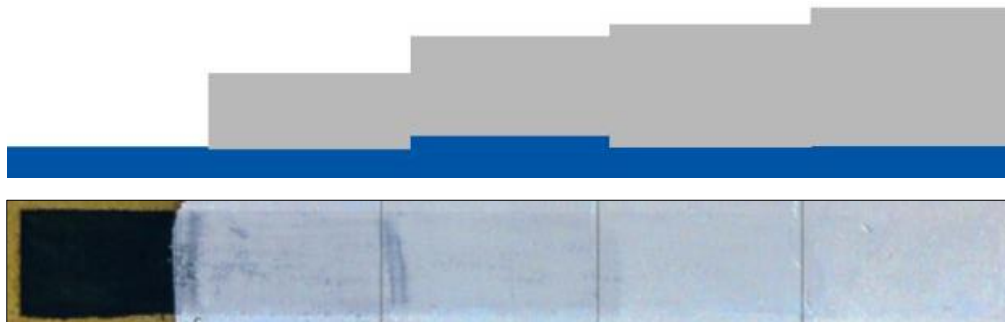


Figure 4.3. Outline of azurite structure

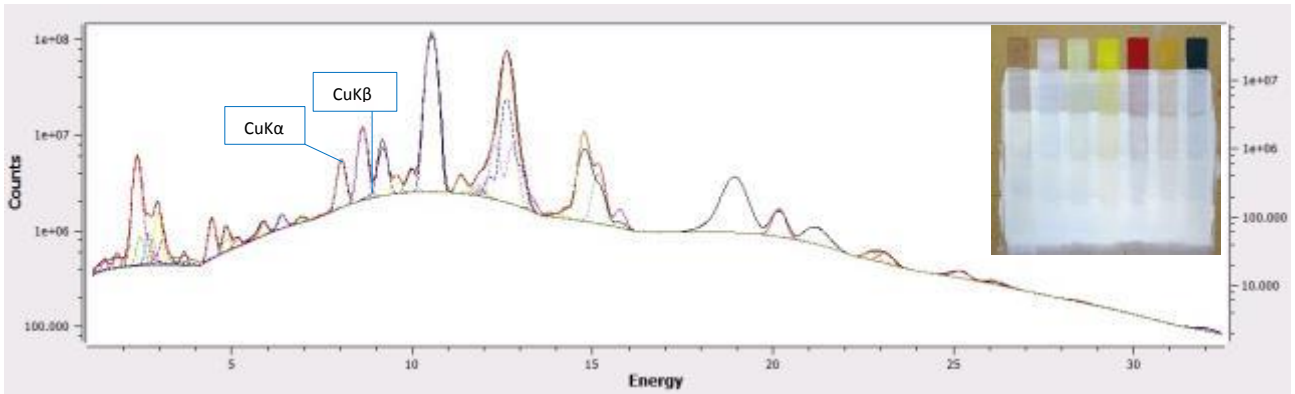


Figure 4.4. Spectra of the second sample. Below the blue lines highlight the Cu-K $\alpha$  and Cu-K $\beta$  peaks.

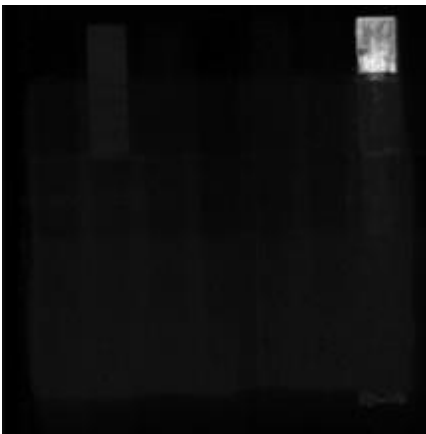


Figure 4.5 a. Cu-K map; 850ms time per pixel and 500 $\mu$ m step size

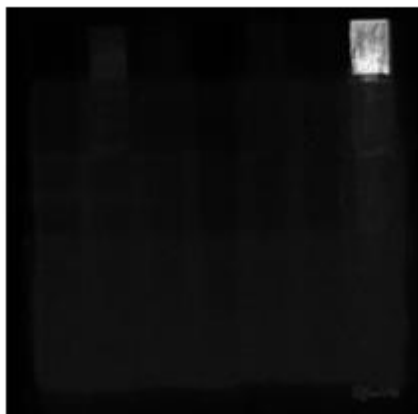
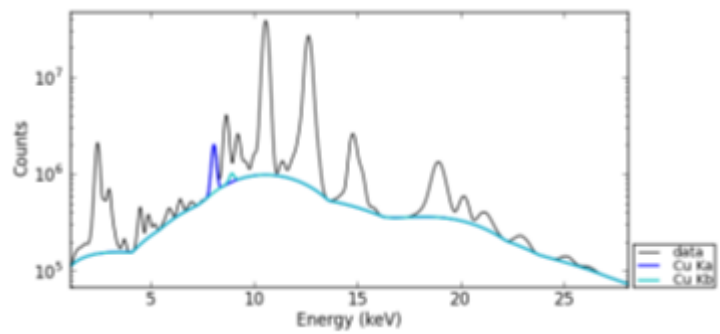


Figure 4.5 b. Cu-K map; 1000ms time per pixel and 500 $\mu$ m step size.

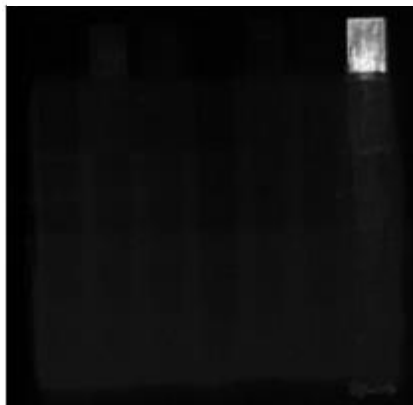
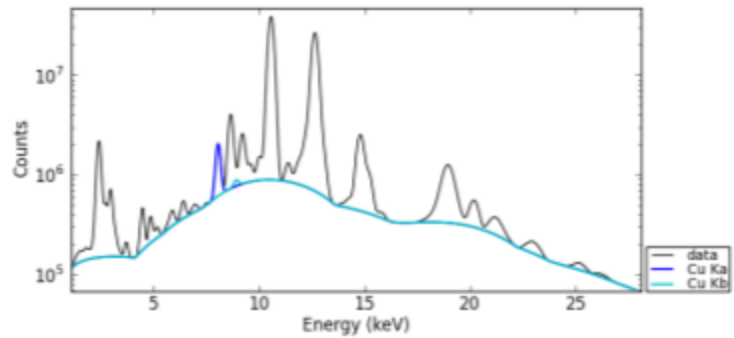
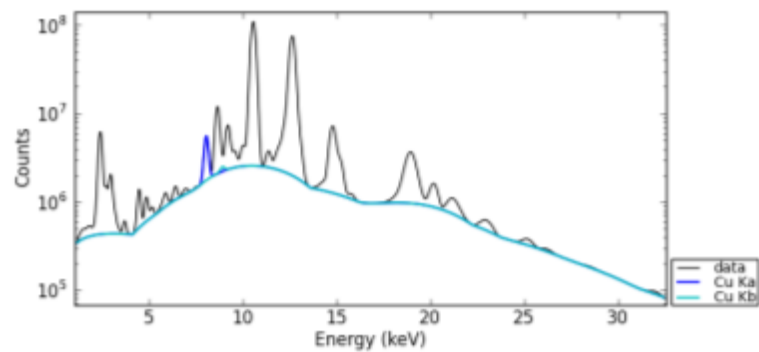


Figure 4.5 c. Cu-K map; 2500ms time per pixel and 500 $\mu$ m step size.



In the table below there are data of azurite pigment analyzed and data for the calculation of sensitivity and limit of detection.

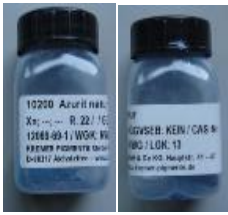


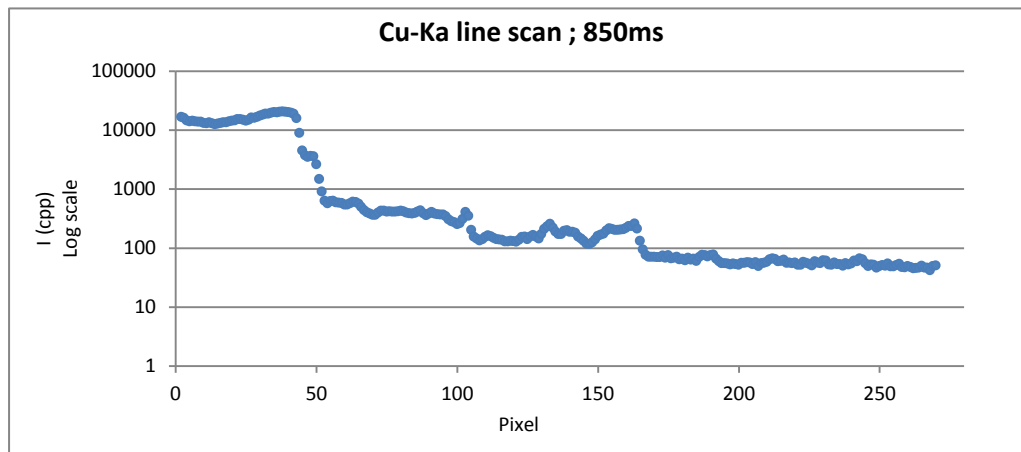
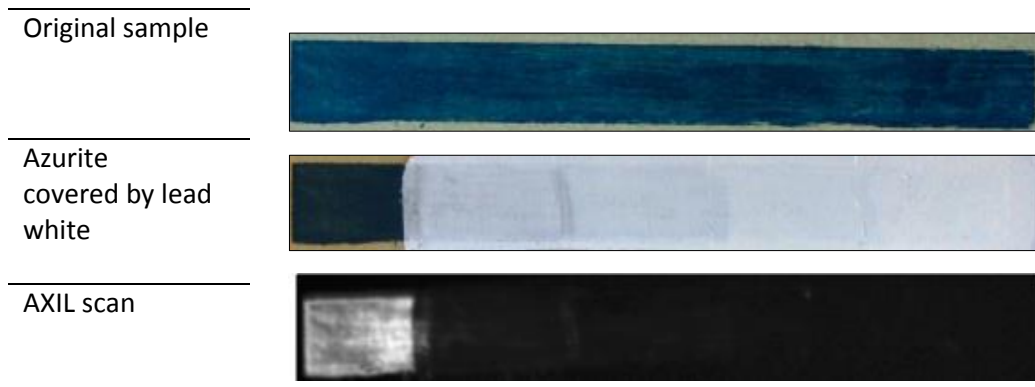
Figure 4.6. Pigment used in the study

<b>Element of interest</b>	Copper (Cu)	<b>X-Ray excitation energy for Cu-K</b>	K = 8,979 KeV
<b>Pigment provenience</b>	Kremer	<b>mass attenuation coefficient (<math>\mu_0</math>)</b>	138,5 cm <sup>2</sup> /g
<b>Atomic Number (Z)</b>	29	<b>X-Ray fluorescent energy for Cu-K<math>\alpha</math></b>	K $\alpha$ = 8,047 KeV
<b>Density of lead white (<math>\rho</math>)</b>	5,11 g/cm <sup>2</sup>	<b>mass attenuation coefficient (<math>\mu_f</math>)</b>	182,4 cm <sup>2</sup> /g
<b>Density of pigment (<math>\rho</math>)</b>	3,11 g/cm <sup>2</sup>	<b>Cos<math>\alpha</math></b>	0,000
<b>Concentration (C<sub>i</sub>)</b>	55,31	<b>Cos<math>\beta</math></b>	0,707
<b>Levels</b>	<b>Absorption factor for Pb (A<sub>1</sub>)</b>	<b>Absorption factor for Cu (A<sub>2</sub>)</b>	<b>Irradiated mass (mg)</b>
0 level	1,000	0,637	4,21
1 level	0,920	0,671	3,69
2 level	0,897	0,574	5,30
3 level	0,879	0,657	3,89
4 level	0,836	0,647	4,05

Table 4.3. Data for the quantitative analysis of Cu.

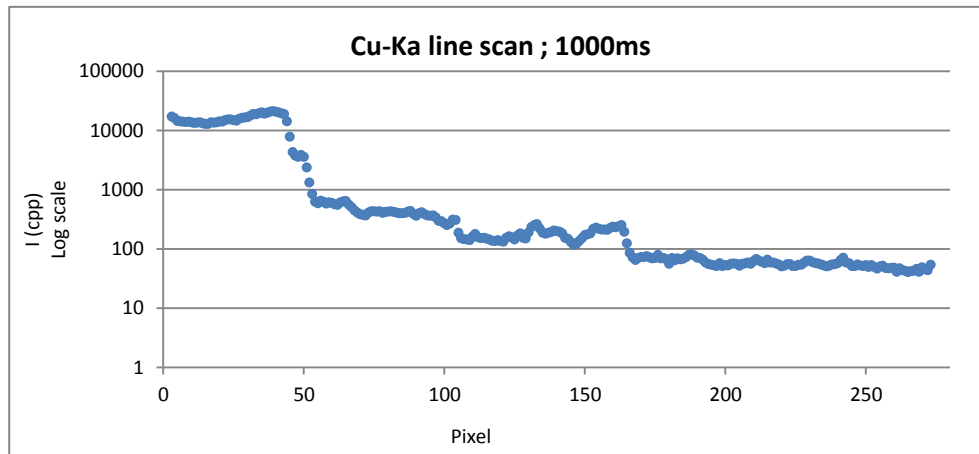
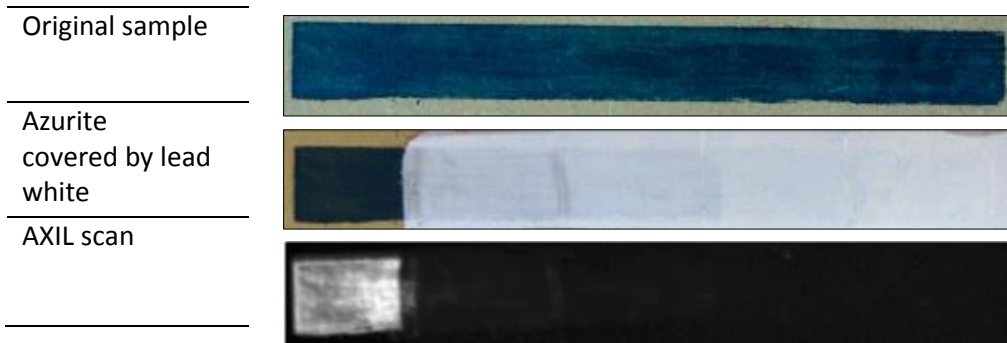
Results for:

Instrument AXIL D; Time per Pixel: 850ms ; Step size: 500 $\mu$ m; Total time: 22 hours and 50minuts



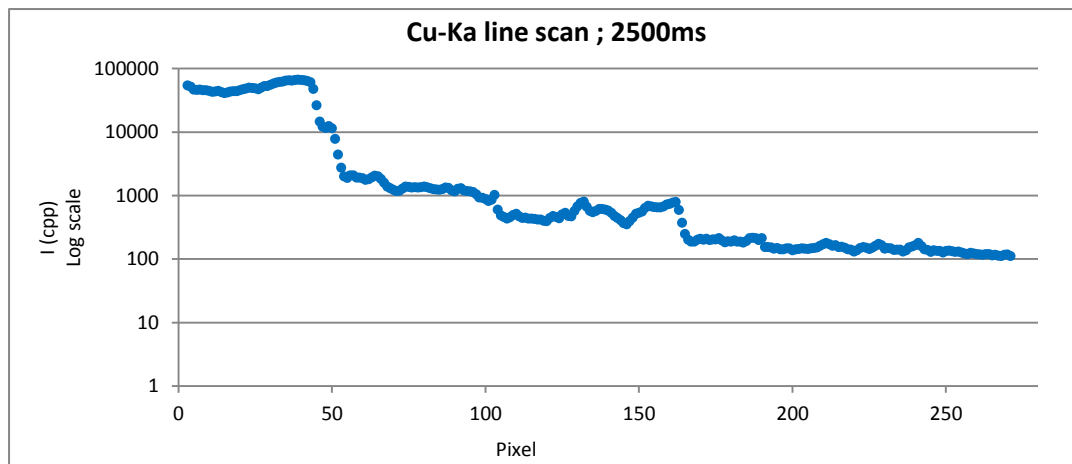
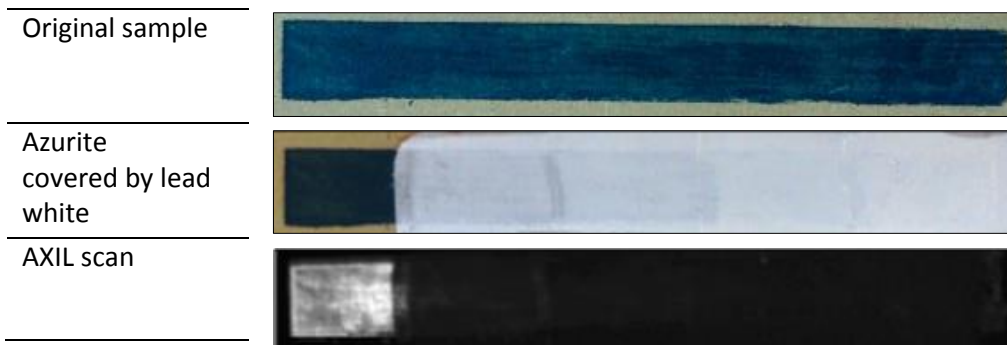
Results for:

instrument: AXIL D; Time per Pixel: 1000ms; Step size: 500 $\mu$ m; Total time: 26 hours and 52 minutes



Results for:

Instrument: AXIL; Time per Pixel: 2500ms; Step size: 500 $\mu$ m; Total time: 67 hours and 10 minutes



<b>SCAN: 850ms 500µm</b>	<b>Intensity average (cps)</b>	<b>St.Dev.</b>	<b>Sensitivity (cpp/mg)</b>	<b>Limit of Detection (µg)</b>
0 level	18676	3044,13	6966	1311
1 level	507	117,39	223	1581
2 level	200	43,33	73	1776
3 level	74	9,14	33	829
4 level	61	6,09	28	662
<b>SCAN: 1000ms 500µm</b>				
0 level	15819	2864,52	5901	1456
1 level	438	105,10	192	1638
2 level	176	38,61	64	1797
3 level	62	8,09	28	875
4 level	55	6,91	25	821
<b>SCAN: 2500ms 500µm</b>				
0 level	20695	3402,86	7719	1322
1 level	586	127,20	258	1482
2 level	214	47,08	78	1801
3 level	69	10,39	31	1015
4 level	52	6,15	24	776

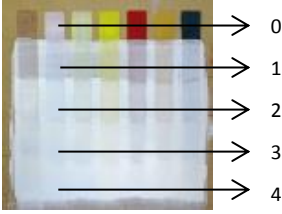





**Table 4.4.** Results for Cu

Intensity and sensitivity decrease considerably with the growth of lead white thicknesses. The highest values of sensitivities are of course in the 0 level, between 6000cps/mg and 7700cps/mg. The sensitivity is very low for the 2, 3 and 4 levels, these values correspond perfectly to what is observed in elemental maps, where only 0 and 1 levels are visible.

Limit of detection increases with the growth of the lead white thickness up to the 2 level). Effectively it is necessary more pigment under a thick covering layer to let copper detected.



**Sample 2: Zinc White ZnO**

Description	Sample taken from the five levels 
0 level Zinc white average thickness: 26,04 $\mu\text{m}$	 Magnification: 4X
1 level Zinc white average thickness: 21,36 $\mu\text{m}$ Lead white average thickness: 19,47 $\mu\text{m}$	 Magnification: 5X
2 level Zinc white average thickness: 30,24 $\mu\text{m}$ Lead white average thickness: 40,32 $\mu\text{m}$	 Magnification: 4X
3 level Zinc white average thickness: 38,57 $\mu\text{m}$ Lead white average thickness: 83,33 $\mu\text{m}$	 Magnification: 4X
4 level Zinc white average thickness: 30,82 $\mu\text{m}$ Lead white average thickness: 108,74 $\mu\text{m}$	 Magnification: 5X

**Table 4.5.** Cross sections of the five samples taken from zinc white paint layer.

Zinc White	0 level	1 level		2 level		3 level		4 level	
	µm Zn	µm Pb	µm Zn	µm Pb	µm Zn	µm Pb	µm Zn	µm Pb	µm Zn
Values taken on the cross sections photos by Dino Capture	22,40	21,01	23,81	44,79	22,40	69,00	35,91	120,29	30,52
	22,40	18,21	21,01	40,38	29,12	100,60	39,50	113,11	25,13
	42,55	14,01	19,61	42,55	40,31	57,45	32,32	89,84	28,73
	17,92	21,01	21,01	40,31	26,88	122,08	45,03	111,31	30,52
	26,88	21,42		33,59	35,83	78,99	44,88	100,54	19,75
	33,59	19,61		40,31	26,88	71,84	36,31	96,95	26,93
	17,92	21,01			33,59		36,09	107,72	39,50
	24,64				26,88			95,22	46,68
<b>Average Thicknesses:</b>	<b>26,04</b>	<b>19,47</b>	<b>21,36</b>	<b>40,32</b>	<b>30,24</b>	<b>83,33</b>	<b>38,57</b>	<b>108,74</b>	<b>30,92</b>

Table 4.6 Calculation of average thicknesses for zinc white and lead white

Looking at the table above, layers are more or less homogeneous, except the 1 layer (21,36 µm) and the 3 layer (38,57 10µm) of zinc white. The lead white layers grow homogeneously from 19,47µm to 108,74 µm.

Below there is an outline of the mockup in section:



Figure 4.7. Outline of Zinc white structure

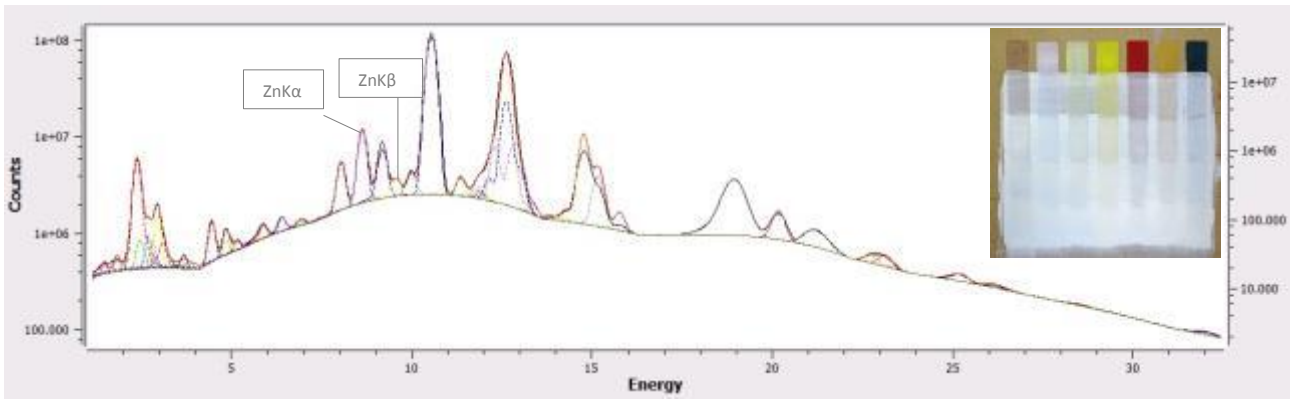


Figure 4.8 Spectra of the second sample. Below the black and gray lines highlight the ZnK $\alpha$  and ZnK $\beta$  peaks.

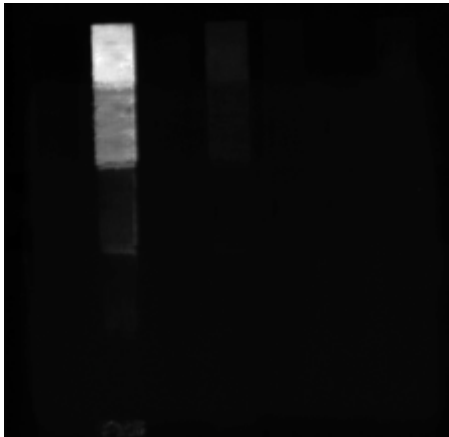


Figure 4.9 a. Zn-K map; 850ms time per pixel and 500 $\mu$ m step size.

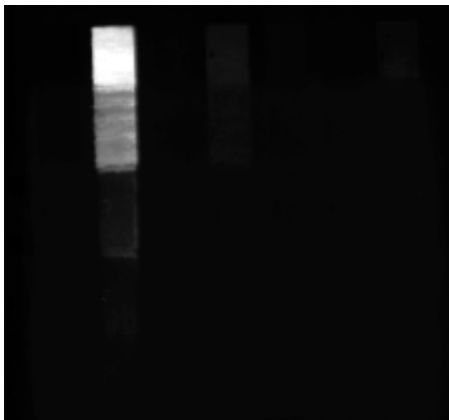
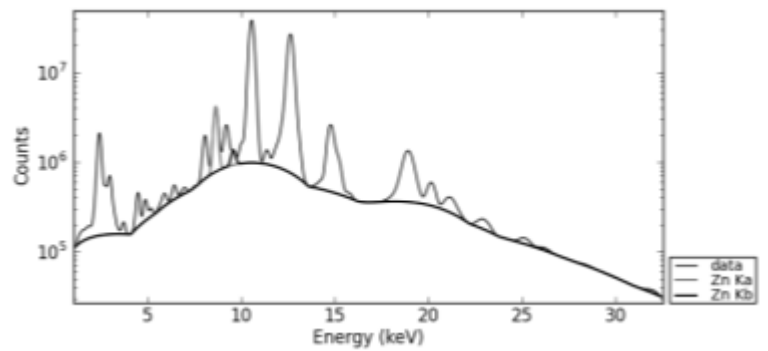


Figure 4.9 b. Zn-K map; 1000ms time per pixel and 500 $\mu$ m step size.

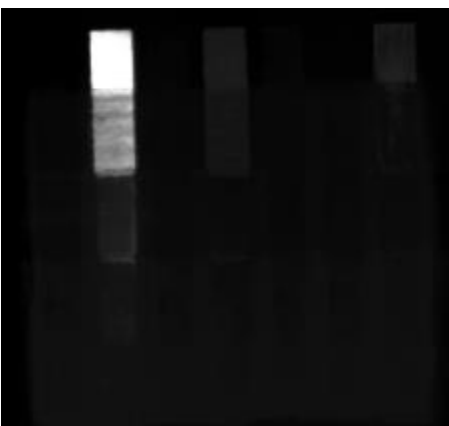
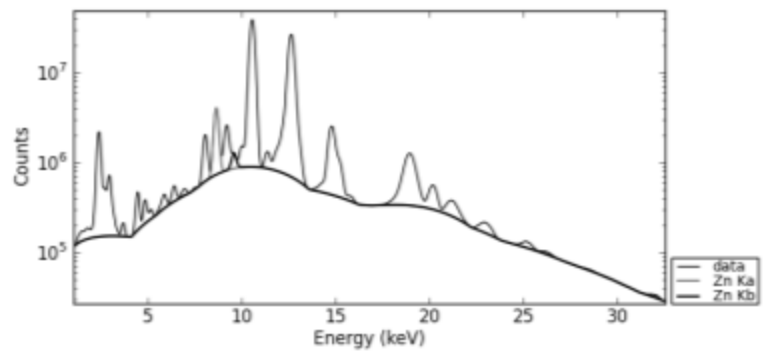
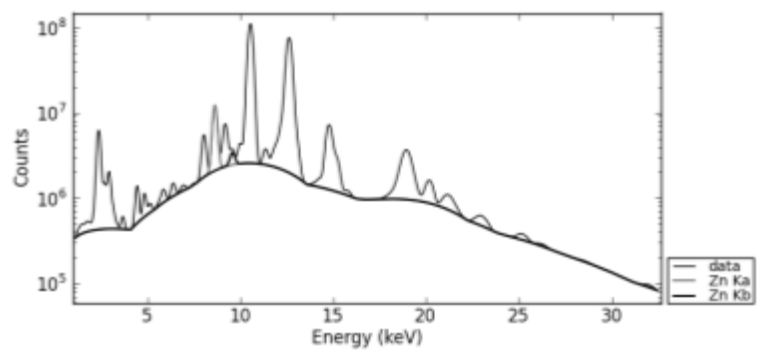


Figure 4.9 c. Zn-K map; 2500ms time per pixel and 500 $\mu$ m step size.



In the table below there are data of azurite pigment analyzed and data for the calculation of sensitivity and limit of detection.



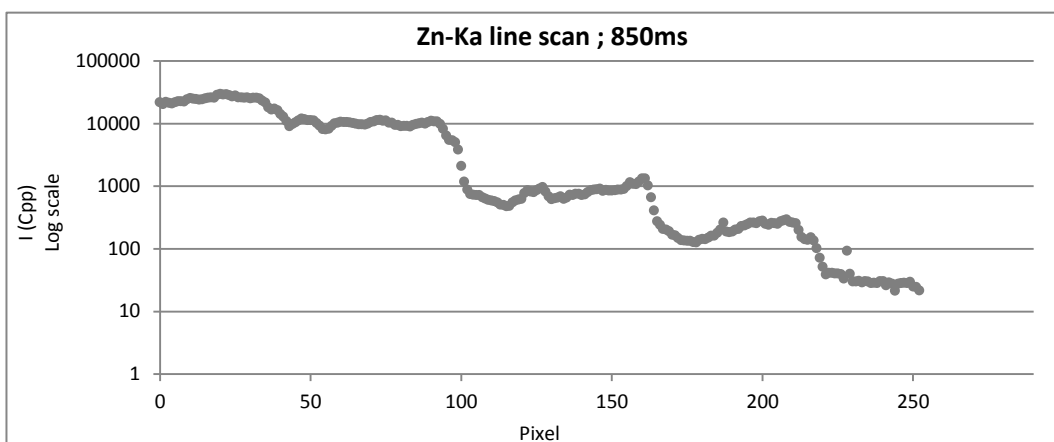
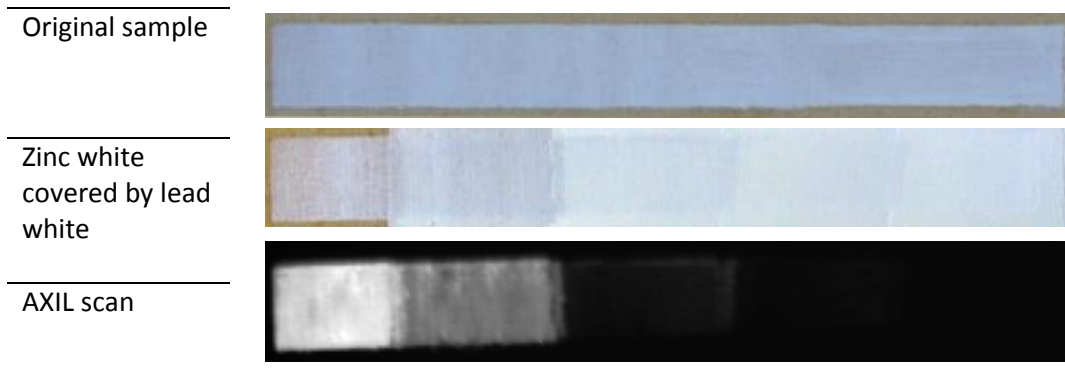
Figure 4.10 Pigment used in the study

<b>Element of interest</b>	Zinc (Zn)	<b>X-Ray excitation energy for Cu-K</b>	K = 1,196 KeV
<b>Pigment provenience</b>	Block	<b>mass attenuation coefficient (<math>\mu_0</math>)</b>	115,20 cm <sup>2</sup> /g
<b>Atomic Number (Z)</b>	30	<b>X-Ray fluorescent energy for Cu-K<math>\alpha</math></b>	K $\alpha$ = 8,638 KeV
<b>Density of lead white</b>	5,11 g/cm <sup>3</sup>	<b>mass attenuation coefficient (<math>\mu_f</math>)</b>	152,9 cm <sup>2</sup> /g
<b>Density of pigment ( <math>\rho</math> )</b>	4,44g/cm <sup>3</sup>	<b>Cos<math>\alpha</math></b>	0,000
<b>Concentration (C<sub>i</sub>)</b>	80,34	<b>Cos<math>\beta</math></b>	0,707
<b>Levels</b>			
	<b>Absorption factor for Pb ( A<sub>1</sub> )</b>	<b>Absorption factor for Cu ( A<sub>2</sub> )</b>	<b>Irradiated mass (mg)</b>
0 level	1,000	0,571	9,28
1 level	0,973	0,626	7,61
2 level	0,945	0,528	10,78
3 level	0,889	0,455	13,75
4 level	0,858	0,521	11,02

Table 4.7. Data for the quantitative analysis of Zn.

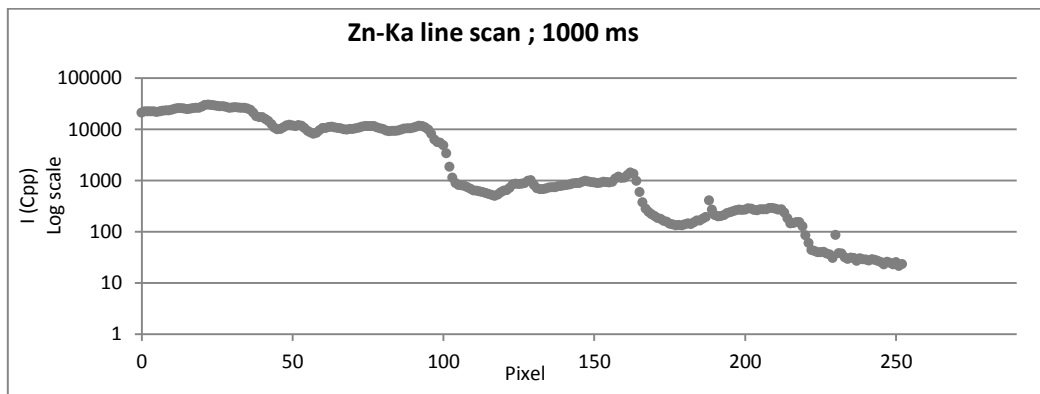
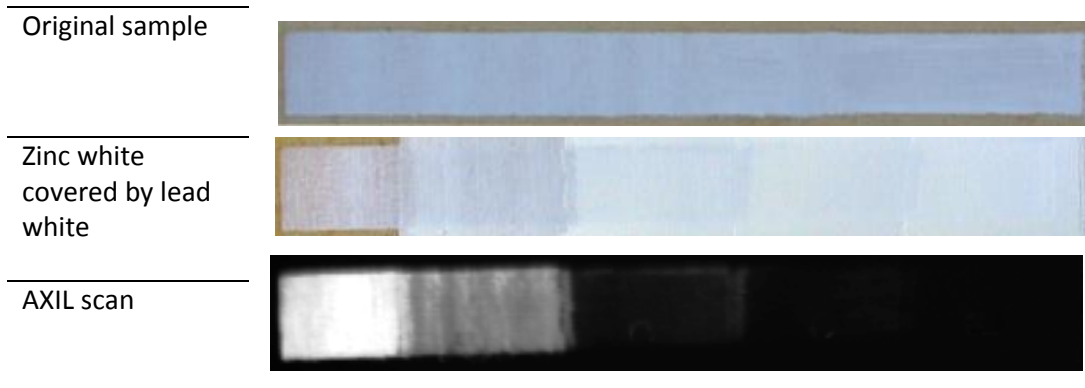
Results for:

Instrument: AXIL D; Time per Pixel: 850ms ;Step size: 500 $\mu$ m ; Total time: 22 hours and 50minuts



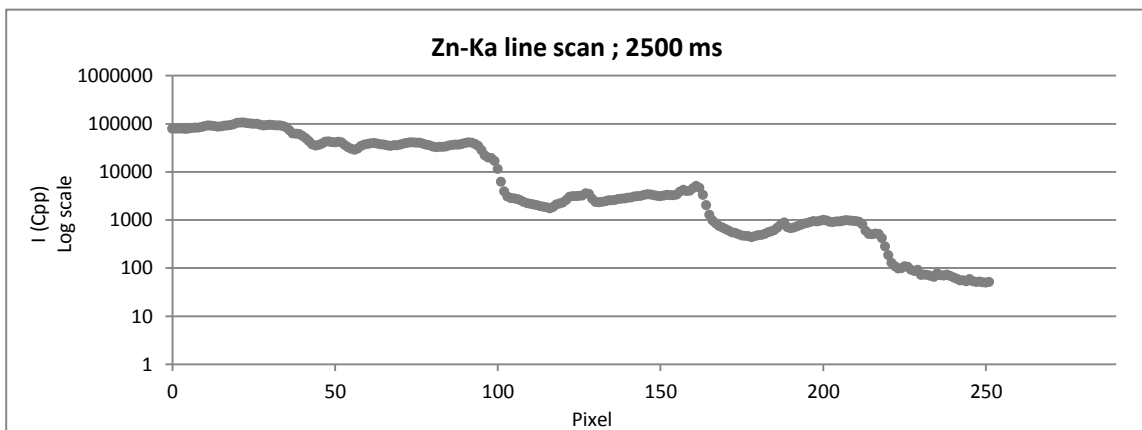
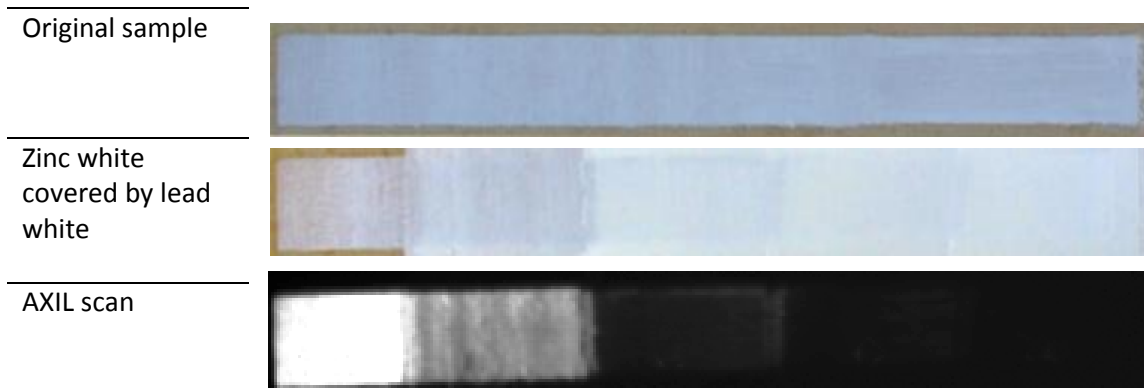
Results for:

Instrument AXIL D Time per Pixel: 1000ms ; Step size: 500 $\mu$ m ; Total time: 26 hours and 52 minutes



Results for:

Instrument AXIL D ; Time per Pixel: 2500ms ; Step size: 500 $\mu$ m ; Total time: 67 hours and 10 minutes



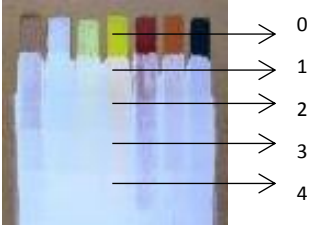
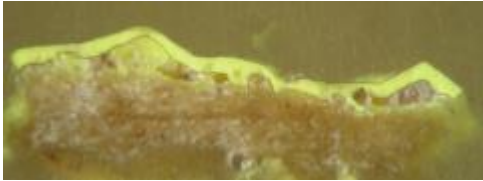



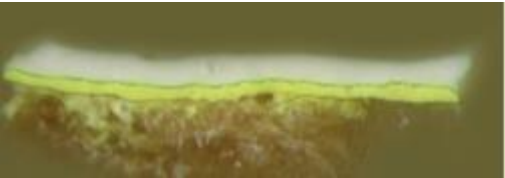
<b>SCAN: 850ms 500µm</b>	<b>Intensity average (cps)</b>	<b>St.Dev.</b>	<b>Sensitivity (cps/mg)</b>	<b>Limit of Detection (µg)</b>
0 level	28187	3411	5319	1924
1 level	11789	1142	2544	1347
2 level	913	232	170	4095
3 level	239	64	43	4472
4 level	36	8	7	3248
<b>SCAN: 1000ms 500µm</b>				
0 level	24974	3437	4712	1846
1 level	10489	1085	2263	1286
2 level	832	221	155	3821
3 level	216	62	39	4228
4 level	31	8	6	3064
<b>SCAN: 2500ms 500µm</b>				
0 level	34478	4315	6506	1990
1 level	14728	1361	3178	1285
2 level	1170	286	218	3941
3 level	293	74	53	4217
4 level	30	8	6	3921

**Table 4.8.** Results for Zn.

All the average intensity and sensitivity decrease with the growth of lead white thickness. For Zn the decrease of the values of sensitivity seems to be much stronger than in the other elements.

Limit of detection always increases with the growth of covering lead white, except for the 1 level, probably because of the high difference in standard deviation between 0 and 1 level, this is due to the irregularity of the layers.

**Sample 1: Cadmium yellow CdS**

Description	Sample taken from the five levels 
0 level Cadmium sulfide average thickness: 56,90µm	 Magnification: 6,3X
1 level Cadmium sulfide average thickness: 67,34 µm Lead white average thickness: 50,45 µm	 Magnification: 6,3X
2 level Cadmium sulfide average thickness: 67,12µm Lead white average thickness: 34,53µm	 Magnification: 8X
3 level Cadmium sulfide average thickness: 58,43µm Lead white average thickness: 49,96µm	 Magnification: 6,3X
4 level Cadmium sulfide average thickness: 62,49µm Lead white average thickness: 71,91µm	 Magnification: 8X

**Table 4.9.** Cross sections of the five samples taken from cadmium yellow paint layer.

Cadmium Yellow	0 level	1 level		3 level		4 level		5 level	
	$\mu\text{m Cd}$	$\mu\text{m Pb}$	$\mu\text{m Cd}$	$\mu\text{m Pb}$	$\mu\text{m Cd}$	$\mu\text{m Pb}$	$\mu\text{m Cd}$	$\mu\text{m Pb}$	$\mu\text{m Cd}$
Values taken on the cross section photos by Dino Capture	62,79	57,66	57,66	34,23	64,86	63,03	98,04	57,05	134,23
	53,82	68,47	81,08	31,53	54,05	60,24	74,23	62,64	88,37
	53,82	40,54	55,86	31,53	76,58	50,42	61,69	83,89	63,76
	53,82	45,95	74,77	35,14	72,97	50,42	28,01	91,72	40,27
	53,82	39,64		36,04		42,02	42,02	83,89	36,98
	53,82			38,74		33,61	35,02	73,83	36,91
	66,38						70,03	50,34	36,91
<b>Average Thicknesses:</b>	<b>56,90</b>	<b>50,45</b>	<b>67,34</b>	<b>34,53</b>	<b>67,12</b>	<b>49,96</b>	<b>58,43</b>	<b>71,91</b>	<b>62,49</b>

Table 4.10. Calculation of average thicknesses for Cadmium Yellow and lead white

Looking at the table above, we can notice that most of the layers are inhomogeneous because of their very low thicknesses and because the film applicator is a mechanical instrument, the right operation depends on the operator pressure. In particular the lead white thickness in the 2 and 3 levels are lower than the layers before. Although the collected samples represent statistically the morphology of the paint layers, they give a notion of the irregularity of the thicknesses.

Below there is an outline of the mockup in section:

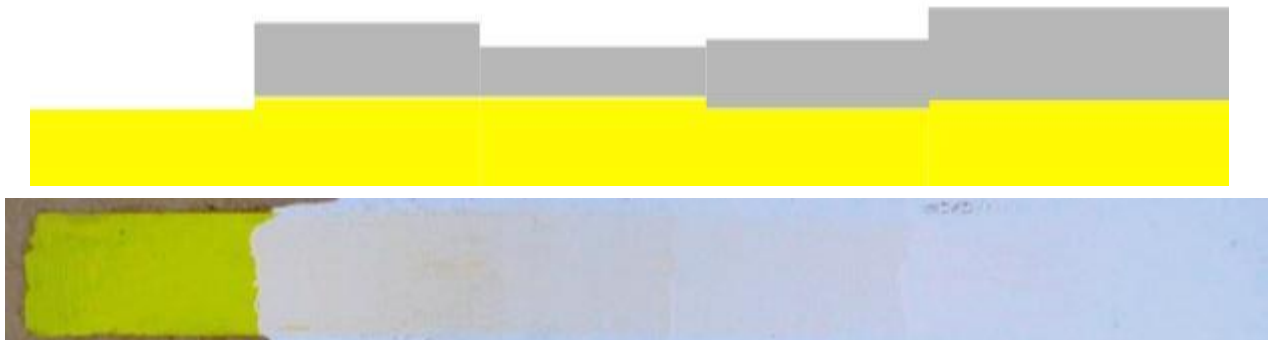


Figure 4.11. Outline of Cadmium yellow structure



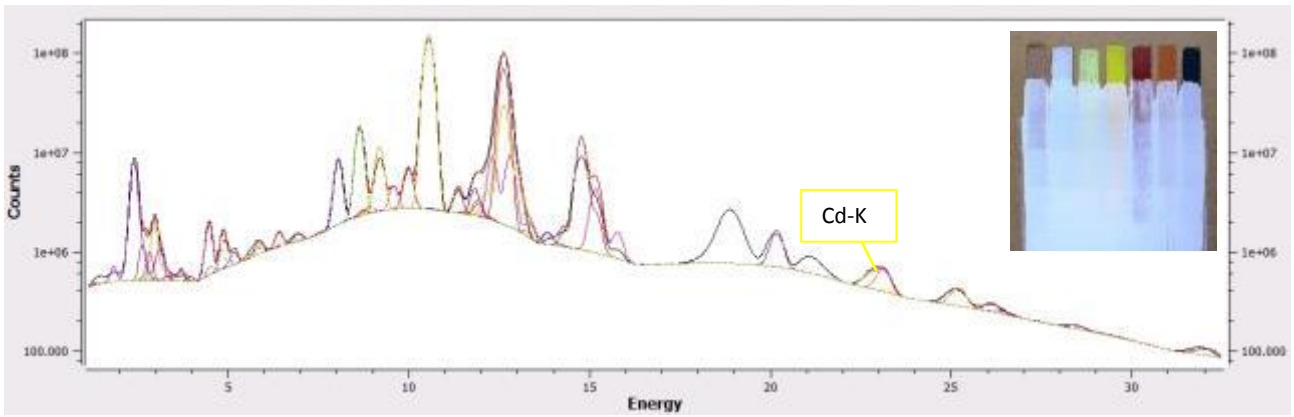


Figure 4.12. Spectra of the first sample. Below the yellow line highlights the Cd-K peak.

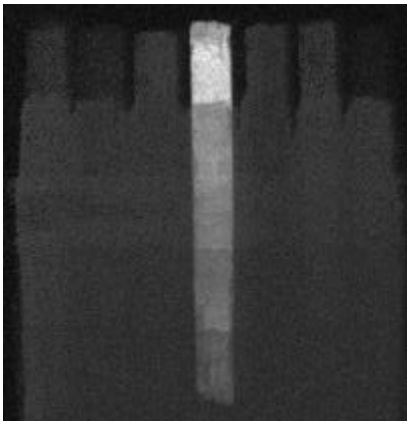


Figure 4.13a. Cd-K map; 850ms time per pixel and 500 $\mu$ m step size.

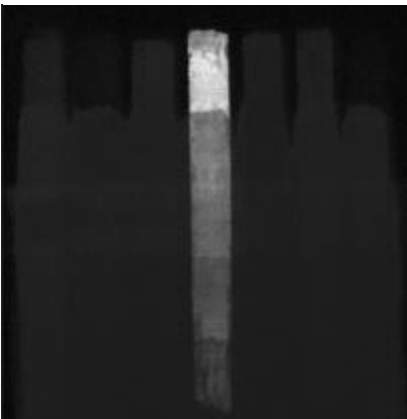
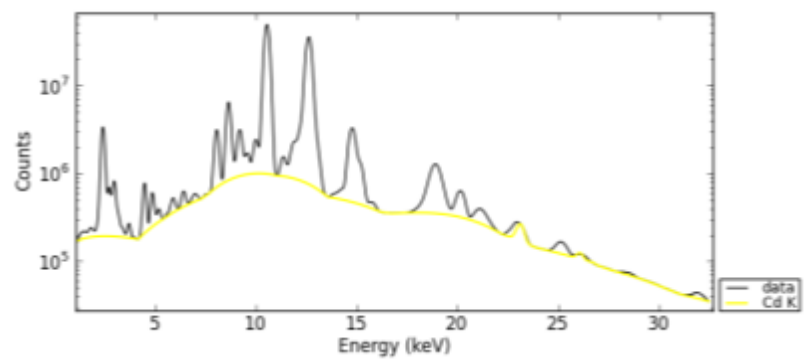


Figure 4.13b. Cd-K map; 1000ms time per pixel and 500 $\mu$ m step size.

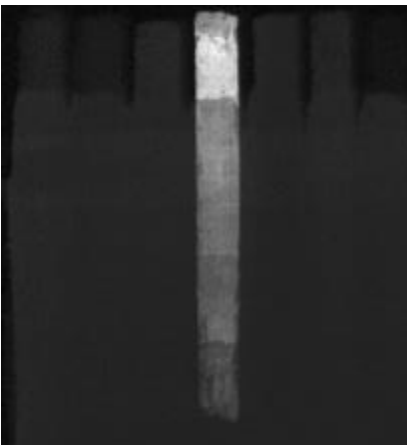
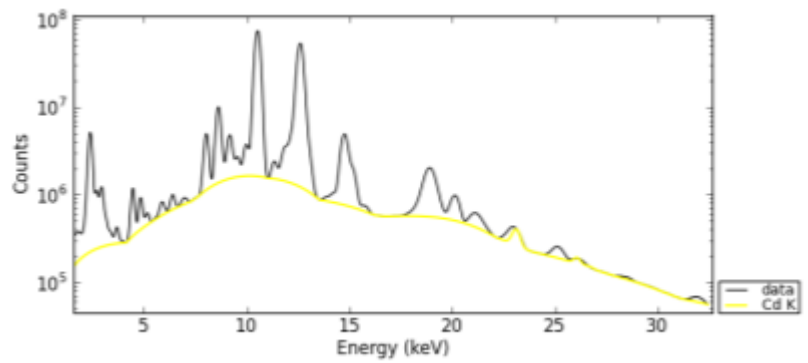
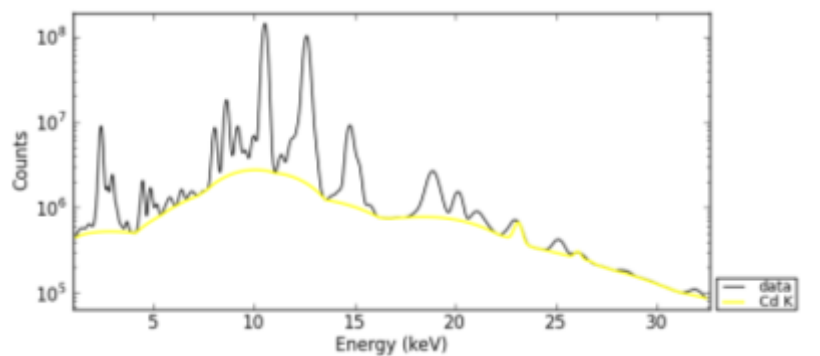


Figure 4.13c. Cd-K map; 2500ms time per pixel and 500 $\mu$ m step size.



In the table below there are data of azurite pigment analyzed and data for the calculation of sensitivity and limit of detection.



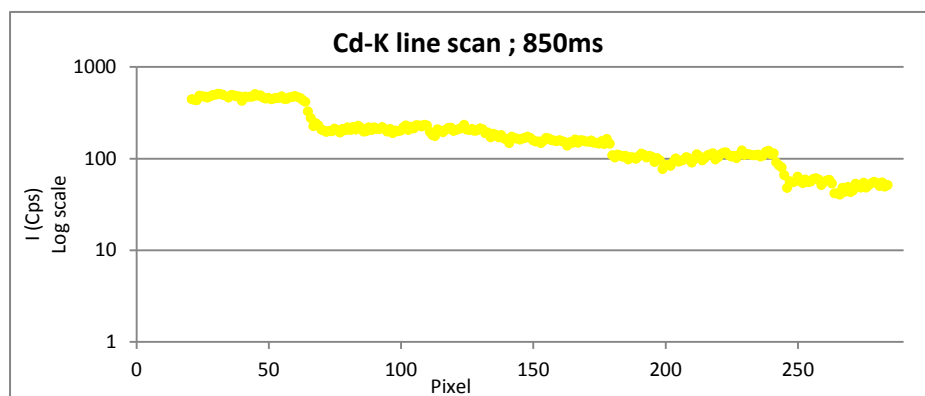
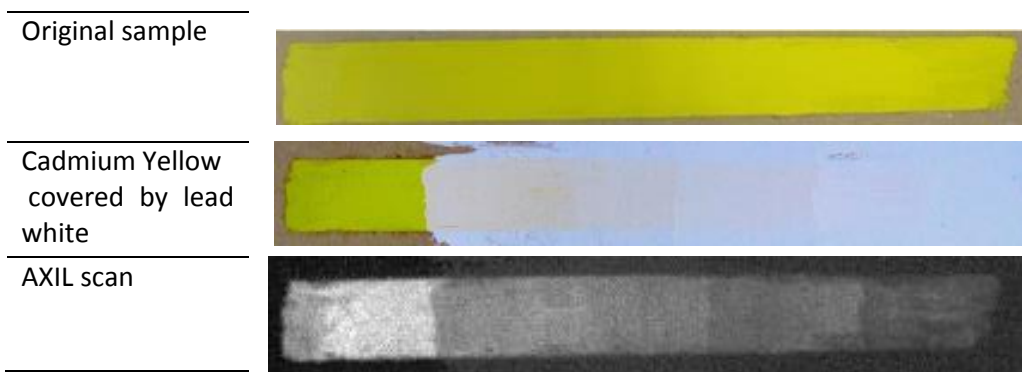
Figure 4.14. Pigment used in the study.

Element of interest	Cadmium (Cd)	X-Ray excitation energy for Cd-K	K = 26,711 keV
Pigment provenience	BLOCK	mass attenuation coefficient ( $\mu_0$ )	3,28 cm <sup>2</sup> /g
Atomic Number (Z)	48	X-Ray fluorescent energy for Cd-K $\alpha$	K $\alpha$ = 23,172 keV
Density of lead white ( $\rho$ )	5,11 g/cm <sup>2</sup>	mass attenuation coefficient ( $\mu_f$ )	4,17 cm <sup>2</sup> /g
Density of pigment ( $\rho$ )	3,85 g/cm <sup>3</sup>	Cos $\alpha$	0,000
Concentration (C <sub>i</sub> )	77,81	Cos $\beta$	0,707
Levels	Absorption factor for Pb (A <sub>1</sub> )	Absorption factor for Cd (A <sub>2</sub> )	Irradiated mass (mg)
0	1,000	0,968	17,05
1	0,931	0,963	20,18
2	0,952	0,963	20,12
3	0,932	0,968	17,51
4	0,903	0,965	18,73

Table 4.11. Data for the quantitative analysis of Cd.

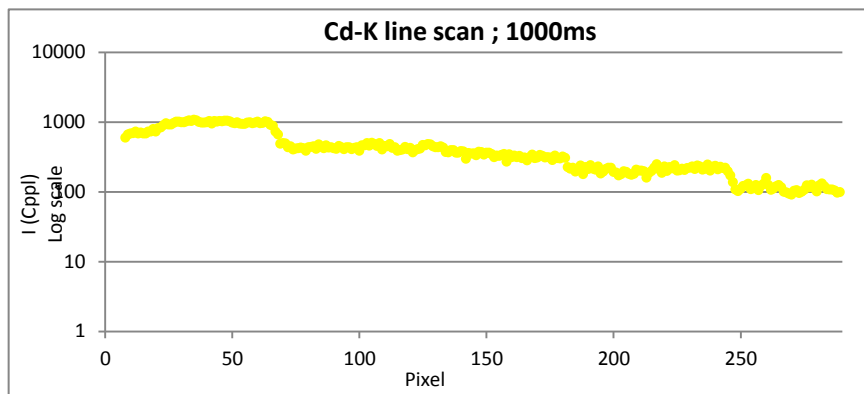
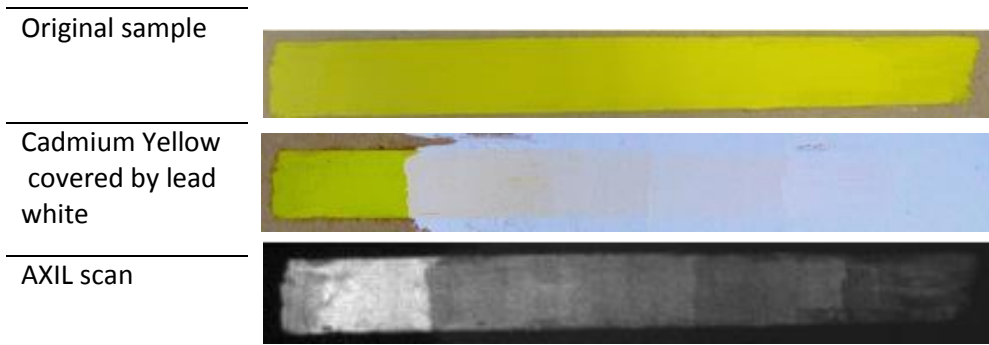
Results for:

Instrument: AXIL; Time per Pixel: 850ms; Step size: 500 $\mu$ m; Total time: 23 hours and 16 minutes



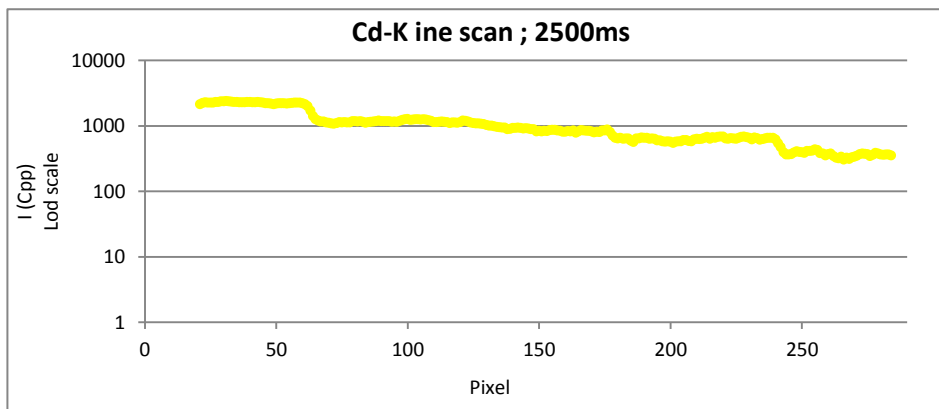
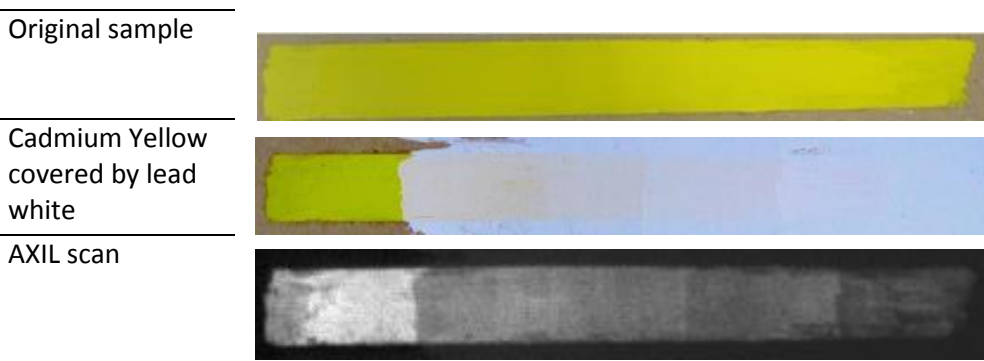
Results for:

Instrument: AXIL; Time per Pixel: 1000ms; Step size: 500 $\mu$ m; Total time: 31 hours and 6 minutes



Results for:

Instrument: AXIL; Time per Pixel: 2500ms; Step size: 500 $\mu$ m; Total time: 71 hours and 16 minutes



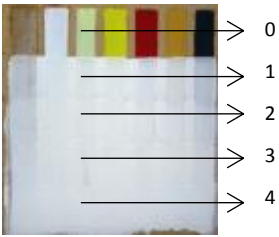




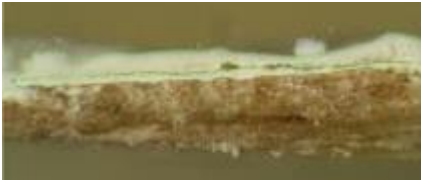
<b>SCAN: 850ms 500µm</b>	<b>Intensity average (cps)</b>	<b>St.Dev.</b>	<b>Sensitivity (cps/mg)</b>	<b>Limit of Detection (µg)</b>
0 level	548	20,138	33	2140
1 level	243	12,374	13	3253
2 level	183	8,166	10	2907
3 level	120	8,987	8	4175
4 level	61	5,601	4	5285
<b>SCAN: 1000ms 500µm</b>				
0 level	984	40,632	60	2046
1 level	431	30,224	24	3806
2 level	326	24,497	18	4155
3 level	208	19,643	13	4468
4 level	113	13,238	7	5722
<b>SCAN: 2500ms 500µm</b>				
0 level	906	19,61	55	1073
1 level	466	10,45	26	1217
2 level	342	17,76	19	2877
3 level	252	10,40	16	1952
4 level	147	7,77	9	2589

**Table 4.12.** Results for Cd.

Intensity and sensitivity always decrease with the growth of lead white thicknesses, while limit of detection always increases with the growth of lead white thicknesses.

Probably the values of cadmium yellow are overestimated, because its peak is influenced by the pile-up artefacts of Pb in lead white. In fact the energy fluorescence of cadmium yellow (Cd-K $\alpha$  : 23,17 KeV ) is exactly the sum of the two energies come from lead white (Pb $_{\alpha 1}$  : 10,55 KeV ; Pb $_{\beta 1}$  : 12,61 KeV).

**Sample 3: lead tin yellow  $Pb_2SnO_4$**

Description	Sample taken from the five levels 
0 level Lead tin yellow average thickness: 37 $\mu\text{m}$	 Magnification: 4X
1 level Lead tin yellow average thickness: 38 $\mu\text{m}$ Lead white average thickness: 69 $\mu\text{m}$	 Magnification: 4X
2 level Lead tin yellow average thickness: 32 $\mu\text{m}$ Lead white average thickness: 117 $\mu\text{m}$	 Magnification: 5X
3 level Lead tin yellow average thickness: 47 $\mu\text{m}$ Lead white average thickness: 127 $\mu\text{m}$	 Magnification: 4 X
4 level Lead tin yellow average thickness: 48 $\mu\text{m}$ Lead white average thickness: 156 $\mu\text{m}$	 Magnification: 4 X

**Table 4.13.** Cross sections of the five samples taken from lead tin yellow paint layer.

Lead tin yellow	0 level	1 level		2 level		3 level		4 level	
	$\mu\text{m Sn}$	$\mu\text{m Pb}$	$\mu\text{m Sn}$	$\mu\text{m Pb}$	$\mu\text{m Sn}$	$\mu\text{m Pb}$	$\mu\text{m Sn}$	$\mu\text{m Pb}$	$\mu\text{m Sn}$
Values taken on the cross sections photos by Dino Capture	36	64	30	127	40	108	49	134	38
	34	66	34	128	23	134	43	162	55
	45	74	43	110	32	125	49	172	45
	29	72	43	110	32	140		157	47
	38			108	34				55
	40								
<b>Average Thicknesses:</b>	37	69	38	117	32	127	47	156	48

Table 4.14. Calculation of average thicknesses for lead tin yellow and lead white layers

Looking at the table above, the layers are quite inhomogeneous, in particular in the 2 level, the lead tin yellow is the thinnest (8  $\mu\text{m}$  less than the mean value) and it is the thicker in the 4 level (8  $\mu\text{m}$  more than the mean value). The lead white layers grow from 69 $\mu\text{m}$  to 156 $\mu\text{m}$ .

Below there is an outline of the mockup in section:



Figure 4.15. Outline of lead tin yellow structure

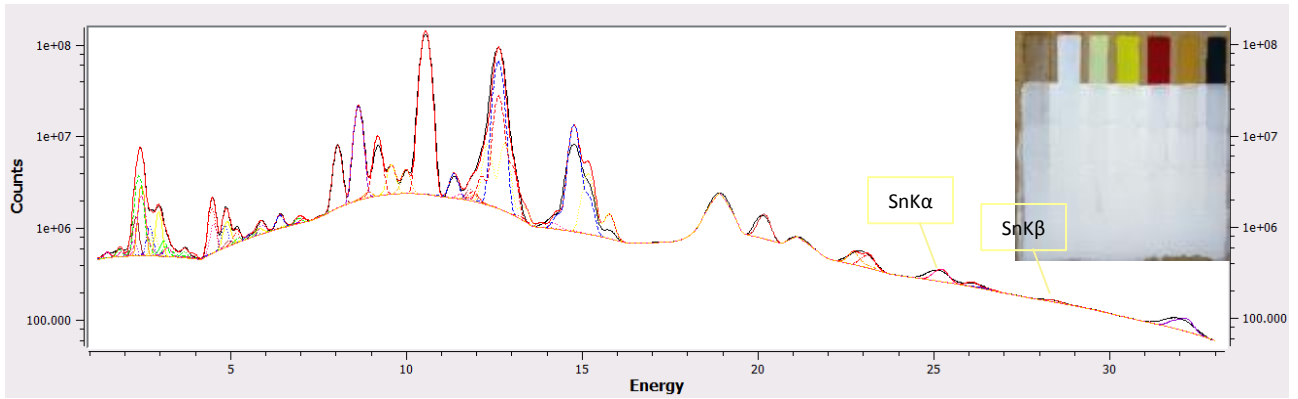


Figure 4.16. Spectra of the third sample. Below the yellow and red lines highlight the Sn-K $\alpha$  and Sn-K $\beta$  peaks.

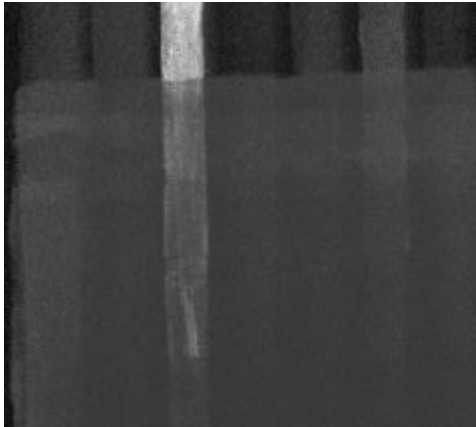


Figure 4.17a. Sn-K map; 850ms time per pixel and 500 $\mu$ m step size.

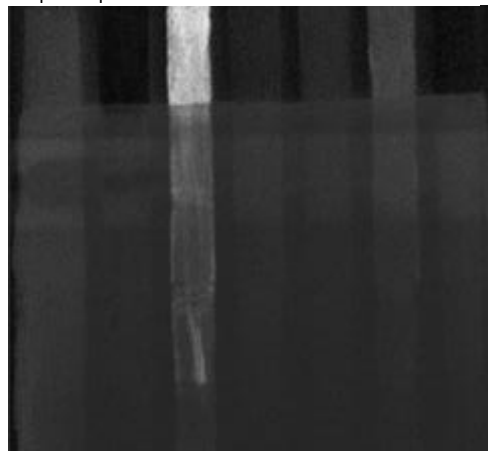
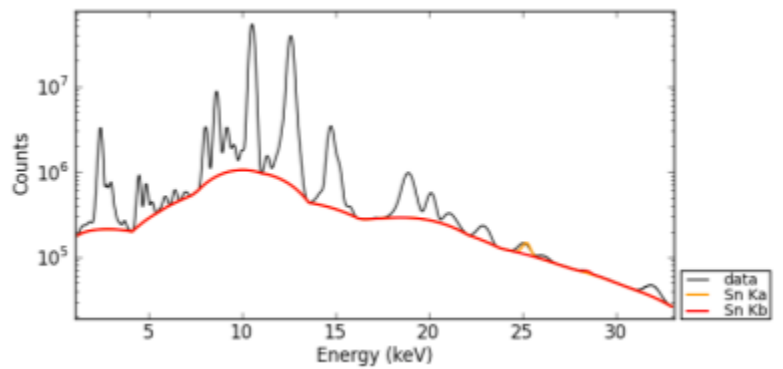


Figure 4.17b. Sn-K map; 1000ms time per pixel and 500 $\mu$ m step size.

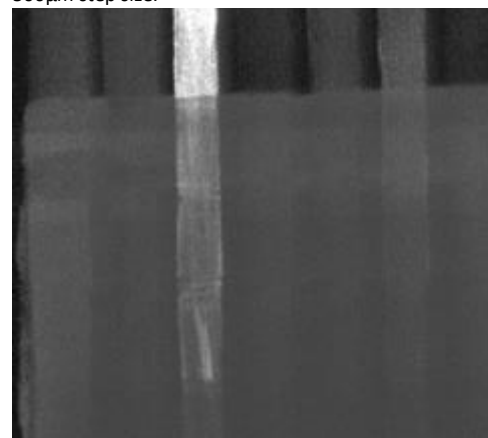
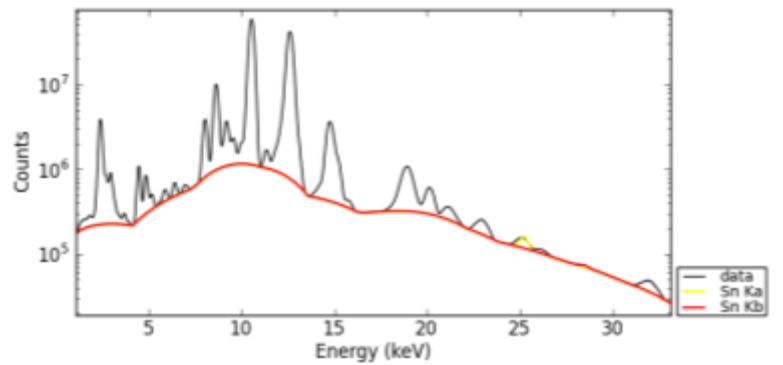
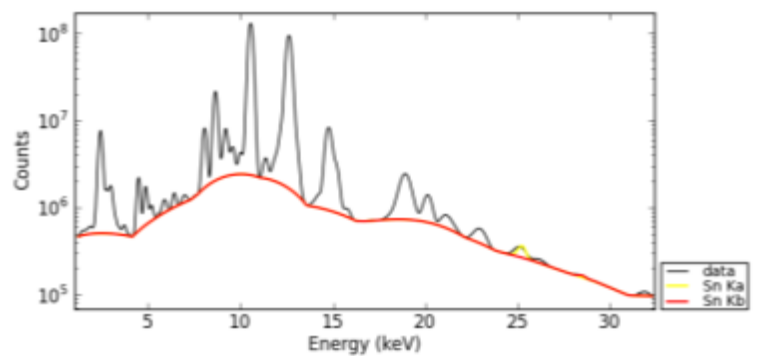


Figure 4.17c. Sn-K map; 2500ms time per pixel and 500 $\mu$ m step size.



In the table below there are data of azurite pigment analyzed and data for the calculation of sensitivity and limit of detection.



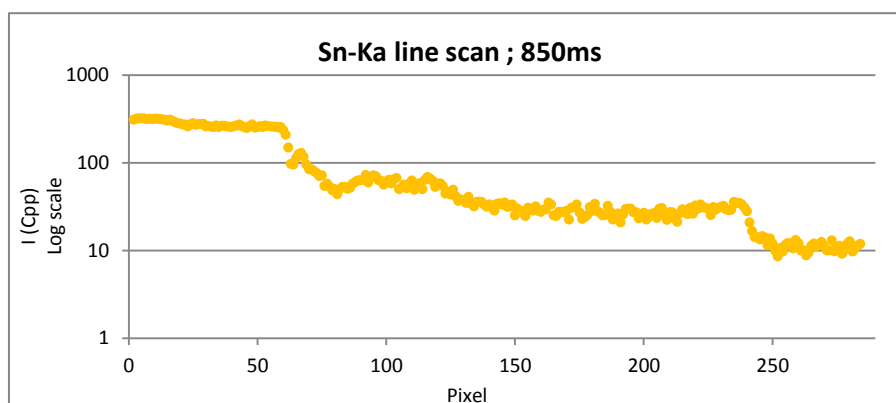
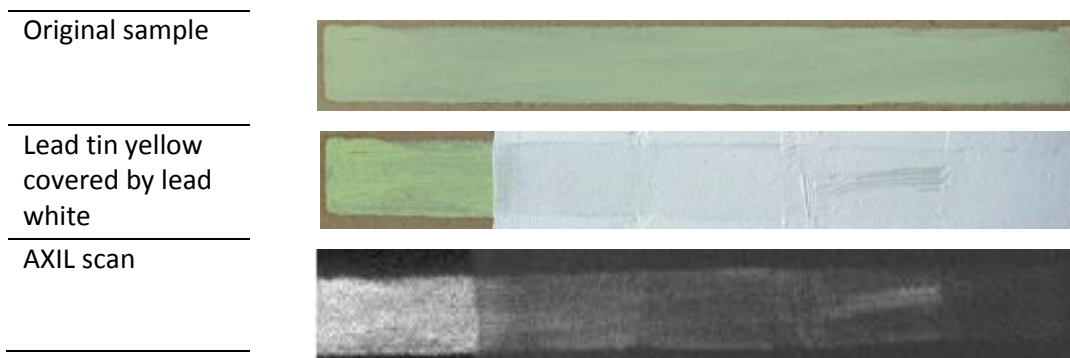
Figure 4.18. Pigment used in the study

<b>Element of interest</b>	Tin (Sn)	<b>X-Ray excitation energy for Sn-K</b>	K = 29,2 keV
<b>Pigment provenience</b>	Kremer	<b>mass attenuation coefficient (<math>\mu_0</math>)</b>	26,09 cm <sup>2</sup> /g
<b>Atomic Number (Z)</b>	50	<b>X-Ray fluorescent energy for Sn-K<math>\alpha</math></b>	K $\alpha$ = 25,27 keV
<b>Density of lead white (<math>\rho</math>)</b>	5,11 g/cm <sup>3</sup>	<b>mass attenuation coefficient (<math>\mu_f</math>)</b>	37,84 cm <sup>2</sup> /g
<b>Density of pigment (<math>\rho</math>)</b>	6,23 g/cm <sup>3</sup>	<b>Cos<math>\alpha</math></b>	0,000
<b>Concentration (C<sub>i</sub>)</b>	19,88	<b>Cos<math>\beta</math></b>	0,707
<b>Levels</b>	<b>Absorption factor for Pb (A<sub>1</sub>)</b>	<b>Absorption factor for Sn (A<sub>2</sub>)</b>	<b>Irradiated mass (mg)</b>
0 level	1,000	0,747	4,58
1 level	0,907	0,743	4,65
2 level	0,848	0,774	3,99
3 level	0,836	0,693	5,82
4 level	0,802	0,688	5,95

Table 4.15. Data for the quantitative analysis of Sn.

Results for

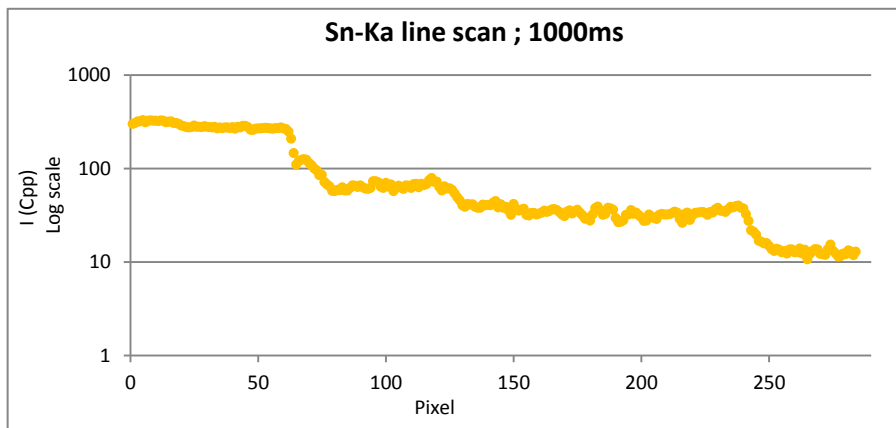
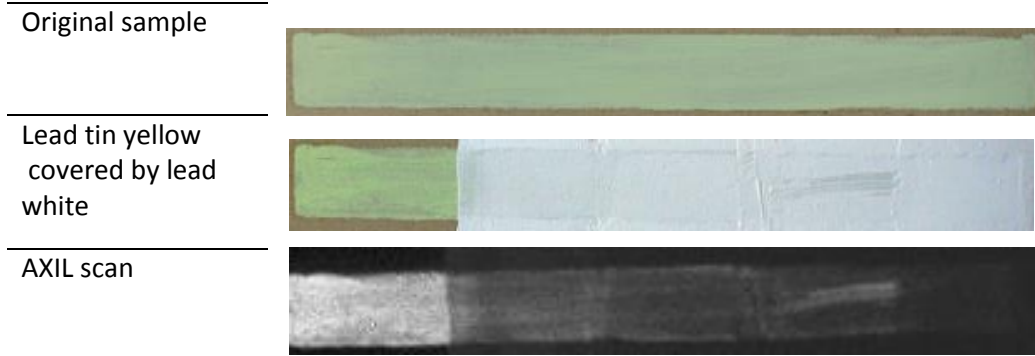
Instrument: AXIL ; Time per Pixel: 8500ms ; Step size: 500 $\mu$ m ; Total time: 16 hours and 18 minutes





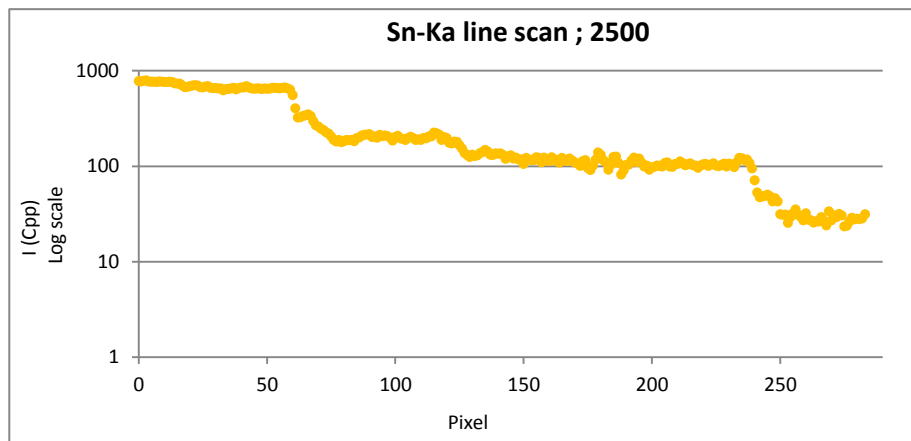
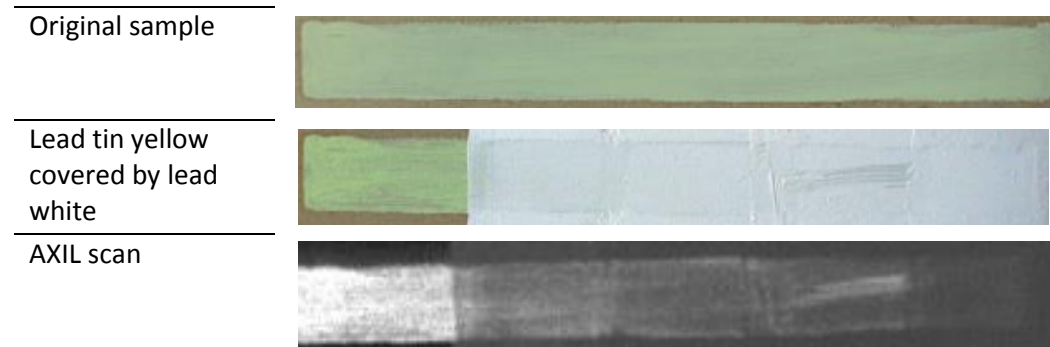
Results for:

Instrument: AXIL ; Time per Pixel: 1000ms ; Step size: 500 $\mu$ m ; Total time: 19 hours and 10 minutes



Results for:

Instrument: AXIL ; Time per Pixel: 2500ms ; Step size: 500 $\mu$ m ; Total time: 147 hours and 56 minutes


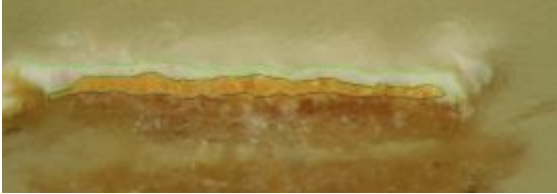
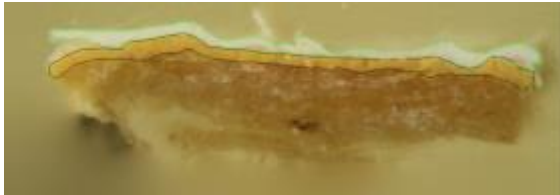




<b>SCAN: 850ms 500µm</b>	<b>Intensity average (cps)</b>	<b>St.Dev.</b>	<b>Sensitivity (cpp/mg)</b>	<b>Limit of Detection (µg)</b>
0 level	326	27,95	95	969
1 level	68	8,12	22	1087
2 level	36	4,34	14	839
3 level	32	3,66	10	1049
4 level	13	1,80	4	1388
<b>SCAN: 1000ms 500µm</b>				
0 level	286	21,12	84	758
1 level	64	5,05	20	739
2 level	37	4,10	14	866
3 level	32	3,11	10	981
4 level	13	1,26	4	951
<b>SCAN: 2500ms 500µm</b>				
0 level	275	19,57	81	729
1 level	78	4,48	25	537
2 level	48	4,22	18	684
3 level	42	1,71	12	416
4 level	12	3,07	4	2518

**Table 4.16.** Results for Sn.

Looking at the table above intensity and sensitivity decrease with the growth of lead white thicknesses. Limit of detection should increase with the growth of the lead white thickness, but it is not true due probably to the inhomogeneity of the layers and to the influence of the closer Rh-compton and Rayleigh peaks. Moreover the few samples analyzed cannot give excellent data.

**Sample1: Naples yellow  $Pb_2Sb_2O_7$**

Description	Samples taken from the five levels
0 level Naples yellow average thickness: 57,11 $\mu\text{m}$	 5X magnification
1 level Naples yellow average thickness: 46 $\mu\text{m}$ Lead white average thickness: 54 $\mu\text{m}$	 6,3X magnification
2 level Naples yellow average thickness: 58 $\mu\text{m}$ Lead white average thickness: 77 $\mu\text{m}$	 5X magnification
3 level Naples yellow average thickness: 39 $\mu\text{m}$ Lead white average thickness: 86 $\mu\text{m}$	 5X magnification
4 level Naples yellow average thickness: 51 $\mu\text{m}$ Lead white average thickness: 161 $\mu\text{m}$	 6,3X magnification

**Table 4.17.** Cross sections of the five samples taken from Naples yellow paint layer.

Naples Yellow	0 level	1 level		2 level		3 level		4 level	
	$\mu\text{m Sb}$	$\mu\text{m Pb}$	$\mu\text{m Sb}$	$\mu\text{m Pb}$	$\mu\text{m Sb}$	$\mu\text{m Pb}$	$\mu\text{m Sb}$	$\mu\text{m Pb}$	$\mu\text{m Sb}$
Values taken on the cross sections photos by Dino Capture	44	55	42	59	56	84	35	159	73
	49	53	40	73	47	84	44	169	35
	24	29	62	100	56	91	51	199	47
	69	62	64	55	74		26	109	40
	67	35	36	98				171	58
	53	89	29						
	66								
	69								
73									
<b>Average Thicknesses:</b>	<b>57</b>	<b>54</b>	<b>46</b>	<b>77</b>	<b>58</b>	<b>86</b>	<b>39</b>	<b>161</b>	<b>51</b>

Table 4.18. Calculation of average thicknesses for Naples Yellow and lead white layers

Looking at the table above, the layers are quite inhomogeneous, the Naples yellow layer has different measurements from 39  $\mu\text{m}$  for the 3 level to a maximum of 58  $\mu\text{m}$  for the 2 level. The lead white layers grow from 54  $\mu\text{m}$  to 161  $\mu\text{m}$ , it has been noted also that the 3 level is only 10  $\mu\text{m}$  thicker than the previous (it should be more or less 40  $\mu\text{m}$  thicker).

Below there is an outline of the mockup in section:

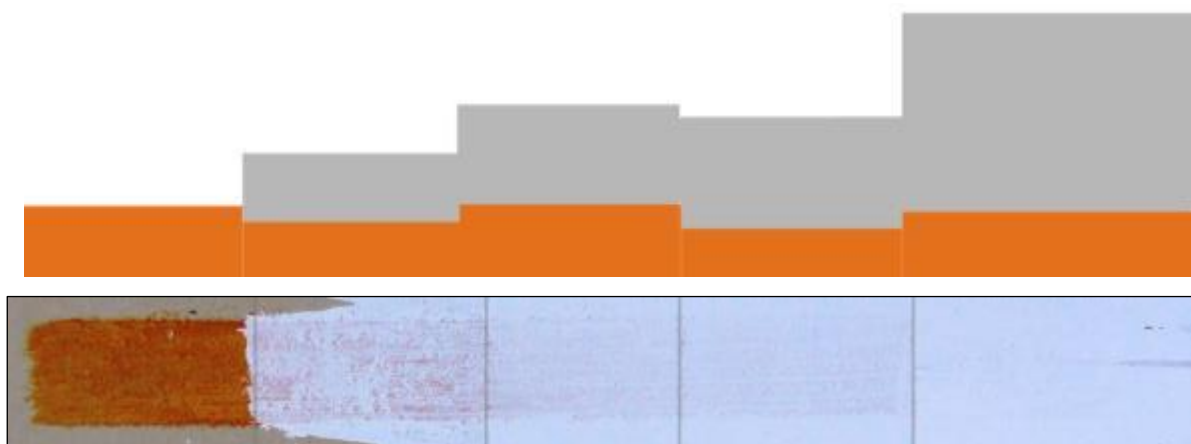


Figure 4.18. Outline of Naples yellow structure

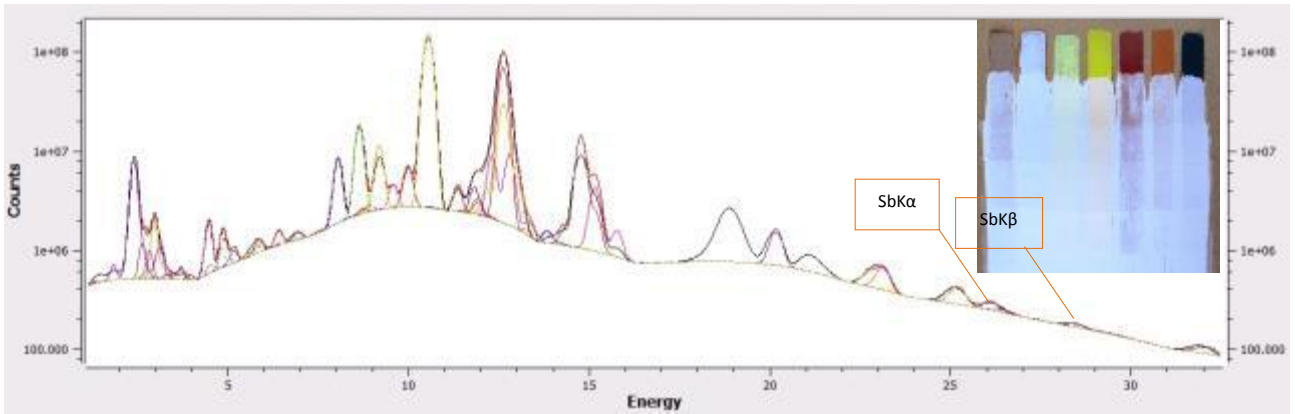


Figure 4.19 Spectra of the first sample. Below the red and blue lines highlight the Sb-K peak.

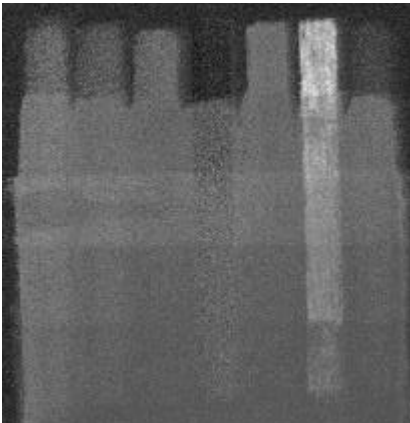


Figure 4.20a. Sb-K map; 850ms time per pixel and 500 $\mu$ m step size.

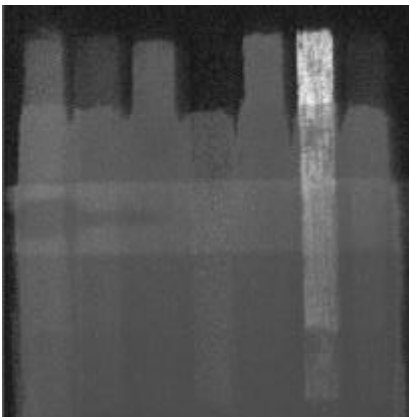
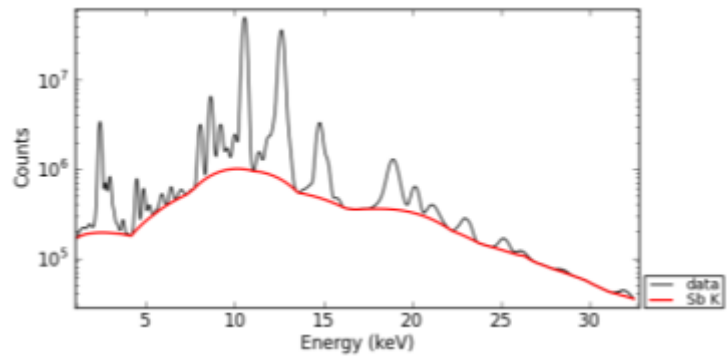


Figure 4.20b. Sb-K map; 1000ms time per pixel and 500 $\mu$ m step size.

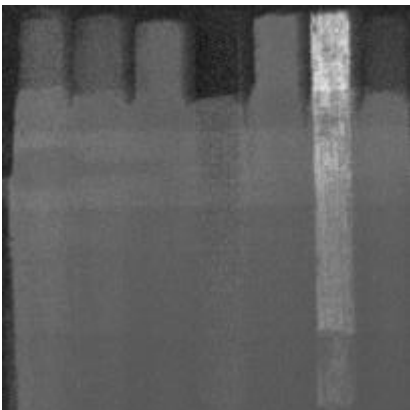
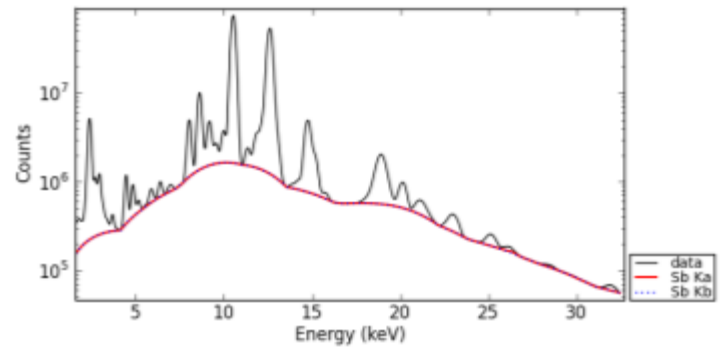
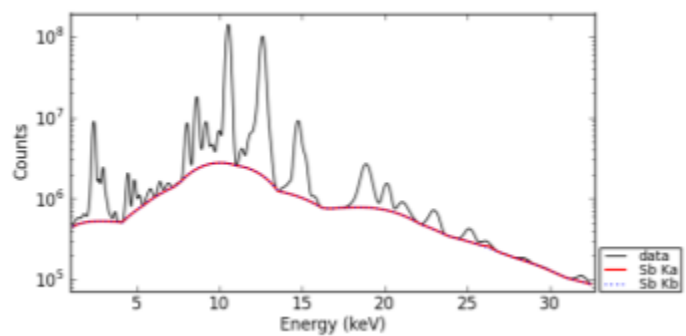


Figure 4.20. Sb-K map; 2500ms time per pixel and 500 $\mu$ m step size.



In the table below there are data of azurite pigment analyzed and data for the calculation of sensitivity and limit of detection.



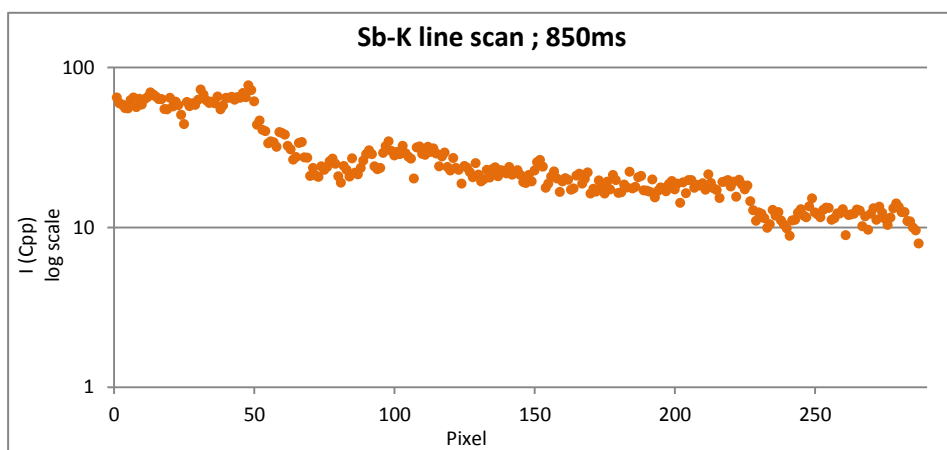
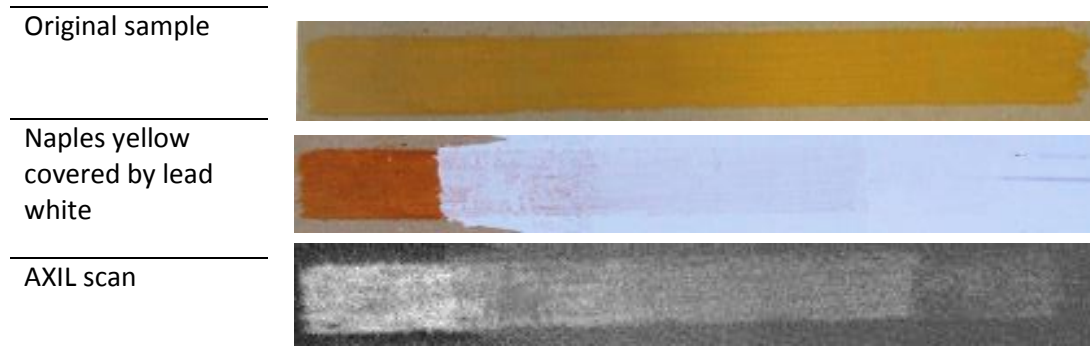
Figure 4.21. Error! No text of specified style in

<b>Element of interest</b>	Antimony (Sb)	<b>X-Ray excitation energy for Cd-K</b>	30,491 cm <sup>2</sup> /g
<b>Pigment provenience</b>	Michael Harding	<b>Mass attenuation coefficient (μ<sub>0</sub>)</b>	30,49 KeV
<b>Atomic Number (Z)</b>	51	<b>X-Ray fluorescent energy for Cd-Kα</b>	26,357 cm <sup>2</sup> /g
<b>Density of lead white (ρ)</b>	5,11 g/cm <sup>3</sup>	<b>Mass attenuation coefficient (μ<sub>f</sub>)</b>	26,36 KeV
<b>Density of pigment (ρ)</b>	5,94 g/cm <sup>3</sup>	<b>Cosα</b>	0,000
<b>Concentration (C<sub>i</sub>)</b>	31,7	<b>Cosβ</b>	0,707
<b>Levels</b>			
	<b>Absorption factor for Pb (A<sub>1</sub>)</b>	<b>Absorption factor for Cd (A<sub>2</sub>)</b>	<b>Irradiated mass (mg)</b>
0	1,000	0,738	8,47
1	0,927	0,781	6,84
2	0,897	0,734	8,62
3	0,886	0,809	5,80
4	0,797	0,761	7,58

Table 4.19 Data for the quantitative analysis of Sb.

Results for:

Instrument: AXIL; Time per Pixel: 8500ms ; Step size: 500μm ; Total time: 23 hours and 16 minutes



Results for.

Instrument: AXIL ; Time per Pixel: 1000ms ; Step size: 500 $\mu$ m ; Total time: 31 hours and 6 minutes

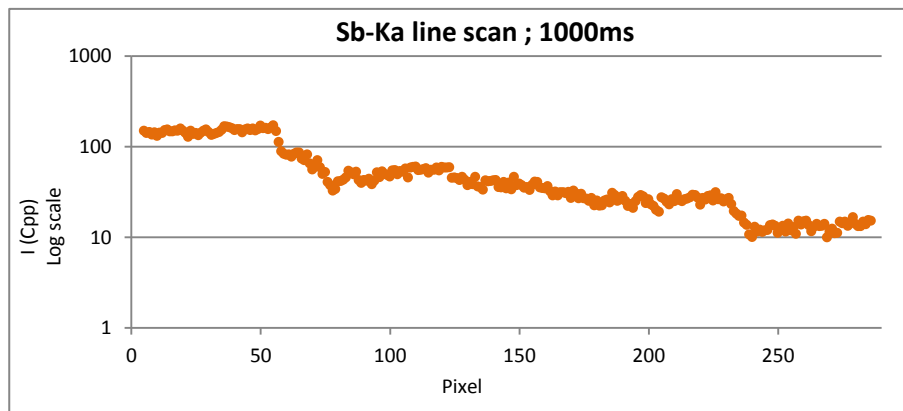
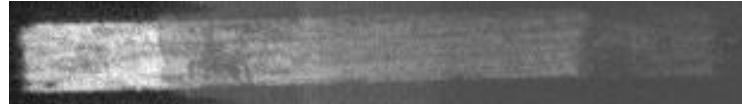
Original sample



Naples yellow covered by lead white



AXIL scan



Results for:

Instrument: AXIL ; Time per Pixel: 2500ms ; Step size: 500 $\mu$ m ; Total time: 71 hours and 16 minutes

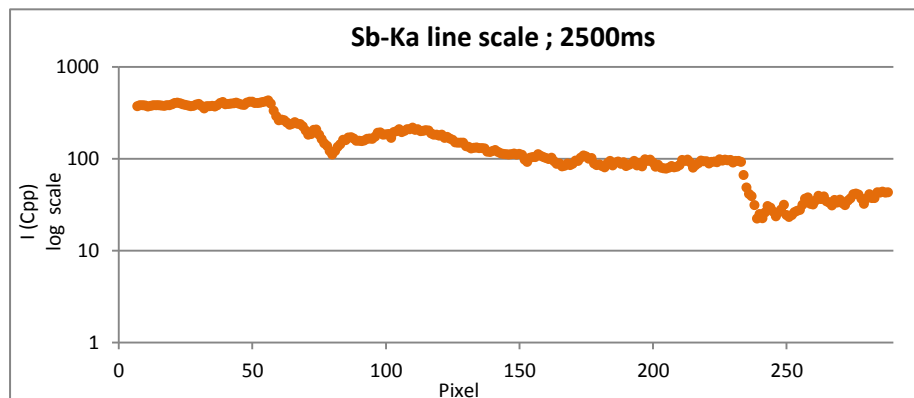
Original sample



Naples yellow covered by lead white



AXIL scan



<b>SCAN: 850ms 500µm</b>	<b>Intensity average (cps)</b>	<b>St.Dev.</b>	<b>Sensitivity (cps/mg)</b>	<b>Limit of Detection (µg)</b>
0 level	73	6,65	12	1719
1 level	31	4,41	6	2088
2 level	24	2,93	4	2093
3 level	21	1,90	5	1110
4 level	14	1,54	3	1518
<b>SCAN: 1000ms 500µm</b>				
0 level	150	9,96	24	1246
1 level	51	7,23	10	2116
2 level	32	5,80	6	3092
3 level	26	2,66	6	1284
4 level	13	1,53	3	1609
<b>SCAN: 2500ms 500µm</b>				
0 level	155	6,42	25	775
1 level	70	9,98	14	2101
2 level	43	5,54	7	2221
3 level	36	2,39	9	834
4 level	13	2,50	3	2601

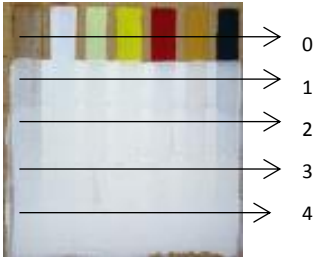

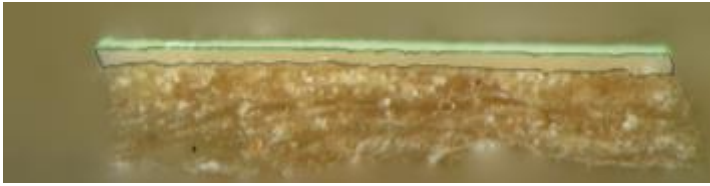

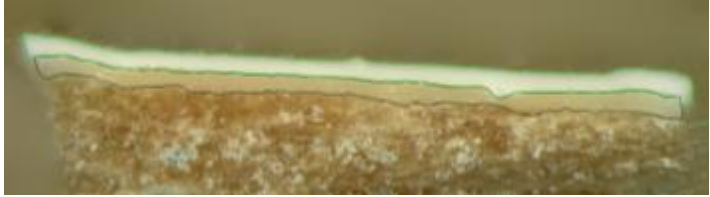
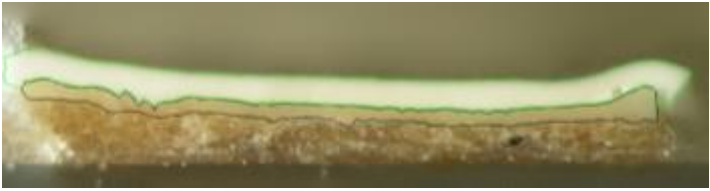
**Table 4.20.** Results for Sb.

As we noticed for the other elements and from the theory, sensitivity increases with time per pixel and decreases with the growth of lead white layers.

Limit of detections almost always increases with the growth of lead white, as we expected from the theory. In the scan with 2,5 seconds per pixel we have in "0 level" a minimum of 755 µg of antimony which could be detected, instead of 2601 µg detected in the "4 level". Most of the problems are in the 3 and 4 levels, where fluorescences come from Naples yellow are difficult to be detected and to give meaningful data.



**Sample 3: Barium Sulfate BaSO<sub>4</sub>**

Description	Samples taken from the five levels 
0 level Barium sulfate average thickness: 58,32 μm	 5X magnification
1 level Barium sulfate average thickness: 60,88 μm Lead white average thickness: 42,95 μm	 4X magnification
2 level Barium sulfate average thickness: 76,48 μm Lead white average thickness: 73,97 μm	 6X magnification
3 level Barium sulfate average thickness: 66,83 μm Lead white average thickness: 101,15 μm	 4X magnification
4 level Barium sulfate average thickness: 73,25 μm Lead white average thickness: 148,20 μm	 3,2X magnification

**Table 4.21.** Cross sections of the five samples taken from barium sulfate paint layer.

Barium Sulfate	0 level	1 level		2 level		3 level		4 level	
	μm Ba	μm Pb	μm Ba	μm Pb	μm Ba	μm Pb	μm Ba	μm Pb	μm Ba
Values taken on the cross sections photos by Dino Capture	60,44	36,59	56,17	73,03	70,22	84,27	83,08	188,18	71,67
	67,11	38,07	76,15	84,27	78,85	89,89	81,46	145,58	64,95
	55,93	49,27	62,95	81,46	73,03	78,65	39,43	138,86	67,19
	55,94	44,79	67,19	61,80	81,46	101,28	56,18	161,25	62,71
	53,69	31,35	69,43	67,42	78,85	87,08	56,18	134,38	62,71
	53,69	51,51	65,19	75,84		103,93	81,27	145,58	87,59
	59,33	47,25	29,12			126,40	70,22	154,54	86,35
	60,40	44,79				137,67		134,38	82,87
								136,69	
								136,62	
								156,77	
								145,58	
<b>Average Thicknesses:</b>	<b>58,32</b>	<b>42,95</b>	<b>60,88</b>	<b>73,97</b>	<b>76,48</b>	<b>101,15</b>	<b>66,83</b>	<b>148,20</b>	<b>73,25</b>

Table 4.22. Calculation of average thicknesses for barium sulfate and lead white layers

In the tabel above there are a list of thcknesses taken from the samples shown in the page before. The range of the thick of barium sulfate is very high: from 58,32 μm for the 0 level, to 76,48 μm for the 2 level. Lead white thiknesses increase homogeneously from 42,95 μm to 148,20 μm. Below there is an outline of the mockeup in section:

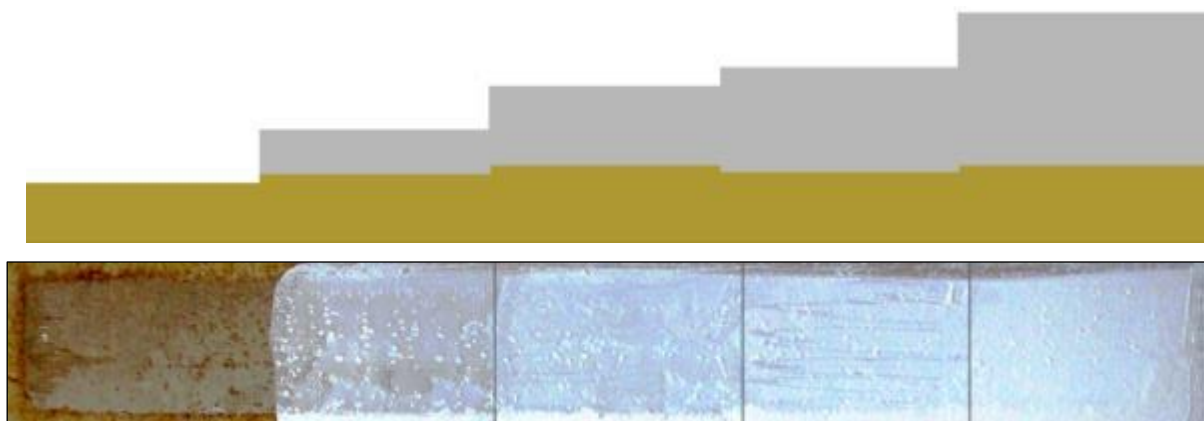


Figure 4.22 Outline of Barium sulfate structure

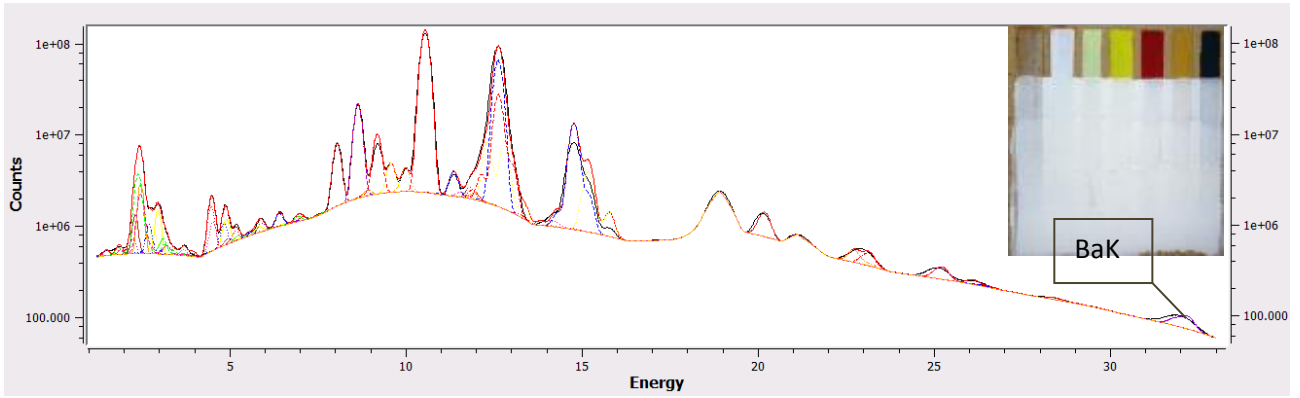


Figure 4.23. Spectra of the third sample. Below the green line highlights the Ba-K peak.

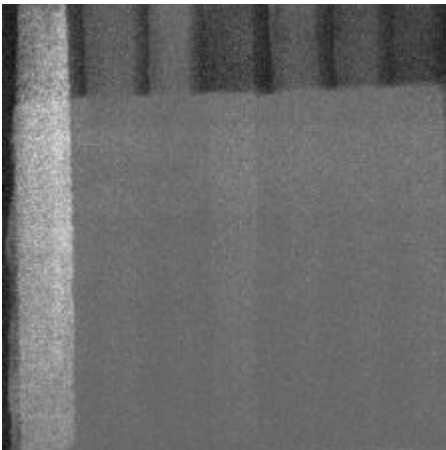


Figure 4.24a. BaK map; 850ms time per pixel and 500um step size.

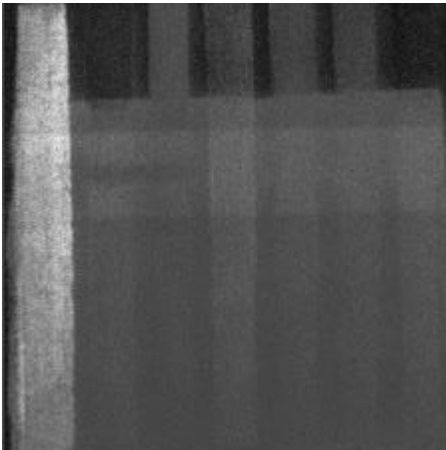
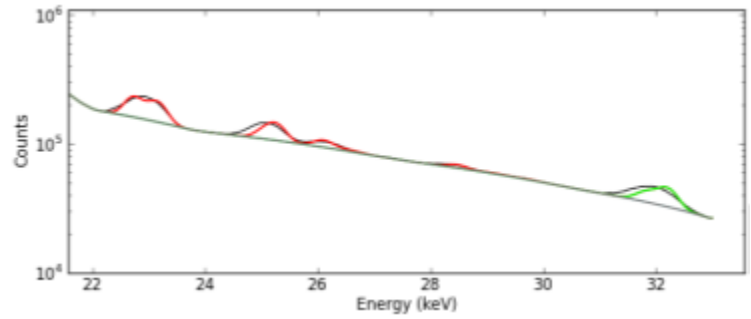


Figure 4.24b. BaK map; 850ms time per pixel and 500um step size.

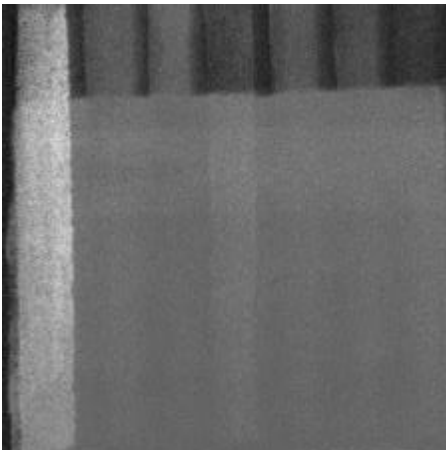
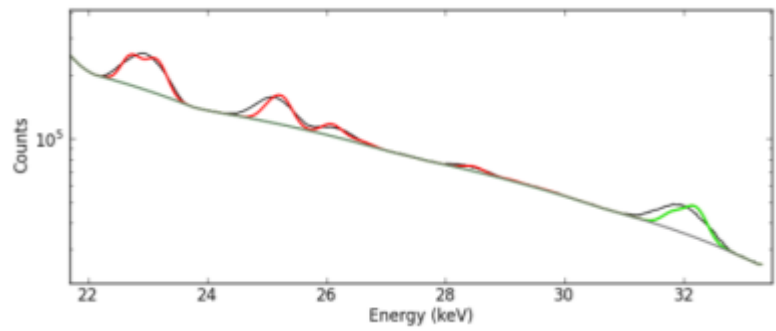
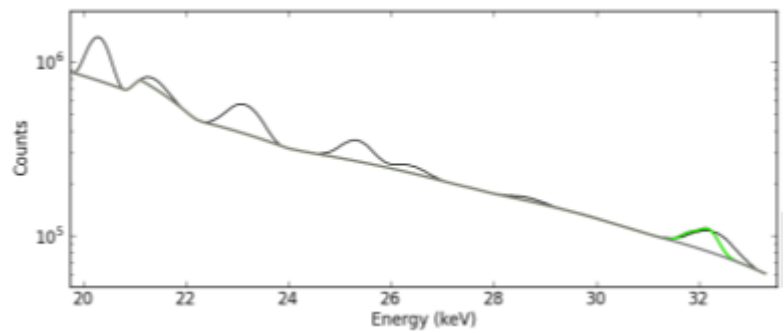


Figure 4.24c. BaK map; 850ms time per pixel and 500um step size.



In the table below there are data of azurite pigment analyzed and data for the calculation of sensitivity and limit of detection.



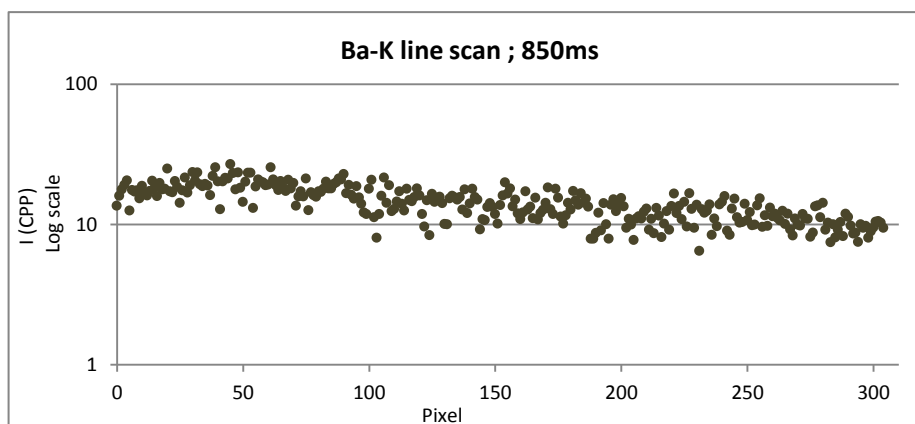
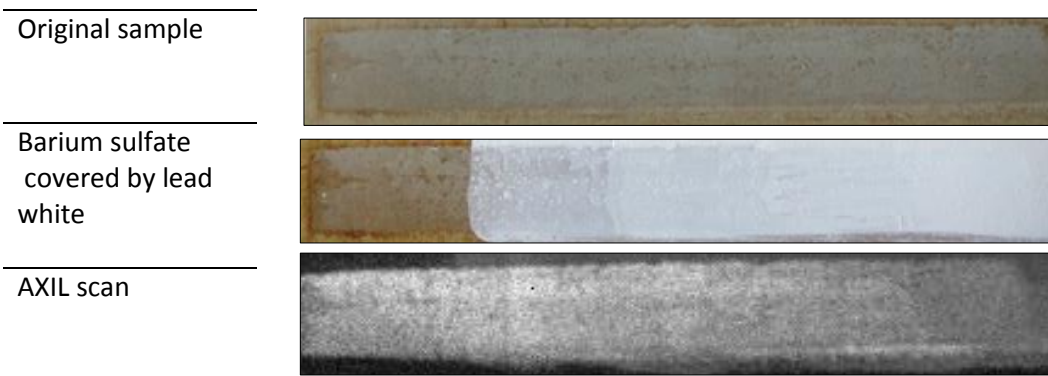
Figure 4.25 Pigment used in the study

<b>Element of interest</b>	Barium (Ba)	<b>X-Ray excitation energy for Ba-K</b>	K = 37,441 KeV
<b>Pigment provenience</b>	Kremer	<b>mass attenuation coefficient (<math>\mu_o</math>)</b>	1,412 cm <sup>2</sup> /g
<b>Atomic Number (Z)</b>	56	<b>X-Ray fluorescent energy for Ba-K<math>\alpha</math></b>	K $\alpha$ = 32,292 KeV
<b>Density of lead white (<math>\rho</math>)</b>	5,11 g/cm <sup>3</sup>	<b>mass attenuation coefficient (<math>\mu_f</math>)</b>	2,057 cm <sup>2</sup> /g
<b>Density of pigment (<math>\rho</math>)</b>	3,61 g/cm <sup>3</sup>	<b>Cos<math>\alpha</math></b>	0,000
<b>Concentration (C<sub>i</sub>)</b>	58,83	<b>Cos<math>\beta</math></b>	0,707
<b>Levels</b>	<b>Absorption factor for Pb (A<sub>1</sub>)</b>	<b>Absorption factor for Ba (A<sub>2</sub>)</b>	<b>Irradiated mass (mg)</b>
0	1,000	0,985	12,38
1	0,941	0,984	12,92
2	0,901	0,980	16,23
3	0,867	0,983	14,18
4	0,811	0,981	15,55

Table 4.23. Data for the quantitative analysis of Ba.

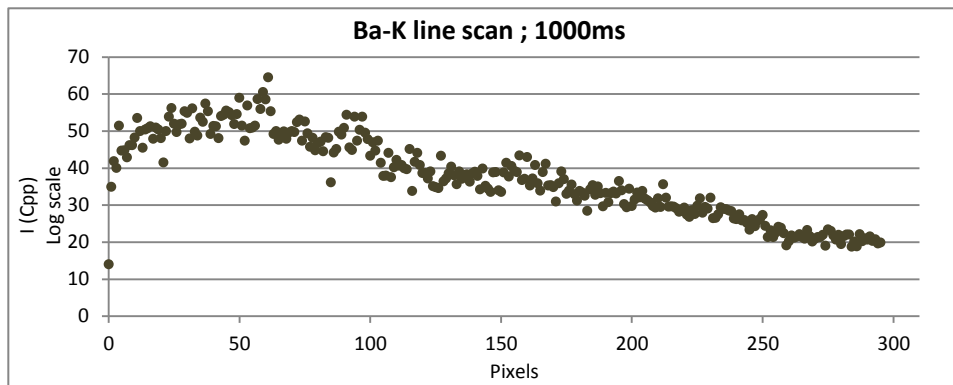
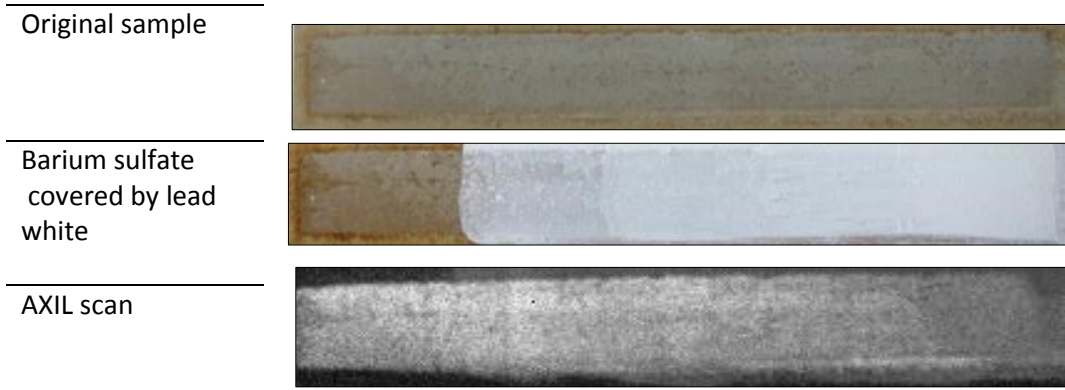
Results for:

Instrument: AXIL ; Time per Pixel: 8500ms ; Step size: 500 $\mu$ m ; Total time: 16 hours and 18 minutes



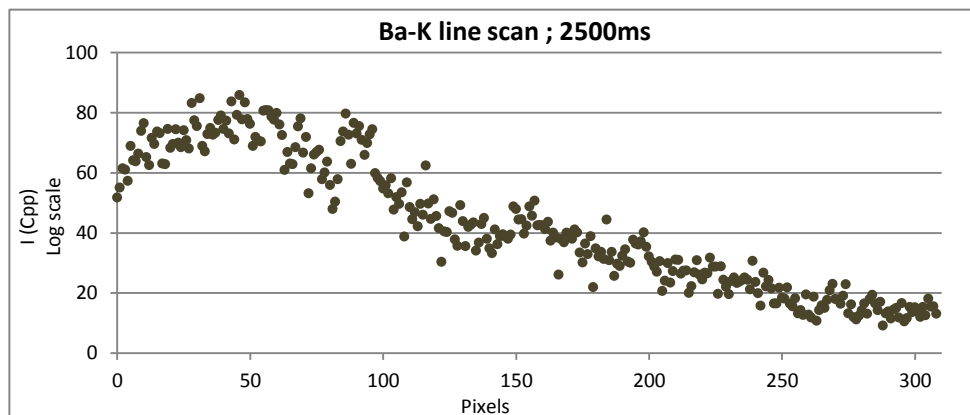
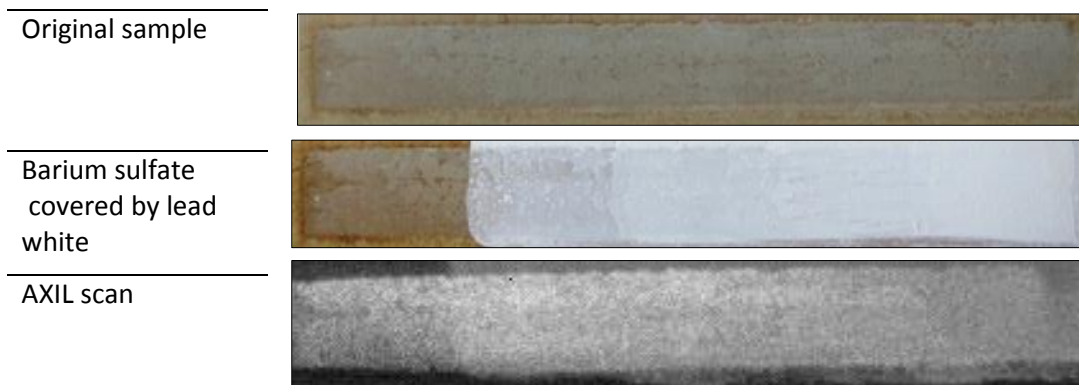
Results for:

Instrument: AXIL ; Time per Pixel: 1000ms ; Step size: 500 $\mu$ m ; Total time: 19 hours and 10 minutes



Results for:

Instrument: AXIL ; Time per Pixel: 2500ms ; Step size: 500 $\mu$ m ; Total time: 147 hours and 56 minutes



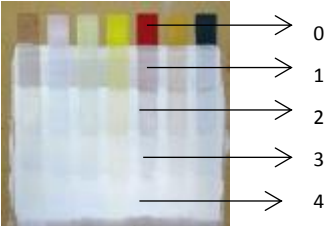

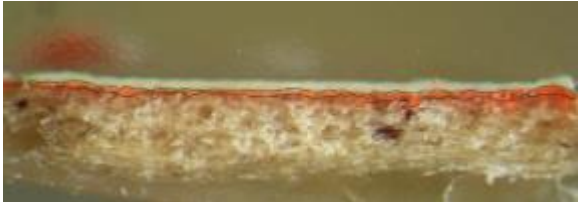
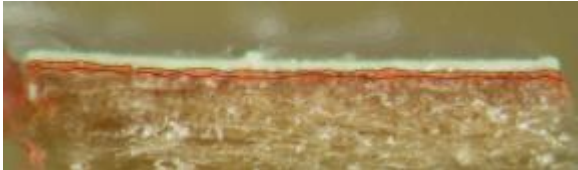


<b>SCAN: 850ms 500µm</b>	<b>Intensity average (cps)</b>	<b>St.Dev.</b>	<b>Sensitivity (cps/mg)</b>	<b>Limit of Detection (µg)</b>
0 level	22	3,72	2	6062
1 level	17	3,47	1	7387
2 level	16	3,13	1	8217
3 level	14	2,72	1	7179
4 level	12	1,88	1	5845
<b>SCAN: 1000ms 500µm</b>				
0 level	51	5,16	4	3688
1 level	41	5,36	3	4715
2 level	34	2,92	2	3714
3 level	28	2,55	2	3286
4 level	21	1,16	2	2044
<b>SCAN: 2500ms 500µm</b>				
0 level	29	2,87	2	3632
1 level	19	3,83	2	7391
2 level	14	1,91	1	5898
3 level	10	1,64	1	6119
4 level	6	1,23	0	7611

**Table 3.24.** Results for Ba.

The intensity and sensitivity of barium are the lowest detected among the seven elements analyzed. The maximum of intensity is in “0 layer”, between 22cps and 51cps, while the sensibility of the instrument for Ba is between 2cps/mg and 4cps/mg, which are very low values.

Limit of detection increases with the growth of lead white, but this is not always true because of the irregularity of layers, at least all the “0 level” have the lowest LODs.

### Sample 2: Vermilion HgS

Description	Samples taken from the five levels 
0 level Mercury-II sulfide average thickness: 21,38 $\mu\text{m}$	 Magnification: 5X
1 level Mercury-II sulfide average thickness: 20,79 $\mu\text{m}$ Lead white average thickness: 32,47 $\mu\text{m}$	 Magnification: 6,3X
2 level Mercury-II sulfide average thickness: 23,98 $\mu\text{m}$ Lead white average thickness: 57,22 $\mu\text{m}$	 Magnification: 5X
3 level Mercury-II sulfide average thickness: 23,87 $\mu\text{m}$ Lead white average thickness: 86,08 $\mu\text{m}$	 Magnification: 5X
4 level Mercury-II sulfide average thickness: 25,69 $\mu\text{m}$ Lead white average thickness: 111,07 $\mu\text{m}$	 Magnification: 5X

**Table 4.25** Cross sections of the five samples taken from vermilion paint layer.

Vermilion	0 level	1 level		2 level		3 level		4 level	
	$\mu\text{m Hg}$	$\mu\text{m Pb}$	$\mu\text{m Hg}$	$\mu\text{m Pb}$	$\mu\text{m Hg}$	$\mu\text{m Pb}$	$\mu\text{m Hg}$	$\mu\text{m Pb}$	$\mu\text{m Hg}$
Values taken on the cross sections photos by Dino Capture	39,15	35,01	49,02	47,62	22,41	88,24	17,32	113,11	25,13
	20,13	30,84	16,81	44,82	28,01	84,05	14,01	129,26	25,13
	19,02	36,41	11,20	49,02	28,01	88,24	23,81	147,22	30,73
	20,13	37,82	12,61	89,64	28,01	88,24	19,61	156,19	37,70
	19,02	35,01	15,41	63,03	28,01	98,04	21,06	104,19	21,54
	17,90	25,21	17,04	56,02	23,81	64,43	21,01	28,73	17,95
	19,02	30,81	30,81	50,42	14,01	85,48	25,21	98,81	21,62
	15,66	25,21	14,01		19,61	91,90	49,02		
	22,37	32,21	11,20				23,81		
		33,61	16,81						
		35,01	37,82						
			16,81						
<b>Average Thicknesses:</b>	<b>21,38</b>	<b>32,47</b>	<b>20,79</b>	<b>57,22</b>	<b>23,98</b>	<b>86,08</b>	<b>23,87</b>	<b>111,07</b>	<b>25,69</b>

Table 4.26. Calculation of average thicknesses for vermilion and lead white layers

Looking at the table above mercury layer is more or less homogeneous and lead white layers grows regularly from 32,47  $\mu\text{m}$  to 111,07  $\mu\text{m}$ .

Below there is an outline of the mockup in section:



Figure 4.26. Outline of vermilion structure



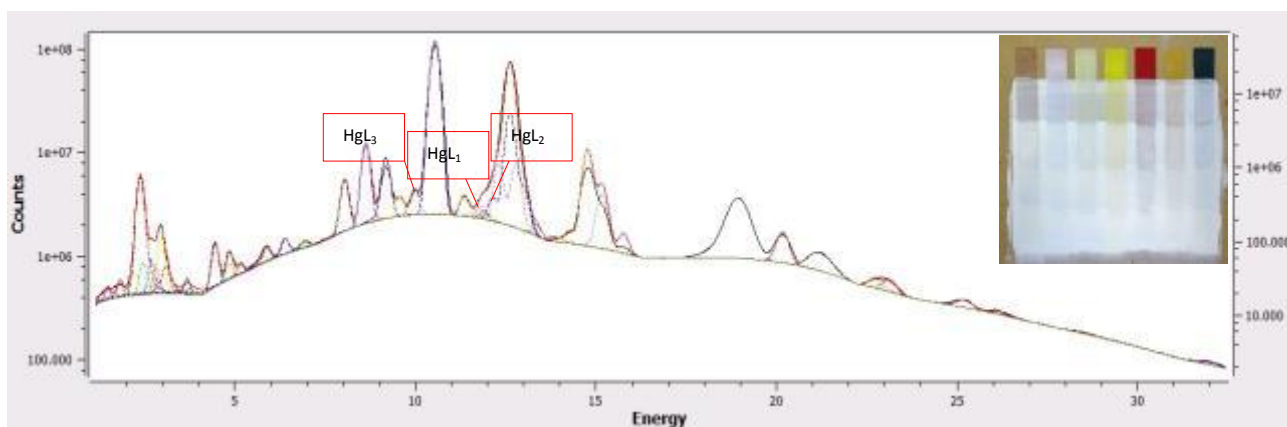


Figure 4.27. Spectra of the first sample. Below the blue, black and red lines highlight the HgL peaks.

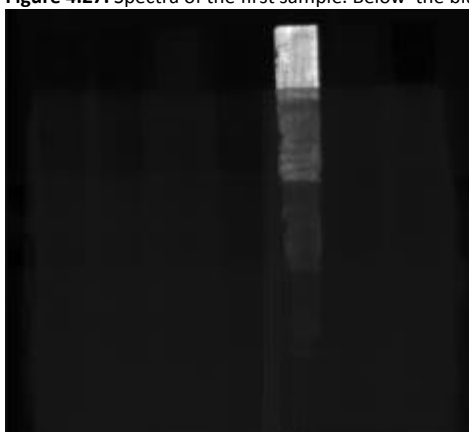


Figure 4.28a. HgL map; 850ms time per pixel and 500 $\mu$ m step size.

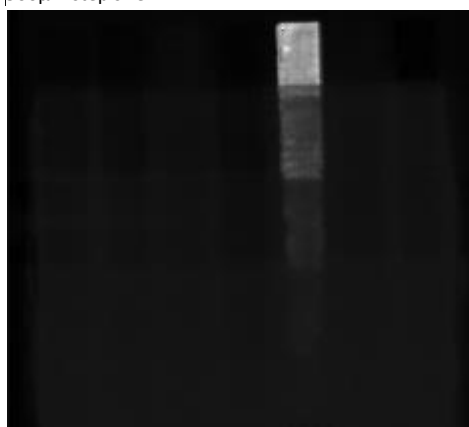
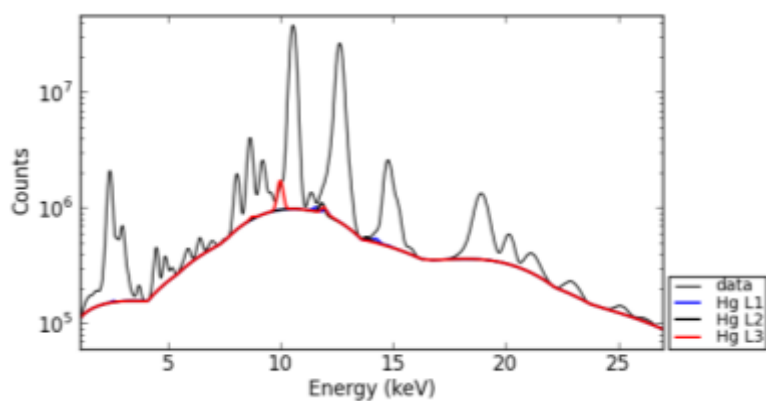


Figure 4.28b. HgL map; 1000ms time per pixel and 500 $\mu$ m step size.

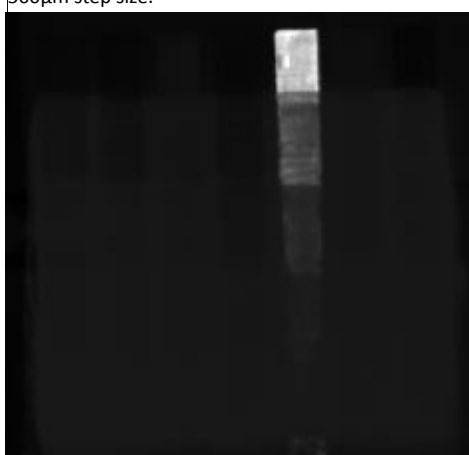
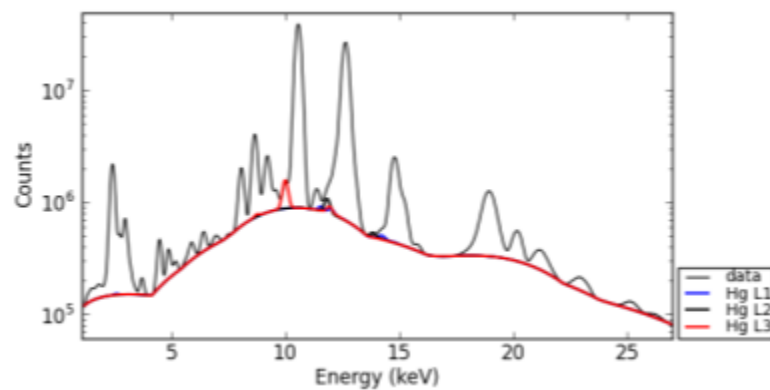
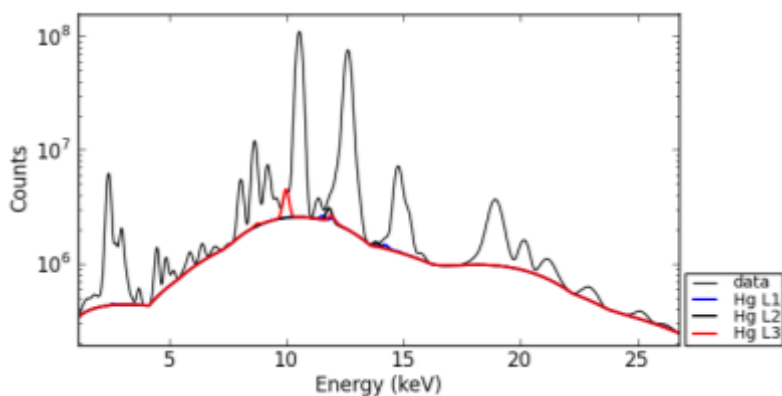


Figure 4.28c. HgL map; 2500ms time per pixel and 500 $\mu$ m step size.



In the table below there are data of azurite pigment analyzed and data for the calculation of sensitivity and limit of detection.



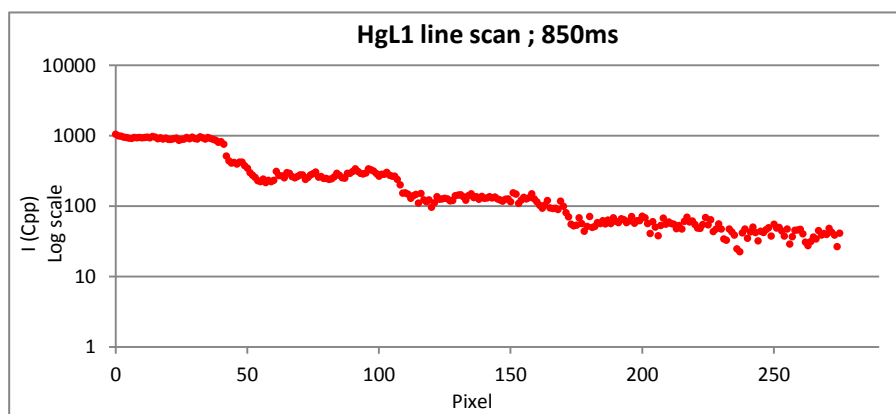
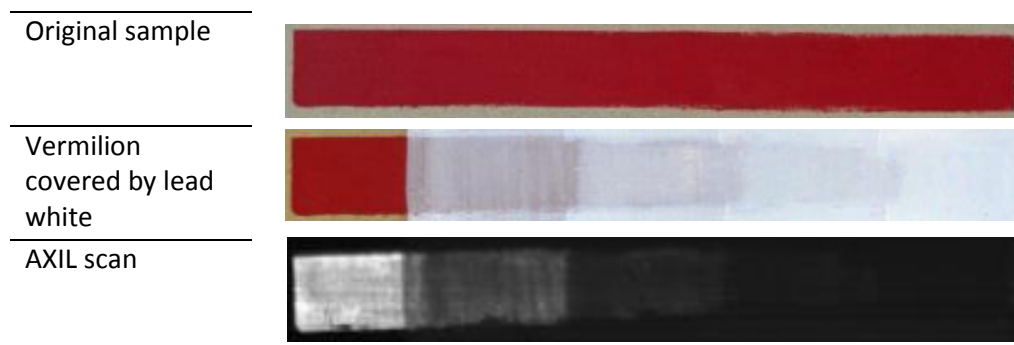
Figure 4.29. Pigment used in the study

<b>Element of interest</b>	Mercury (Hg)	<b>X-Ray excitation energy for Cd-K</b>	$L_1 = 8,31 \text{ KeV}$
<b>Pigment provenience</b>	Deffner & Johann	<b>mass attenuation coefficient (<math>\mu_0</math>)</b>	$1,80 \text{ cm}^2/\text{g}$
<b>Atomic Number (Z)</b>	80	<b>X-Ray fluorescent energy for Cd-K<math>\alpha</math></b>	$L_1 = 7,08 \text{ KeV}$
<b>Density of lead white (<math>\rho</math>)</b>	$5,11 \text{ g/cm}^3$	<b>mass attenuation coefficient (<math>\mu_f</math>)</b>	$2,67 \text{ cm}^2/\text{g}$
<b>Density of pigment (<math>\rho</math>)</b>	$6,375 \text{ g/cm}^3$	<b>Cos<math>\alpha</math></b>	
<b>Concentration (C<sub>i</sub>)</b>	86,22	<b>Cos<math>\beta</math></b>	
<b>Levels</b>			
	<b>Absorption factor for Pb (A<sub>1</sub>)</b>	<b>Absorption factor for Cd (A<sub>2</sub>)</b>	<b>Irradiated mass (mg)</b>
0	1,000	0,987	11,75
1	0,955	0,988	11,43
2	0,922	0,986	13,18
3	0,886	0,986	13,12
4	0,855	0,985	14,12

Table 4.27. Data for the quantitative analysis of Hg.

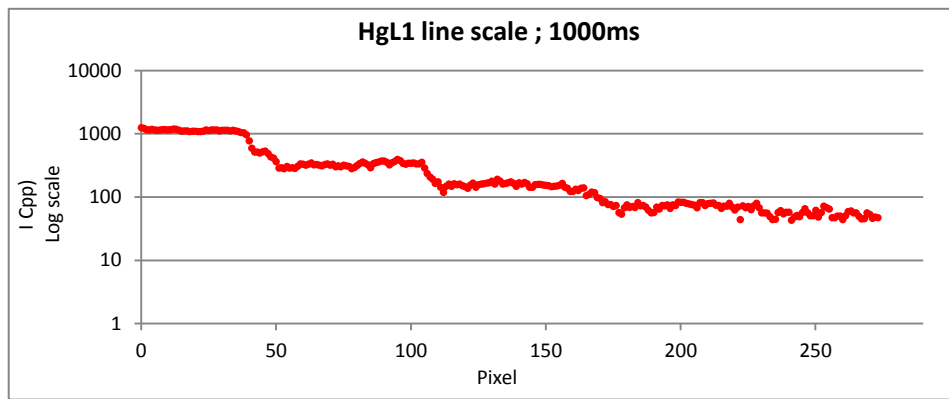
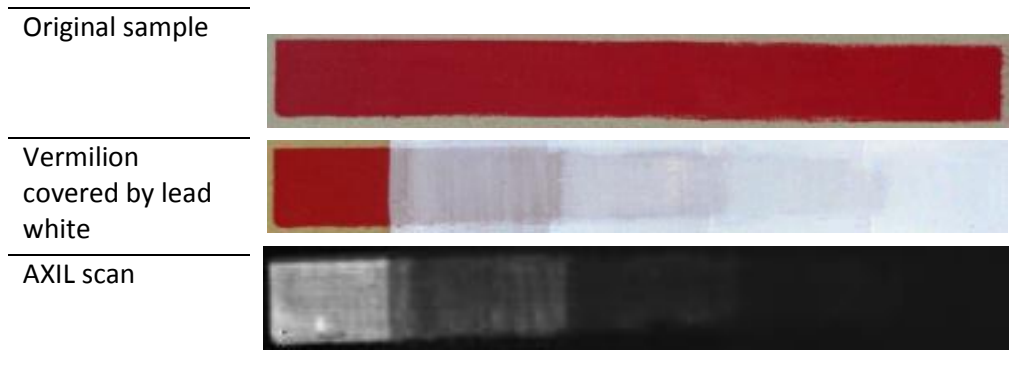
Results for:

Instrument: AXIL ; Time per Pixel: 850ms ; Step size: 500 $\mu\text{m}$  ; Total time: 22 hours and 50minuts



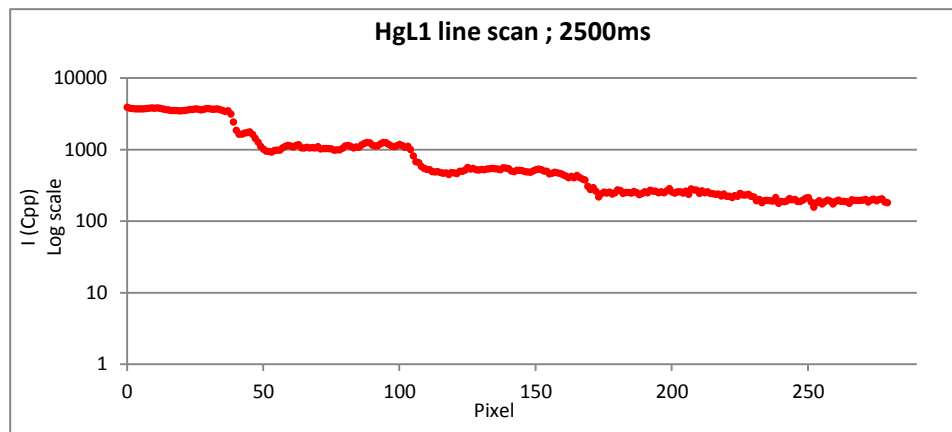
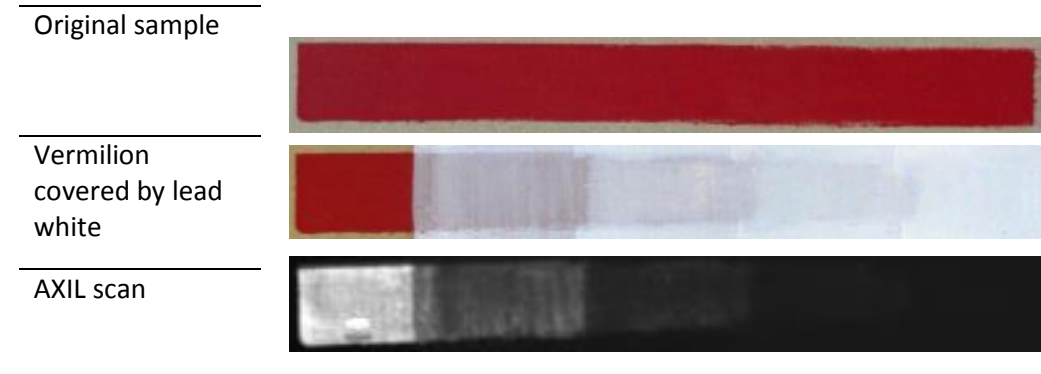
Results for:

Instrument: AXIL D ; Time per Pixel: 1000ms ; Step size: 500 $\mu$ m ; Total time: 26 hours and 52 minutes



Results for:

Instrument: AXIL D ; Time per Pixel: 2500ms ; Step size: 500 $\mu$ m ; Total time: 67 hours and 10 minutes



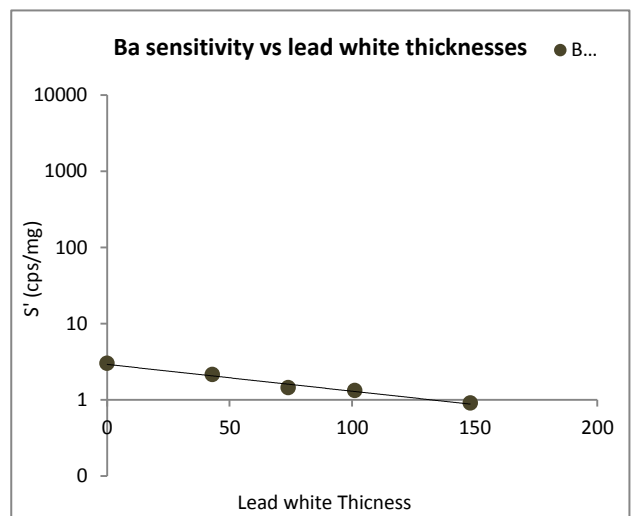
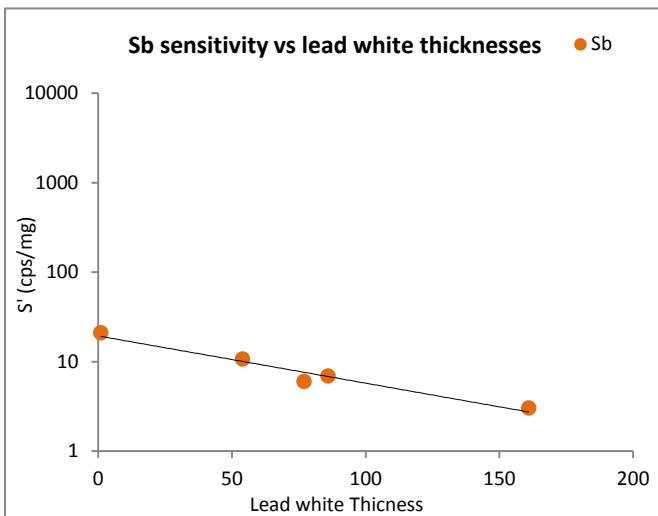
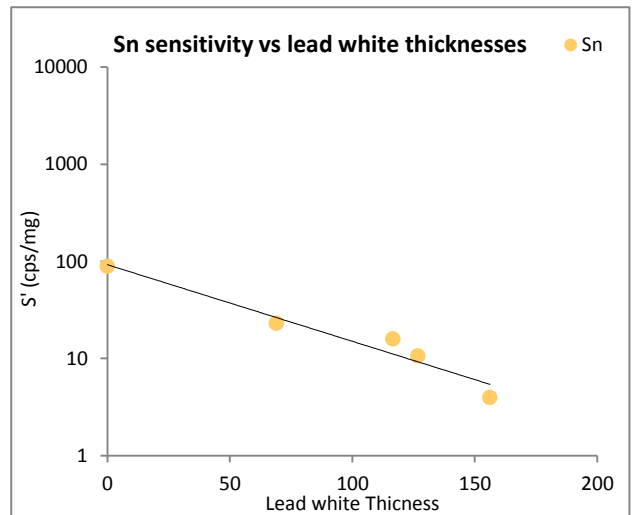
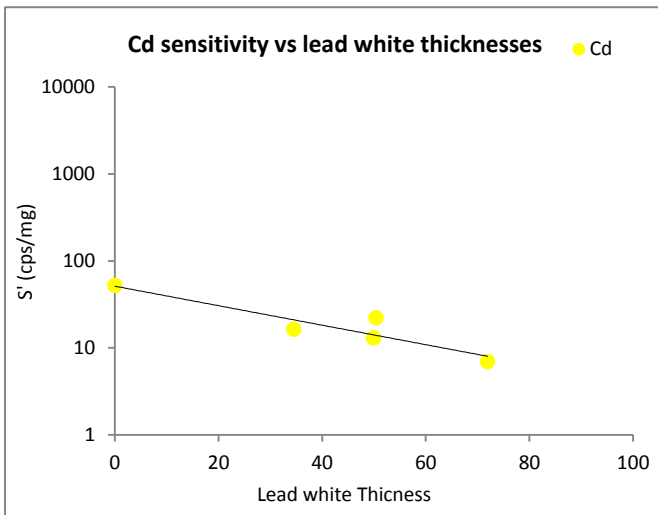
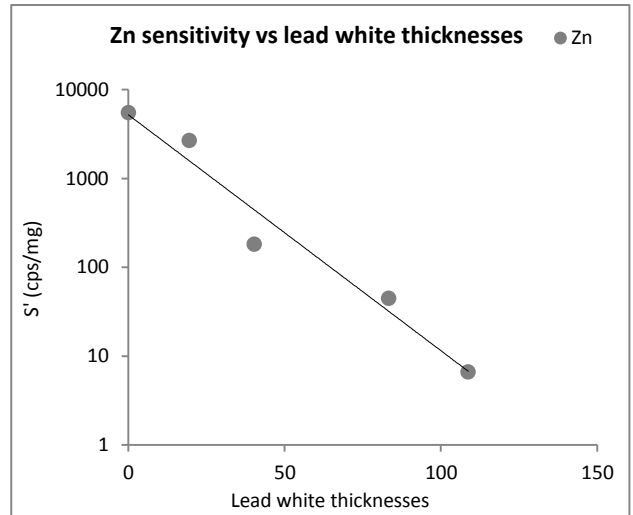
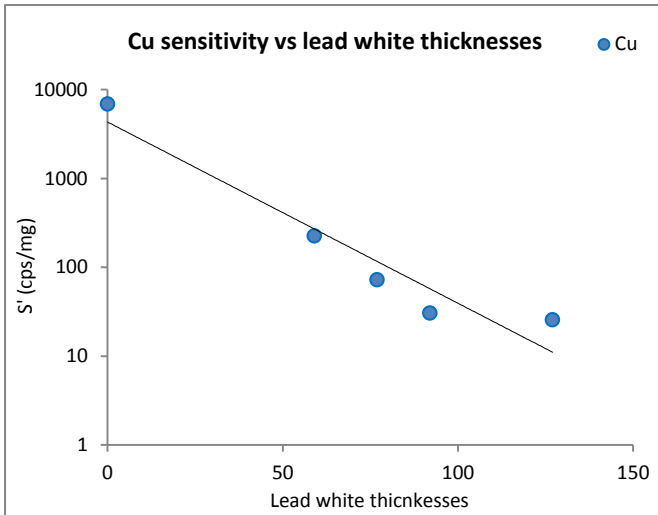
<b>SCAN: 850ms 500µm</b>	<b>Intensity average (cps)</b>	<b>St.Dev.</b>	<b>Sensitivity (cps/mg)</b>	<b>Limit of Detection (µg)</b>
0 level	1069	130,33	92	4244
1 level	324	32,04	30	3198
2 level	149	20,14	12	4866
3 level	68	8,99	6	4522
4 level	47	8,14	4	6128
<b>SCAN: 1000ms 500µm</b>				
0 level	1124	110,78	97	3429
1 level	326	27,24	30	2704
2 level	151	17,12	13	4070
3 level	72	7,64	6	3662
4 level	54	6,92	5	4604
<b>SCAN: 2500ms 500µm</b>				
0 level	1461	46,30	126	1103
1 level	434	34,04	40	2538
2 level	200	15,07	17	2715
3 level	101	5,27	9	1791
4 level	77	4,28	6	1992

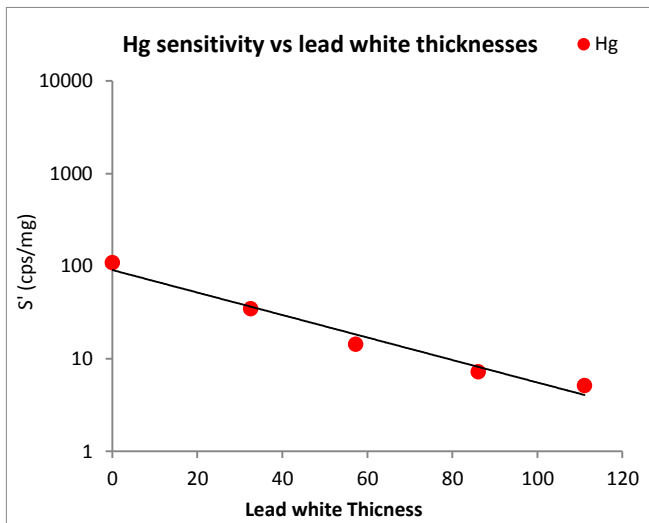
Table 4.28. Results for Hg.

As we have observed for the other elements, Intensity and Sensitivity decrease with the growth of lead white thicknesses. The value for the third scan seems to be higher than the other values of first and second scan, this is probably due to the higher amount of fluorescence detected and a overvaluation of dwell time. Limit of detection should increase with the growth of lead white, but this is not always true for this sample of vermilion.

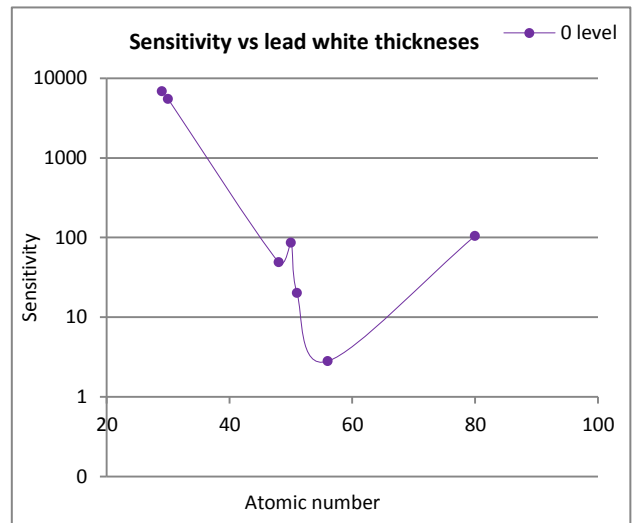
### 4.2.3 Discussion

The following Graphics show the behaviour of average sensitivity for each element versus the growth of lead white thicknesses.





Graphics 5.1 Behaviour of sensitivity with the growth of lead white



Graphic 5.2. Sensitivity versus atomic number

Sensitivity normalized to 1 second decreases with the growth of the covering lead white layer for all the selected elements in this project. Looking at the slopes of linear regressions lines, the seven elements can be divided in two groups: 1<sup>st</sup> group with Cu and Zn; 2<sup>nd</sup> group with Cd, Sn, Sb, Ba, while Hg is in the middle of the two groups.

The slopes of the regression lines for Cu and Zn are very high ( -58,34 for Cu and -44,50 for Zn ). It means that there is a big difference in detecting Cu and Zn in a surface layer rather than in covered layer. Furthermore it seems that it is not possible to obtain the white signals in Cu-K elemental maps when covering lead white layer is equal or thicker than 50 μm, while Zn-K maps clearly distinguish levels up to 100 μm of covering lead white layer ( different degrees of absorption ).

The slopes of the regression linear lines for Cd, Sn, Sb and Ba are around zero. This means that sensitivity for these elements will not decrease significantly and that the absorption in covering layer is not observed, due to the high energies of pigments fluorescence radiations: Cd ( $K\alpha$  : 23,17 keV), Sn ( $K\alpha$  : 25,27 keV), Sb ( $K\alpha$  : 26,36 keV), Ba ( $K\alpha$  : 32,29 keV). In particular, Cd-K maps and detection suffer from two artefact: the Pb pile-up peaks and the interference in the spectra of the Rh-lines coming from the tube, as a consequence the Cd-K maps do not show significant difference in brightness in the 5 levels. Rh-K lines from the tube interfere also with Sn, but it appears better detectable than Cd. This happens because Cd was detected with its K-line (sum of  $K\alpha$  and  $K\beta$  lines) instead of  $K\alpha$  lines. The  $K\alpha$  fluorescence is usually 7 times more intense than the  $K\beta$  lines, so that the less intense  $K\beta$  lines influence the detection of Cd. Sensitivity for Sb and Ba is very low, they are barely detectable due to the employment of the polychromatic source and the Rh anode. Although the problematic detection, they are not absorbed by lead white (their slopes are very close to zero). Hg has a average behaviour, with a slop around 1. The choice to study the Hg-L1 lines influenced the results, since the L3 lines are much more intense. Probably if the L3 lines were analysed, an increase of the slope and therefore a greater difference in intensity in the 5 layers could have been detected.

In the Graphic 5.2, the behavior of AXIL scanner's sensitivity is highlights for 0 level. It is clear that AXIL D is more sensitive for mean-Z elements (in our case Cu and Zn), while elements with a high atomic numbers are less detectable (Cd, Sn, Sb, Ba). Although the trend is quite visible, the Sn dots do not really follow it, probably due to the interference of the neighboring Rh-peaks and Pb pile-up peaks.

## CHAPTER 5

### CONCLUSIONS AND OUTLOOK

Historical paintings are one of the most important precious part of cultural heritage, so that scientific investigations support their conservation and restoration. Paintings have a layered structure, that is made by applying many paint layers on the prepared ground. Most of the time, the paint's structure reveals important information as artists *modus operandi* (then the authorship), original painting, *pentimenti*, painting structure, etc.... so that covered layer is one of the keys for studying deeply the history of the painting. Mobile scanning MA-XRF is the technique that better fits this role in the field of cultural heritage, but, as most of the tools used in art research, XRF was not born for this purpose. For this reason in recent years, group of experts have developed some home-made mobile MACRO-XRF, but as newborns tools, they still have to be studied, tested and improved.

In this research, the possibilities and limitations of visualizing pigments common in historical painting by means of two MA-XRF scanners were studied.

I showed how basic parameters of the instruments could be important and fundamental to obtain visible improvements in elemental dispersive maps and which pigments are more detectable by the scanners. About the detection of pigment in the surface, step size of 500  $\mu\text{m}$  was proved to be enough for giving defined elemental maps, while the dwell time resulted to be critical for detecting some of the elements in the study: Sb and Ba, while Cd and Sn seem to be more detectable, but Pb pile-up peaks and the influence of the neighboring Rh-peaks have to be taken in account. Dwell time of 500 ms for M6 and 850 ms for AXIL scanner were proved to give excellent resolutions and particulars in elemental maps. A shorter dwell time could be employed for a "pre-scan" and then, the interesting area could be scanned by a higher dwell time for achieving more details.

Geometry of detectors resulted to be crucial for a better detection of elements in the study. AXIL D with the source at 90 degrees, the detectors at 45 and 47 degrees and closer to the sample, lead to obtain a notable improvement in detecting pigments, than AXIL C, which had source at 80 degrees and detectors at 25, 36, 45, and 39 degrees. This is the reason why it was chosen for the quantitative part of the research.

Sensitivity and limit of detection were calculated for the seven elements at the five levels. As we expected from the theory and from the elemental maps carried out in the qualitative part of the study, copper and Zinc resulted to be better detectable by AXIL scanner D. Their sensitivities are close to 10000 cps/mg when they are in surface and they roughly decrease with the growth of lead white. In fact they weak fluorescence radiations are easily absorbed by lead. In particular pigments composed by copper in hidden layer, are quite impossible to be visualized by means MA-XRF. Other techniques coupled with MA-XRF can help its identification in historical painting. About the other heavier elements (cadmium, tin, antimony and barium), they have a very low sensitivities due to their high energies of excitation. The use of a polycapillary optic attenuates the high energetic part of the primary radiation and also element heavier than rhodium cannot be well excited. A higher energetic primary radiation is needed to better excite heavy elements, but the radiation would be strongly scattered in the sample and difficult to shield, so that the energy of primary radiation must be limited for radiation protection worries in mobile instruments. Although the instrument is not so sensitive for these elements, they can be visible if present in hidden layer, in fact covering lead white layers do not absorb their strong X-ray fluorescence radiations. Indeed, cadmium, tin, antimony and barium, elements presents in most of the common pigments in historical paintings, are very well visible in elemental maps if some based parameters of scanning are respected.

Limits of detection are of course higher in hidden painting and they increase with the growth of lead white, since since there is more mass necessary in the covered layer to emit the same amount of fluorescence

radiation reaching the detector after absorption in the covering layer. Moreover, as we expected from the sensitivity trends, LODs are upper for heavy elements, as they are worse detected.

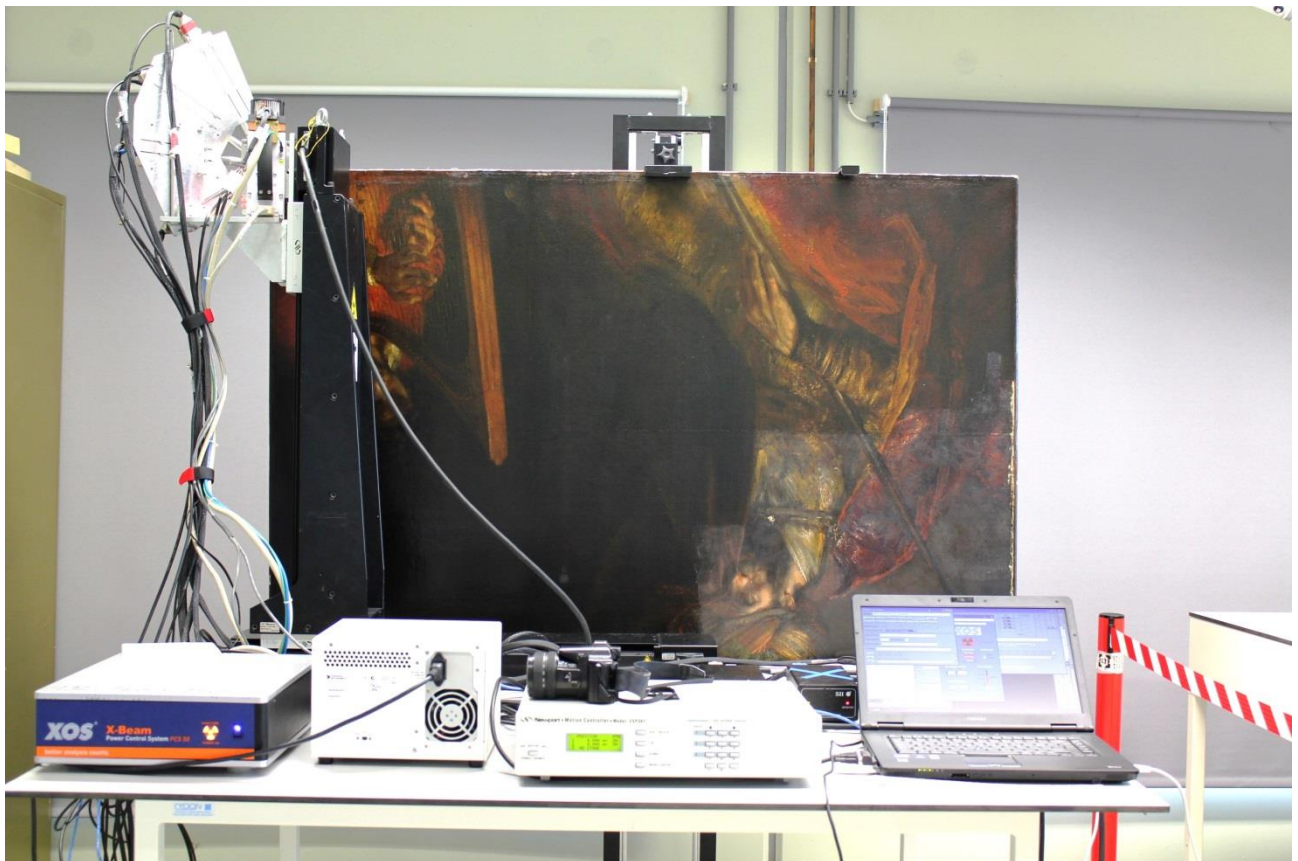
In conclusion two trend were obtained, one for  $S'$  e one for LOD, but they do not fit very well. The main reasons could be:

- a) Paint layers are inhomogeneous. Since the film applicator is a manual instrument, operator has to work with the same pressure during the operation. Furthermore, the different grain of the pigments can also influence the thicknesses of the layers.
- b) A complete and competitive study needs a much larger set of experimental data, the three samples in analysis can only give an idea of the sensitivity and LOD trends.
- c) Probably the measurement time is too low to obtain excellent quantitative data, which can be affected by the noise of the background.
- d) Sensitivity was calculated with the formula for monochromatic excitation instead of polychromatic. The equation (4.2.1.2), for  $R_i$  calculation is quite complicated to be planned with a simple calculation program. A specific program could be more appropriate.
- e) The calculation was simplified using the angles  $\alpha = 90$  and  $\beta = 45$ , but in reality detectors cover a range of angles from  $\beta_{\min}$  to  $\beta_{\max}$ , so that I approximated the calculation of  $R_i$  through the absorption factor  $A_i$  (see formula 4.1.2.3 and 4.1.2.4).
- f) Self-absorption was neglected
- g) Spot size was not calculated, but it was supposed to be  $1\text{mm}^2$



## CHAPTER 6

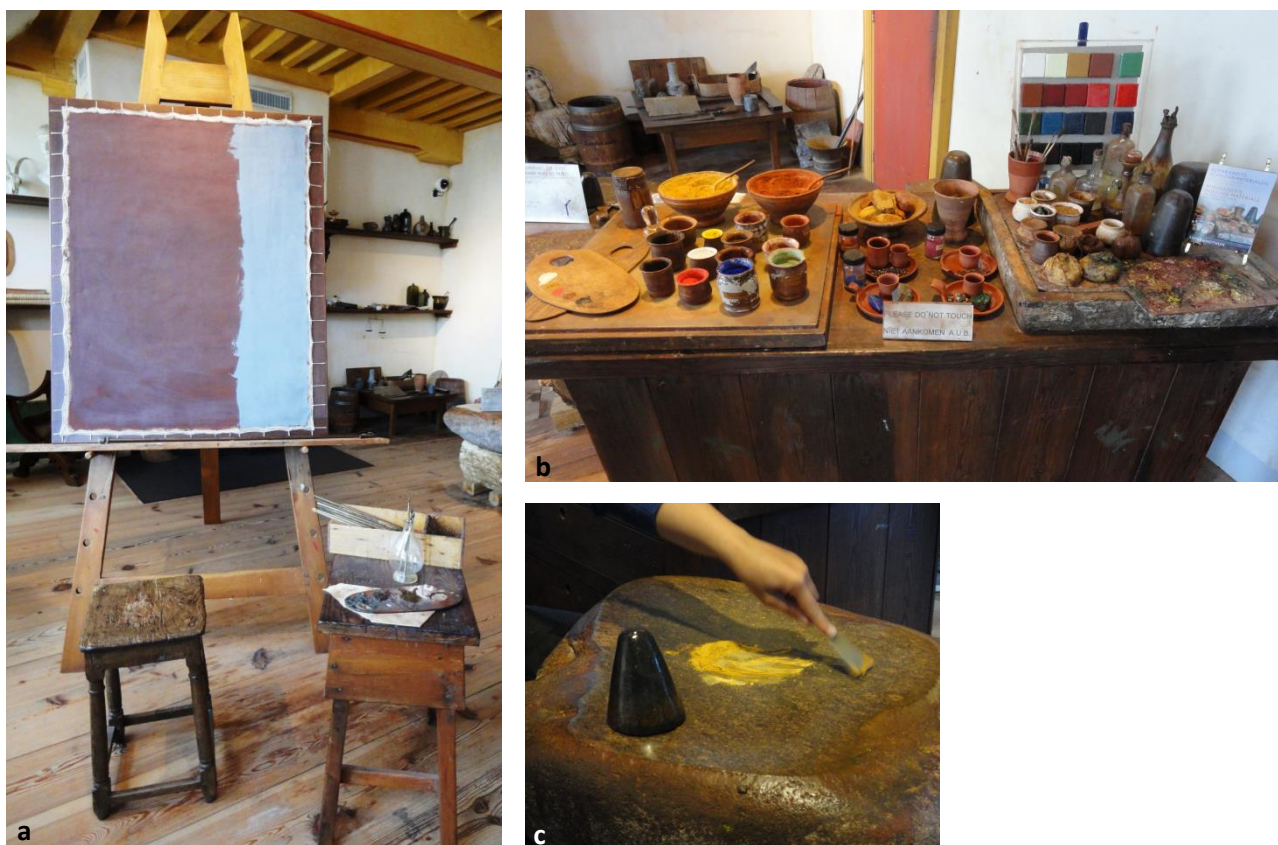
### REMBRANDT: “SAUL AND DAVID”, STUDY OF COBALT



## 6.1. Technique and pigments used by Rembrandt

In this chapter, the imaging analysis of a painting by the famous 17<sup>th</sup> century painter Rembrandt van Rijn, called 'Saul and David', belonging to the collection of the Royal Museum Mauritshuis, Den Haag, The Netherlands, is discussed. This investigation is part of a larger project dedicated to shedding more light on the painting techniques and materials employed by Rembrandt during the last part of his career.

What technical information Rembrandt was taught may be discerned by studying the works of his instructors, Jacob Isaacszoon Van Swanenburch, who had taught him for three years and Pieter Lastmann, with whom he specialized in history and biblical painting, or mythological stories. In the end, Rembrandt obviously surpassed them both. He experimented with paints and grounds and he arrived at methods and recipes that only he and his pupils used (Weil & Belchetz-Swenson, 2007). Various examples of Rembrandt's works show that he was not limited to any one technique, but employed them all, the choice depending on which approach best suited the subject in question, and for what purpose the painting was intended. Rembrandt painted on wood, sometimes on copper and later on canvas for larger works. Rembrandt used typically a plain weave, fairly rough canvas mounted on to a strainer or fixed wooden support using strings, a quite unique technique to Holland and similar to the method of attaching sails on a ship. This method allows the canvas to be tightened by simply pulling on the strings and it permits to paint out to the edge of the canvas without the interference of the stretcher behind (Schot & Dreu., 2010).



**Figure 6.1** Pictures taken in Rembrandt's house in Amsterdam, where his study room is reproduced: a) canvas mounted on fixed wooden support using strings; b) table with an exposition of the pigments used by Rembrandt, palettes on the left and on the right blisters containing pigments; c) stone where Rembrandt used to grind and create pigments.

The first layer of primer for the panels is a type of glue-chalk gesso, sanded to smooth out the irregularities of the panel's surface. Subsequent layers might consist of finer-textured chalk bound with hide glue, or white lead oil paint. The final layer was usually covered with a transparent brown *imprimitura*, which creates the golden glow characteristic of his work.

At the beginning of his career he used canvases with double ground: a reddish brown oil paint to seal the canvas further and improve the adhesion of the part; for the second layer he used greyish paint. The ground layers were applied with a special knife with a curved blade. In this way the surface was smoother and ready for the painting. Later he used only one layer: a mixture of mainly oil, minced sand and clay. On the ground layer, Rembrandt sometimes made the sketch of the composition in transparent brown, black paint or sometimes he used pale colors as well. After this process called "dead coloring", the composition was worked up in detail with more strong colors.

Paints are made up of pigments and binding medium. Rembrandt experimented with linseed egg, wax oil or gum. In the seventeenth century pigments were really expensive, also for a rich artist such as Rembrandt. The genius used to create new colors with a limited numbers of pigments; in the beginning of his career he used about twelve paintings while in his last period only six. Pigments were ground daily and placed in mussel shells until they were put on the palette. Ground pigments in mussel shells were left in water. Most of them could be kept for several days if submerged in water to exclude oxygen (Schot & Dreu., 2010).

Rembrandt's palette consisted of (Schot & Dreu., 2010):

- black (bone black or ivory black, less frequently charcoal): bone black is considered the deepest black of all and was used extensively by Rembrandt when sketching the under-layers of his paintings and for the deep black of the costumes worn by his sitters;
- a number of earth colors ( ochres, siennas and umbers): the stability of ochre's stability, the color range, and variable translucency ( up to opacity) suited Rembrandt's purposes well and therefore tended to predominate in most of his paintings. In addition to iron oxide, umber contains black manganese dioxide that has a siccative effect on linseed oil. Therefore, they were added by Rembrandt to the ground layers to promote faster drying;
- cassel earth;
- lead-tin yellow in highlights;
- occasionally vermilion, produced by the direct combination of mercury and sulfur with heat followed by sublimation, it was highly developed in the time of Rembrandt. He used to prefer bright red ochre heightened by the addition of red lake rather than vermilion, which was really expensive, which he only used occasionally;
- a number of yellow and red lakes. The lake pigments (produced from textile dyes fixed to a precipitate formed with alum and potash or to a chalk substrate) typically used in oil painting to produce effects of richness and depth over opaque underlayers, were rarely used for this purpose by Rembrandt, who typically mixed lakes directly with other pigments to enrich their color;
- flake white (*schulpwit*, a higher grade of lead carbonate without chalk) and lead white (*loodtwit*) in flash tone (lead carbonate with chalk);
- azurite verditer, a synthetic azurite, was available in the 17<sup>th</sup> century and has been found in some of Rembrandt's paintings, it is a good dryer because it contains copper that has a siccative effect on linseed oil and it appears more frequently in Rembrandt's early work.
- smalt used as a blue in the later pictures. Smalt was popular because of its low cost. Its manufacture became a specialty of the Dutch and Flemish in the 17th century. Smalt is a very good dryer and was used by Rembrandt for this purpose and also to give bulk to thick glazes containing lake pigments, which are poor dryers.

In Rembrandt's method, the evidence indicates that drying was accomplished by adding fast-drying pigments to his mixtures where they were needed. The principal pigments used for this purpose were smalt, azurite, umbers and lead white.

**Table 6.1.** Rembrandt's palette (Schot & Dreu., 2010):

Pigment	Colour	Raw material	Source
Umber	From dark brown to deep black	Earth: mineral	Found all over the world
Sienna	Yellow or red	Earth: mineral	Italy
Ochre	Yellow, orange, brown or red	Earth: mineral	Mainly France and Italy
Kasselearth	Dark brown	Earth: mineral and organic (e.g. peat)	Various places but mainly near Kassel and Cologne
Azurite	Light blue when finely crushed, dark blue when coarsely crushed	Mineral	Mainly from Hungary until it was occupied by Turks in the 17 <sup>th</sup> century
Lead white	White	Man-made from lead	Lead ore is found in various places in Europe
Lead-tin-yellow	From light to dark yellow	Man-made from lead and tin	See lead white
Vermilion	Orange red	Metal (cinnabar) or man-made from mercury and sulphur	Cinnabar is found all over the world e.g. Almadén (Spain), Idrija (Slovenia)
Smalt	Blue	Glass containing cobalt and sand	Silver mines in Saxony
Carmine	Carmine red; this is blue red	Cochineal beetle	Central and South America; mainly in the Oaxaca region of Mexico
Madder	Purplish blue	Plant: madder root	Originally from Asia, also cultivated in Zeeland in the 17 <sup>th</sup> century
Bone black	Black	Man-made: from bones	All over the world

## 6.2 History of the painting: "Saul and David"

According to the Bible, more exactly the Books of Samuel, David, second king of the United Kingdom of Israel and Judah, had beaten the Philistines and returned to the court of King Saul. The superstitious king considers David a threat to his already weakened position. In the painting in Fig. 6.2 b, we see Saul trying to think of a way to get rid of the young hero. At the same, he is moved by David's harp playing and he dries his eyes with a curtain. People would rise against him if he were to kill David, so he promotes David to "Captain over a thousand", hoping he will die in battle. This version of the painting is much more melancholic and touching than the earlier edition of the same episode, which Rembrandt created in 1630 (<http://www.artbible.info/art/large/378.html>, 2008).



**Figure 6.2 a.** Rembrandt Harmensz van Rijn (1606 – 1669), Saul and David (c. 1630), Städel Museum, Frankfurt am Main.



**Figure 6.2 b.** Rembrandt Harmensz van Rijn (1606 – 1669), Saul and David (1655-1660), oil on canvas (130 × 164 cm), Mauritshuis, The Hague.

The history of this painting is very troubled and only with the experience of analytical chemists and art historians, it was possible to reconstruct its origin, so that now we have a lot of information regarding Rembrandt picture's condition and original appearance. The first mention of the painting occurs in the Caraman auction of 1830 in Paris, where its width is listed as 20 cm wider than what it is now: 121,5 x 180,9 cm. In the late 1970s, and again in the 1990s, questions regarding the original dimensions, the iconography and the less good state of preservation, particularly of the curtain, remained unanswered.

In 2007 an analysis campaign has discovered that at some point in the past, the two figures were cut apart and reassembled by means of a unique notched join; during the process the picture became reduced in width by 20 cm along the vertical join between the figures of Saul and David and at the same time above the head of David, a large piece of missing canvas (h x w, 53 cm x 51 cm) was replaced with a piece of canvas cut from another painting. Narrow strips were also added to the upper, bottom and right edges. Therefore, the painting consists of ten separate pieces of canvas; a strip of canvas is also missing along the vertical join between the figures of Saul and David. The differences in dimensions listed in the 1830 and 1869 auction catalogues indicate that the painting must have been fashioned into its current format between those dates. The overpainting between the two figures in the background was doubted to be original and the uncertainty was solved with the analysis campaign by means of X-radiography (XRR), infrared reflectography (IRR) and micro-analysis of selected paint samples. The analysis showed the real appearance of the canvas and several other types of information. However, the XRR and IRR provided little information about the condition of the paint layers. Subsequent micro-analyses of carefully selected paint samples demonstrated that the curtain is indeed original to the painting and that the original curtain paint layer contains smalt, which is absent in the overpainting. In 2012, X-ray fluorescence (XRF) imaging using the mobile XRF scanner AXIL, provided elemental distribution maps of the curtain between the two figures. The cobalt, nickel, arsenic and potassium distribution maps (see Fig. 6.3), generated from elements in the smalt provided, for the first time, an image of the original hidden curtain below the muddy overpaint and yellowed varnish (Noble, 2012).

**Table 6.2.** List of changes in size over the years (Noble, 2012).

Until 1830: Coll. Victor-Louis-Charles de Riquet (1762-1835), Duke of Caraman, Vienna and Paris
May 1830, Caraman auction, Paris, lot 76 as Rembrandt, "T. h. 45 p. l. 67. [= c. 121.5 x 180.9 cm]"
Until 1835: Coll. Didot de Saint Marc, Paris.
1835-1863: Coll. Mrs. Abel Vautier (widow Saint Marc), Caen, auctioned December 1863, Paris, lot 31 (as Rembrandt).
1863-1869: Coll. Alphonse Oudry (1819-1869), Paris, auctioned April 1869, Paris, lot 52 (as Rembrandt). "Toile.- H. 1 m. 31 c., L. 1 m. 64 c."
1869-1870: Dealer Durand-Ruel, Paris
About 1870: Coll. Fébure, Paris
Before 1876: Coll. Saint Bourgeois, Cologne
1876 Coll. Albert Baron von Oppenheim, Cologne [exhibited Cologne 1876]
Dealer Saint Bourgeois, Cologne
1890-1891: Coll. M. Philippe George, Ay (Marne)
1891-1898: Dealer Durand-Ruel, Paris and New York [exhibited <i>The World's Congresses</i> , The Art Institute of Chicago, September 1893, no. 27; exhibited Amsterdam 1898, no. 118]
1898: Coll. Abraham Bredius (1855-1946), The Hague [on loan to Mauritshuis; exhibited Moscow/ Leningrad 1936]
1946: Bredius bequest to Mauritshuis

### 6.3 Purpose

The aim of this research was to investigate the painting in greater detail. I focused the attention on the study of the cobalt, in order to complete the analysis campaign started in 2012 by Matthias Alfeld et al. The Co distribution map obtained by means of macro-XRF scanner demonstrated the authenticity of the curtain in the middle of the painting. Looking closely at the cobalt distribution map, cobalt is also present in the modern insert in the upper right of the red frame (Fig. 6.3 b). This observation suggests two different sources of cobalt: small in the original paint layers and cobalt drier added to the 19<sup>th</sup> century overpainting covering the insert and the joins (Noble, 2012). It is clear that a full scan of the painting would allow new information to be gained about the complicated history of the painting.

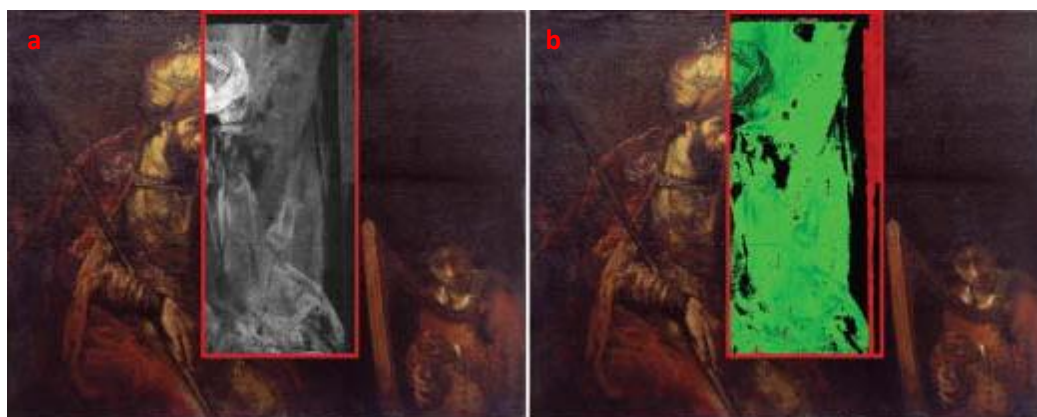
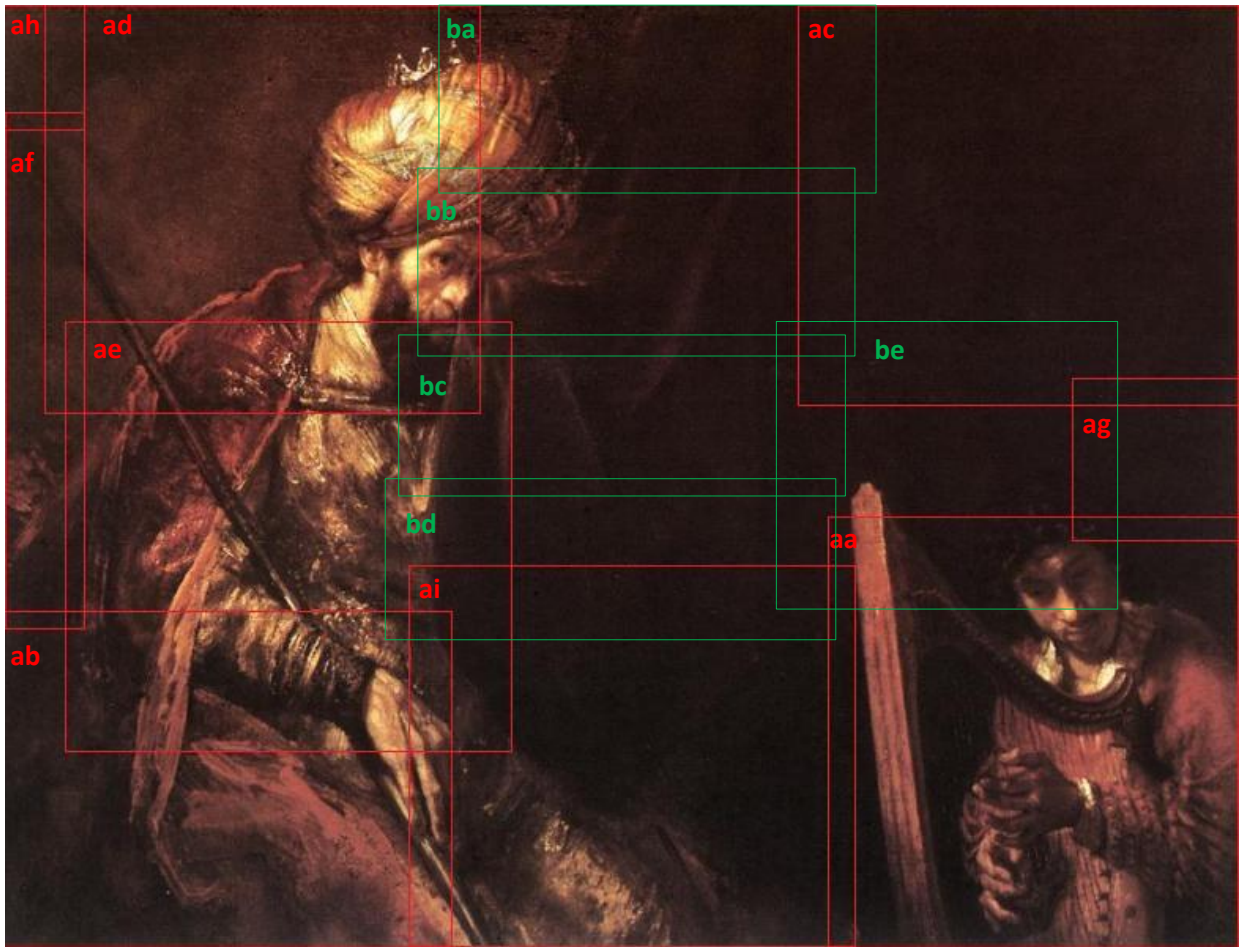


Figure 6.3. a) Co distribution map; b) Co:Ni ratio distribution map. Both images are taken from the article (Noble, 2012)

The painting was investigated in July 2013, in the Mauritshuis Conservation Studio ( Den Haag, NL ) with the supervision of Mrs. Petria Noble (head of conservation studio) and Geert van der Snickt (conservator and researcher of the University of Antwerp, Department of Chemistry) using the self-built macro-XRF scanner AXIL. This device has a maximum scanning capability of 60x60cm. The prototype scanner consists of a 50 W Molybdenum X-ray tube with a fixed polycapillary lens and four energy dispersive X-ray detectors mounted on a XZ-motor stage. The painting was scanned over a period of 20 days, at an average speed of 200 ms per pixel and a lateral resolution of 1000  $\mu\text{m}$ . The fluorescence radiation for each pixel was captured by the X-ray detectors in a series of nine scans. The acquired spectra were processed by PyMca and an in-house written software set called *Datamuncher*. The number and the size of the scans were first studied and decided in the laboratory of the University of Antwerp, so that they would cover the whole picture in the shortest possible time. Using this type of analysis, the essential is that the various scans mutually overlapped by few centimeters. In this way we are sure not to leave out any area of the picture; the overlapped areas are also crucial for stitching the scans together with the software *Datamuncher*.

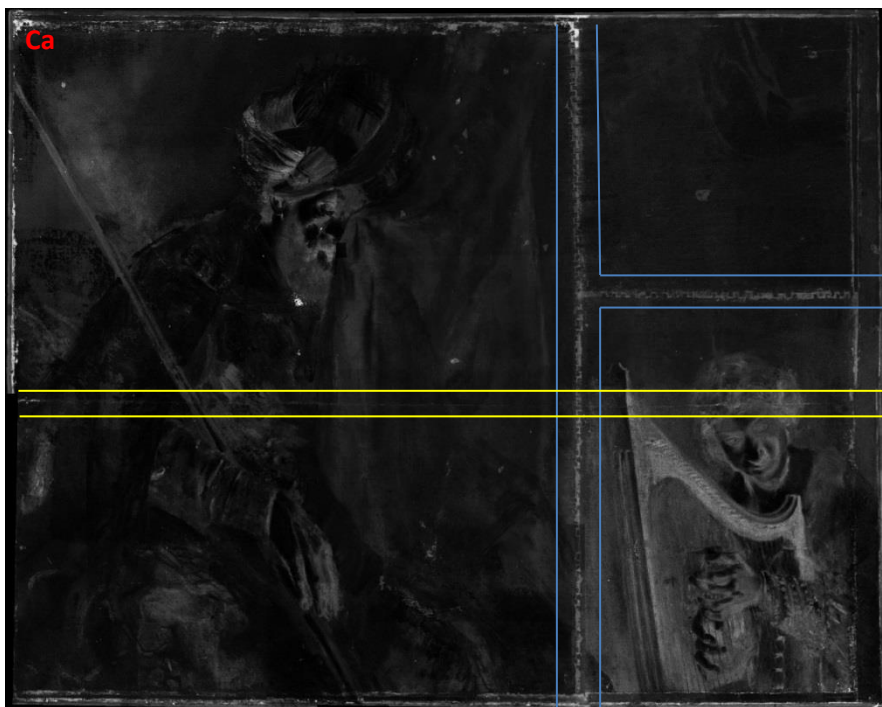
Table 6.3. Operating details of the scans.

Scan	Size of image (w x h)	Step size (mm)	Time per pixel (ms)	Total time (h)
aa	60 cm x 57 cm	X = 1mm ; Y = 1mm	200ms	20 days
ab	60 cm x 57 cm	X = 1mm ; Y = 1mm	200ms	
ac	60 cm x 57 cm	X = 1mm ; Y = 1mm	200ms	
ad	60 cm x 57 cm	X = 1mm ; Y = 1mm	200ms	
ae	60 cm x 57 cm	X = 1 mm ; Y = 1mm	200ms	
af	10 cm x 60 cm	X = 1mm ; Y = 1mm	200ms	
ag	20 cm x 20 cm	X = 1mm ; Y = 1mm	200ms	
ah	10 cm x 15 cm	X = 1mm ; Y = 1mm	200ms	
ai	60 cm x 57 cm	X = 1mm ; Y = 1mm	200ms	

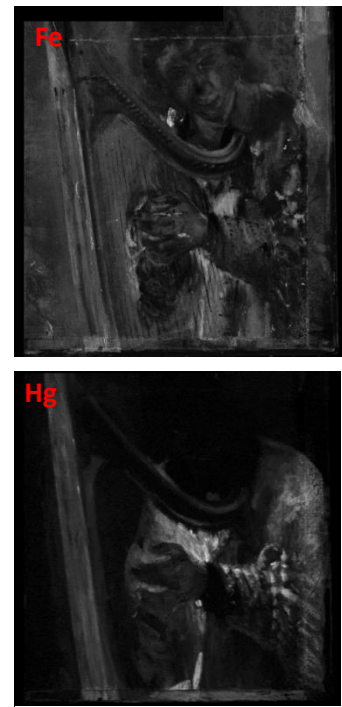


**Figure 6.4.** Saul and David, the five green frames indicate the scans made in 2011 by Matthias. The nine red frames indicate the new scans made in July 2013.

### 6.3.1 Results and discussion



**Figure 6.5.** Ca-K map. The light blue lines highlight the new joints and the yellow lines highlight the old, original joint.

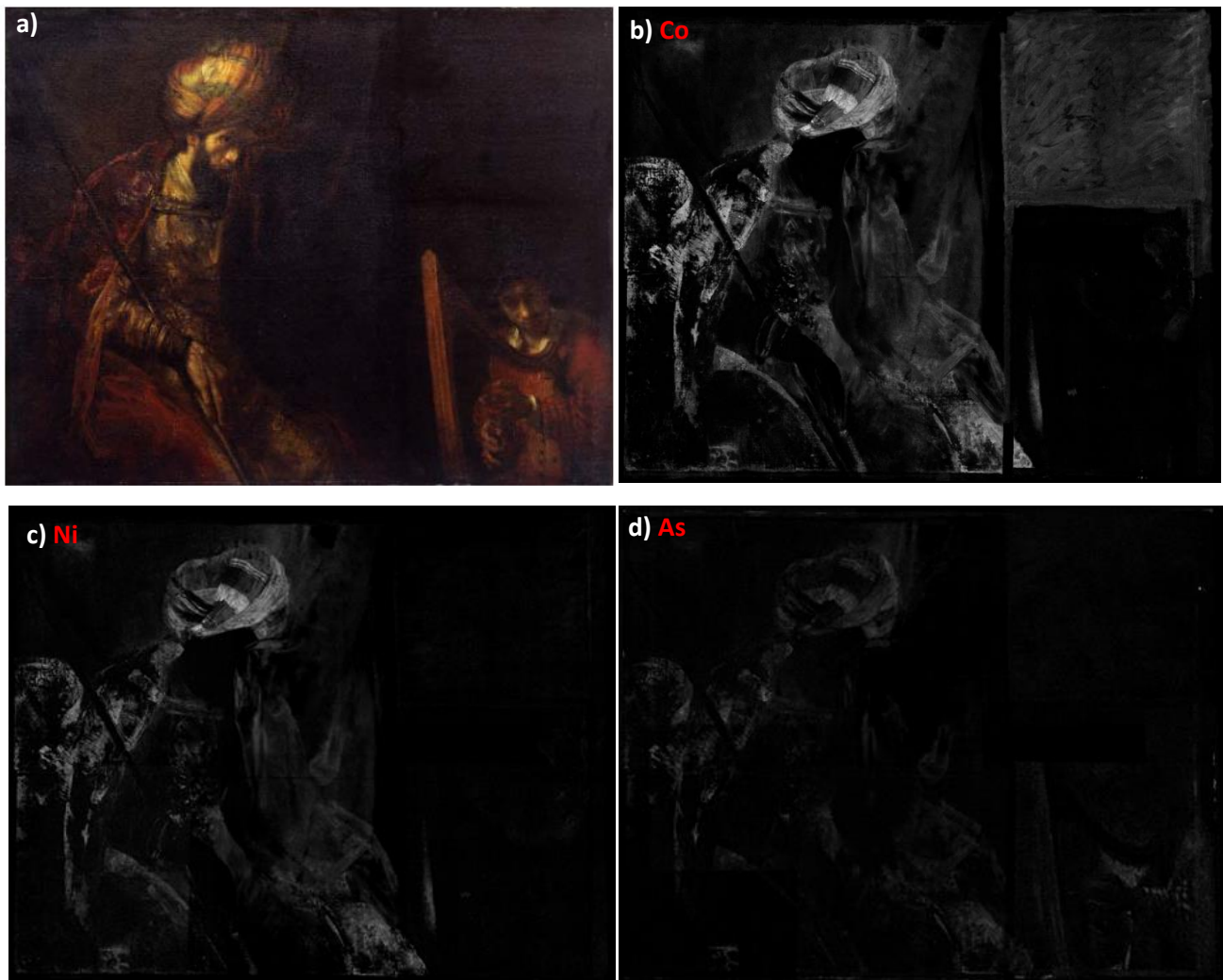


**Figure 6.6.** Particular of David, Fe-K map and Hg-L map.

The development of a mobile scanner provided the opportunity to obtain *in situ* elemental distribution images of *Saul and David*, since the picture was not able to leave the conservation studio. The Ca-K map allows us to see the completely painting in detail. In this map is possible to notice the new vertical and horizontal notched joints, which stitches together the canvas where David is represented with the new black piece of canvas on top and the rest of the left picture. In yellow the old and original joint is highlighted, which is much more subtle and runs horizontally over the head of Saul. The Ca probably comes from chalk; Rembrandt used to dilute expensive pigments (such as lead white) with less expensive materials such chalk. The genius did not add chalk just to save money, but in this way he also increased the viscosity of the paint.

Focusing on scans of the areas in which David is visible, some marker elements are well visible: as we have already said Ca K-lines fluorescence probably correspond to chalk ( $\text{CaSO}_4$ ), used as a paint extender; Fe K-line corresponds to red-brown earth pigments (such as umber, sienna, ochre, Kassel earth); Hg-L lines corresponds to vermilion, an expensive pigment that was used sparingly by the artist. Hg is present only in this specific part of the canvas.

Smalt is composed by cobalt and other minor elements such as nickel and arsenic. Indeed, they are potential markers for imaging the presence of the smalt in the painting. Elemental distribution maps of those elements were recorded and are shown in Fig. 6.7.

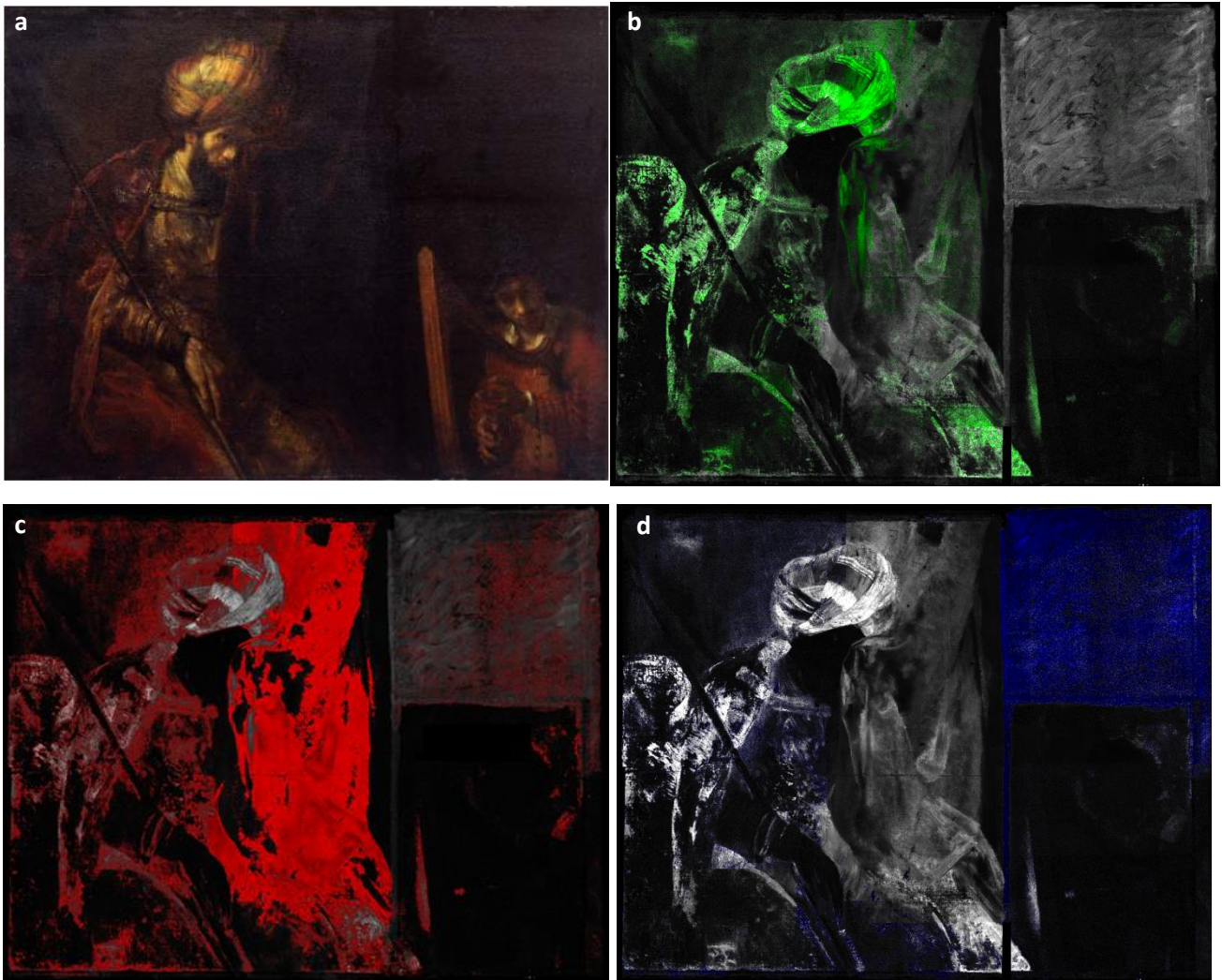


**Figure 6.7.** a) Rembrandt *Saul and David*, c. 1655, 126 x 158cm (original canvas); 130,5 x 164,5 cm (stretcher); b) Co map ; c) Ni map; d) As map

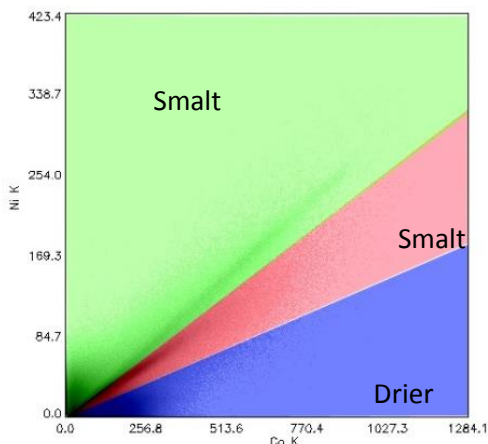
The elemental map show the presence of Co in the clothes and turban of Saul, on the curtain in the middle of the painting and in the background on the top right. If we compare the three elemental distribution maps, we note that Ni and As are not present at the top right of the painting, where Co is evidently present



in high concentration. This observation suggests that the curtain, the clothes and the turban of Saul are painted with smalt, while Co was used as drier in the dark overpaint layers of the modern insert and from the restored damage. The ratio of cobalt to nickel, or cobalt to arsenic (minor elements associated with smalt), allows us to discern directly the distribution of Co used as smalt or as a drier. In effect the Co:Ni ratios gave us much more information. The pixels of cobalt distribution image were colored based on their attribution to smalt (green and red) or drier (blue). Pixels of low intensity are not assigned and are thus left uncolored. This is possible using a particular option of the home-made software *Datamuncher*.



**Figure 6.8.** a) Rembrandt Saul and David, c. 1655, 126 x 158cm (original canvas); 130,5 x 164,5 cm (stretcher); b) Co:Ni ratio map, smalt; map ; c) Co:Ni ratio map, smalt; d) Co:Ni ratio map, Co as a dryer.



**Figure 6.9.** Cobalt:Nickel scatter plot

The Co : Ni ratio distribution suggests that the concentration of Smalt is less high in the curtain than in the Saul's clothes and turban. It appears that in the painting there are two different kind of smalt, because the percentages of Co are different (Figure 6.9). The different concentration is probably due to the fact that the original curtain is overpainted, so the low-energy fluorescence radiation emitted by Co in the curtain is readily absorbed by the overpainted layers. In effect the curtain also be rendered visible by the Fe-K distribution map (Figure 6.10). Iron corresponds to the red earth used in the brown paint

mixtures for the final stages of the curtain and in the red of the curtain wrinkles. Since iron is also an impurity of cobalt ore, Fe can also coincide with smalt in the clothes on the surface layer.

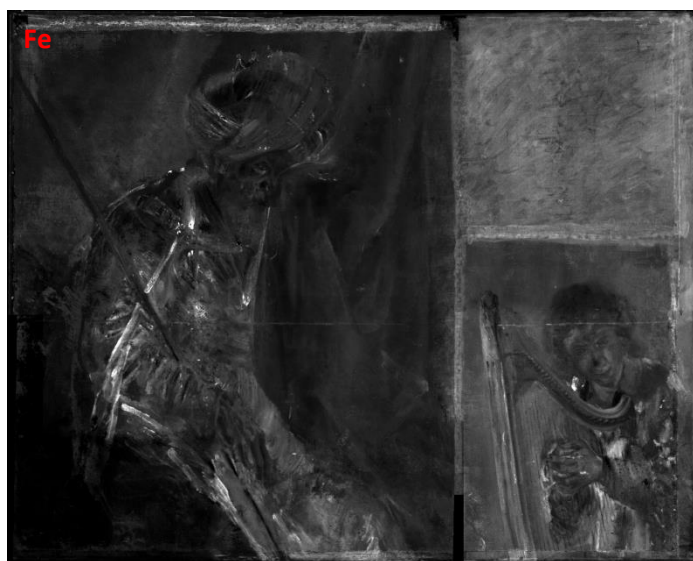


Figure 6.10. Fe-K distribution map

As a result of the overpainted, the element Co cannot give the same intensity fluorescence of Co detected in the surface layer (for example Co present on clothes and turban). Despite this fact, the other constituting elements of smalt (nickel and arsenic) are revealed; this allows us to be ascertain that the detected Co in the curtain corresponds to smalt.

On the top right, where there is the modern insert of canvas, cobalt is detected as a minor constituent dispersed throughout the layer rather than as a component associated with pigment particles; cobalt was used in addition to black pigment as a drier.

It should be also interesting to investigate the new peace of canvas added on top right of the painting. From the Co elemental map seen before, we see that quickly brushstrokes of black have been given to create a dark background.

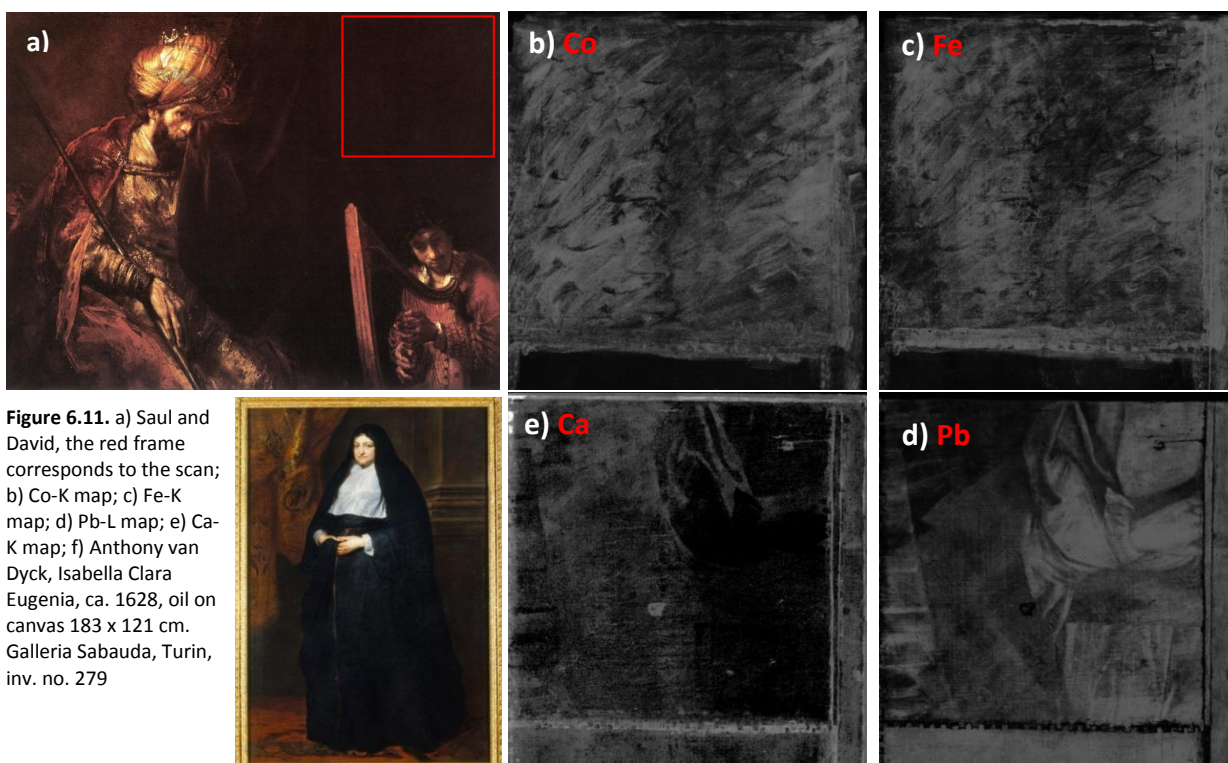


Figure 6.11. a) Saul and David, the red frame corresponds to the scan; b) Co-K map; c) Fe-K map; d) Pb-L map; e) Ca-K map; f) Anthony van Dyck, Isabella Clara Eugenia, ca. 1628, oil on canvas 183 x 121 cm. Galleria Sabauda, Turin, inv. no. 279

In Figure 6.11 b) and c) the Co and Fe maps of this area are shown. In this piece of canvas, Co, as mentioned before, was used as a drier in addition to a black pigment, probably an iron (II) oxide. The elemental distribution maps in d) and e) were able to image the hidden painting with unprecedented detail. In effect, the Pb-L map clearly shows a hidden painting. The detected emission lines of lead can originate from different materials such as: lead white, lead tin yellow, minium, Pb-base driers, etc... The Ca-k lines fluorescence signals provide information about the bottom join, some restored damage, carbon black and/or chalk used in the habit of the hidden painting. While it could be difficult to discover the provenience of this piece of canvas, it has recently been identified as part of an early copy of a painting by Anthony van Dyck's called "Portrait of Isabella Clara Eugenia, Infanta of Spain", turned upside down (Gordenker & Noble, 2013).

## 6.4. Conclusion

This research helped to complete the Analysis Campaign began in 2007. *Saul and David* framework had undergone many changes over the years and the full scan of the painting revealed details and information that could not be obtained by other means. First of all, the advantage of this mobile technique is that the framework has not been subjected to transport and it was possible to analyze it without further action on the work causing irreversible damage.

When performing this kind of analysis, I want to emphasize that the first and most important step on the work carried out in Den Haag is the organization needed to perform scans with mobile macro-XRF scanner. The most important step is to determine the size, the time per pixel and step size of the areas of interest before going to the museum. Since the scan instruments are in high demand by museums and research laboratories, indeed the appropriate organization and planning of the required sequence of scans needed is mandatory to optimize the total analysis time.

The recording of elemental distribution maps with XRF-imaging is of great interest. In the study of traditional paintings, it allows the investigation of the pigments used by the artist, pigment alterations, as well as the possibility to reveal changes made to the painting during or after its creation. In the case of *Saul and David*, a hidden piece of canvas could be attributed by historical experts to a copy of a painting by Anthony van Dyck. Other changes were not visible except for the modern and old joints.

In this research the most important discovery, that will enrich information about the painting, is the presence of three main areas with at different type of cobalt. Thanks to the in-house built software *Datamuncher*, it was possible to analyze the entire painting by stitching the thirteen scans together. Using the output tool *correlate*, it was possible to plot the ratio between two critical elements, in our case cobalt and nickel. After color-labelling the different types of Co:Ni in the graph, the identification of the 3 trends of this ratio was done. In conclusion, the smalt is present in the clothes and the turban of Saul while a lower concentration of smalt is detected in the curtain. This is because the original paint has been covered (probably with earth pigments) and the Co-K XRF signal in covered layer are attenuated. A high percentage of Co, used as drier, was detected in the insert in the upper right. Cobalt accelerated the drying of the black background in order to cover the underlying piece of canvas of van Dyck.

## 7. BIBLIOGRAPHY

- Alfeld, M. (2013). *“Development of Scanning macro- XRF for the Investigation of Historical Paintings”*. Antwerp: University of Antwerp.
- Alfeld, M., K. Janssens, J. Dik, W. de Nolf, & G. van der Snickt. (2011). "Optimization of mobile scanning macro-XRF systems for the in situ investigation of historical paintings". *J. Anal. At. Spectrom.*, 26(5), 899.
- Alfeld, M., Nolf, W. D., Cagno, S., Appe, K., Siddons, D. P., Kuczewski, A., et al. (2012). "Revealing hidden paint layers in oil paintings by means of scanning macro-XRF: a mock-up study based on Rembrandt's "An old man in military costume"". *JASS*.
- Alfeld, M., Pedroso, V., Hommes, V. E., & Snickt, G. V. (2013). "A mobile instrument for in-situ scanning macro-XRF investigation of historical paintings". *JAAS*.
- Alfeld, M., Snickt, G. V., Vanmeert, F., & Janssens, K. (2013). "Scanning XRF investigation of a Flower Still Life and its underlying composition from the collection of the Kröller–Müller". *Springer*.
- Bearat, H., & al., e. (s.d.). *“Mechanistic and computational study of cinnabar phase transformation: applications and implications to the preservations to the preservation of this pigment in historical painting”* (Vol. vol. 1).
- Bomford, D., Dunkerton, J., Gordon, D., & Roy, A. (1989). "Art in the Making: Italian Painting before 1400". *National Gallery*.
- Boston, M. o. (2013). *“Materials Database, Naples Yellow”*. Boston.
- Botteon, A. (2011-2012). *“MA-XRF Analysis on Paintings and Physico-Chemical Characterization of Smalt”*, Master thesis . Ca' Foscari University in collaboration with University of Antwerp.
- Brouwer, P. (2010). *“Theory of XRF ; getting acquainted with the principles”*. The Netherlands: PANalytical.
- Bull, D., Krekeler, A., Alfeld, M., Dik, J., & Janssens, K. (2011). "An intrusive portrait by Goya". *The Burlington Magazine*.
- Church, A. (1901). *“The Chemistry of Paints and Painting”*. London: Seeley & Co. Ltd.
- Clark. (1995). "Synthesis, structural characterization and Raman spectroscopy of the inorganic pigments lead tin yellow types I and II and lead antimonate yellow: their identification on Medieval paintings and manuscripts". *Journal of the Chemical Society*.
- Delamare, F., & Guineau, B. (2000). *“Colour: Making and Using Dyes and Pigments”*. London: Thames & Hudson.
- Eastaugh, N., Walsh, V., Chaplin, T., & Siddall, R. (2004). *“Pigment Compendium: A Dictionary and Optical Microscopy of Historical Pigments”*. Elsevier.
- F., R. (1988). *“Rutley's Elements of Mineralogy”*. Unwin Hyman: 27th Ed., revised by C.D. Gribble.

- Gary, L., Long, J. D., & Winefordner. (June 1983). "Limit of Detection. A Closer Look at the IUPAC Definition" (Vol. vol. 55). Analytical chemistry.
- Gauglitz, G., & Vo-Dinh, T. (s.d.). "X-ray analysis" in "The Handbook of Spectroscopy". John Wiley & Sons.
- Gordenker, E. E., & Noble, P. (2013). "Rembrandt's 'Saul and David' at the Mauritshuis: A Progress Report". JHNA, Vol. 5, Issue: 2.
- Gordon, D., Bomford, D., Plesters, J., & Roy, A. (1985). "Nardo di Cione's 'Altarpiece: Three Saints' ". *National Gallery Technical Bulletin* 9, 21-37.
- Harley, & Rosamund, D. (1982). "Artists' Pigments c.1600–1835". London : Butterworth Scientific.
- J. Dik, K. J., Snickt, G. V., Loeff, L. v., Rickers, K., & Cotte, a. M. (s.d.). "Visualization of a lost painting by Vincent van Gogh using synchrotron radiation based X-ray fluorescence elemental mapping" . *Anal. Chem.*, vol. 80(no. 16).
- Janssens, K. (2013). "Modern Methods for Analysing Archaeological and Historical Glass". John Wiley & Sons, Ltd.
- Janssens, K., & Grieken, V. (2004). "Non-destructive Microanalysis of Cultural Heritage Materials". Amsterdam, The Netherlands: Eds. Elsevier.
- Kuhn, H. (1993). "Lead-Tin Yellow, Artists Pigments" (Vol. Vol. 2). Oxford University : ed. A. Roy .
- Moser. (1973). "Barium Sulfate, Synthetic (Blanc Fixe); Pigment Handbook".
- Noble, P., Loon, A. v., Alfeld, M., Janssens, K., & Dik, J. (2012). "Rembrandt and/or Studio, Saul and David, c.1655: visualising the curtain using cross-section analyses and X-ray fluorescence imaging". *Technè*(n° 35).
- Schot, W., & Dreu., P. d. (2010). "Rembrandts Schildermaterialen, over linnen, loodwit en lijnzaadolie/ Rembrandt's painting materials, on linen, lead white and linseed oil". (M. H. Rembrandthuis, A cura di) Amsterdam.
- Snickt, G. V. (2012). "James Ensor's pigments studied by means of portable and synchrotron radiation-based X-ray techniques: evolution, context and degradation", PhD dissertation. University of Antwerp.
- Snickt, G. V. (2012). "James Ensor's pigments studied by means of portable and synchrotron radiation-based X-ray techniques: evolution, context and degradation", PhD dissertation . University of Antwerp.
- Standage, H. (1883). "The Artists' Table of Pigments, Showing Their Composition, Conditions of Permanency, and Adulterations, Effects in Combination with Other Pigments and Vehicles, and Giving the Most Reliable Tests for Purity". London: Wells Gardner, Darton & Co.,.
- Thompson, A. C., Kirz, J., T. Attwood, D., Gullikson, E. M., Howells, M. R., & Kortright., J. B. (2009). "X-ray data booklet". Berkeley, California: University of California.
- Toch. (1925). The chemistry and Technology of Paints.
- Tsuj, K., Injuk, J., & Grieken, R. V. (2004). "X-Ray Spectrometry: Recent Technological Advances". Eds Jhon Wiley & Sons.

Van Grieken, R., & Markowicz, A. (. (2002.). "*Handbook of X-Ray Spectrometry - methods and techniques*". Second edition, N. Y. Dekker.

Weil, P. D., & Belchetz-Swenson, S. (2007). "Technical art history and archeometry III: an exploration of Rembrandt's paintings and drawing techniques". *Revista Brasileira de Arqueometria, Restauração e Conservação*, vol.1, No. 6, pp. 326 -331.

<http://www.artbible.info/art/large/378.html>. (2008). Retrieved from <http://www.artbible.info/>.

[http://www.kremer-pigmente.com/media/files\\_public/10100e.pdf](http://www.kremer-pigmente.com/media/files_public/10100e.pdf). (n.d.). Retrieved from <http://www.kremer-pigmente.com>.

## 8. ACKNOWLEDGMENTS

I would like to thank Professor Koen Janssens for giving me the opportunity to do my thesis in his group of research at the University of Antwerp, for his precious supervision and for his encouragement.

I am grateful to Professor Carlo Barbante for supporting my project and for his motivation and important advice during the thesis writing.

I really thank Matthias Alfeld and Geert Van der Snickt, which taught me how to use AXIL scanner, M6 Jetstream and programs for processing data. Thanks Matthias also for the essential tips sent by email, once I came back to Italy and thanks Geert for supporting me and for the opportunity to go to Netherlands for scanning the Rembrandt's painting "Saul and David".

I'm grateful to Mrs. Petria Noble for welcoming me in her Conservation Studio of the Mauritshuis museum at Den Haag and for letting me scan and study such an important painting with the supervision of Geert Van der Snickt.

I'm beholden to Stijn Legrand and to Frederik Vanmeert for their precious help during the scan of the mockups.

I would like to thank also the researchers of the Department of Chemistry at Campus Drie Eiken for letting me use the Optical Microscope and the Department of Environmental Sciences, Informatics and Statistics of Cà Foscari for the disposal and the opportunity to use the Dino Lite digital microscope.

I warmly thank Stefano for the smiling office atmosphere, for encouraging me and last, but not list, for listening to my existential doubts.

Finally, I would like to thank all the Antwerp X-ray Analysis, Electrochemistry and Speciation group of research for welcoming me into their home and all of you for being patient with my weak English, especially at the beginning.

Il primo grazie va ai miei genitori, perché mi hanno permesso di vivere per sei anni nella città più bella al mondo, perché hanno sempre creduto in me e sostenuto le mie decisioni. Grazie anche a mia sorella, con la quale mi sono scambiata più o meno 10 messaggi in 6 anni, ma so che mi vuole bene e io ne voglio a lei.

Grazie alla mia Psi preferita, perché i Km di distanza che ci separavano non sono stati sufficienti ad indebolire la nostra amicizia. Grazie per aver sempre ascoltato le mie ansie e paranoie e risposto ai messaggi più tragici, grazie per aver studiato psicologia e per averla sperimentata alla perfezione su di me.

Grazie a tutte le subbie, senza di voi Venezia non sarebbe stata Venezia. Un'esperienza che mai cancellerò dal mio cuore, dalla mia mente e dal mio fegato. Sono stati i miei primi anni da donna consapevole e averli condivisi con voi è stata la cosa più bella, divertente e assurda. Grazie per aver condiviso tutto ciò con me e per avermi scelta. Sono sicura che la nostra sia una vera amicizia e che quel giorno ci ritroveremo tutte a Las Vegas come promesso.

Grazie a Bog, che è sbucato dal nulla e si è rivelato un personaggio fondamentale nella mia vita veneziana. Grazie per avermi sopportata ad Anversa, grazie per aver assecondato tutte le mie idee dell'ultimo secondo....dai corsi di inglese, alle americane, alle uscite, alle feste, all'Erasmus, alla visita a Roger,...e chi se le ricorda tutte!

Grazie alle mie amiche dell'Università. Ne ho conosciute tante e vorrei ringraziarle tutte per aver condiviso questa singolare scelta della Chimica per il Restauro. Annamaria per aver condiviso le stesse esperienze dall'inizio alla fine, a Venezia e all'estero, per aver sempre avuto la parola giusta al momento giusto e per esserci sempre stata nei momenti di bisogno e di festa. Grazie a Rita, Davide, Leo e grazie alle new entry della specialistica: Chiara, Valentina, Giulia, Max, Giada, Giovanna, Elena e alla desaparecido Gaia.... gli

aperitivi, le cene e i gruppi studio non sarebbero stati lo stesso senza le vostre risate e storie, ma avrei voluto incontrarvi prima!

Grazie a Robi, sei stato una salvezza in alcuni momenti e uno spasso in tutti gli altri! Grazie per essermi amico, per avermi compresa e per avermi dato saggi consigli.

Grazie a Zhabenzia per le risate fatte insieme e per il mondo di bene che mi hai dimostrato a tuo modo .....serpenzia come sei!

Grazie a Perpi e Bezzi, perché quando vi incontravo capivo che c'era sempre qualcuno messo peggio di me e mi sentivo quindi d'aiuto per qualcuno!

Grazie a mia zia Annamaria che si è resa volontaria per discutere di questa tanto sudata tesi e grazie a tutti i miei parenti, dai nonni agli zii ai cugini. Grazie per esservi sempre preoccupati della "nipote-cugina in fuga", grazie per aver passato i natali e le poche feste a cui ero presente insieme a me. Grazie di far parte di questa favolosa famiglia!

Grazie ai pochi amici che mi rimangono nel mio paesino, grazie per aver trovato sempre qualche ora per parlare con me quando rincasavo a Daverio city.

Grazie alle poche amiche trovate in Erasmus. Per fortuna vi ho trovate....sarebbe stato un completo disastro senza di voi!

Grazie a tutte le persone che ho incontrato durante questi anni, siete stati tutti fondamentali nella mia crescita di studentessa, ma soprattutto nella mia crescita di donna.